ORBITAL STABILITY ANALYSIS AND CHAOTIC DYNAMICS OF EXOPLANETS IN MULTI-STELLAR SYSTEMS

by

SUMAN SATYAL

Presented to the Faculty of the Graduate School of
The University of Texas at Arlington in Partial Fulfillment
of the Requirements
for the Degree of

DOCTOR OF PHILOSOPHY

THE UNIVERSITY OF TEXAS AT ARLINGTON

December 2014

Copyright © by SUMAN SATYAL 2014

All Rights Reserved

Dedicated to my mother, *Goma Pokhrel Satyal*

ACKNOWLEDGEMENTS

My sincere gratitude to my advising professors Dr. Zdzislaw Musielak (Ph.D.) and Dr. Alex Weiss (M.Sc.) for their guidance, advice and support through out the course of my graduate studies. Many thanks to Dr. Manfred Cuntz, Dr. Sangwook Park and Dr. Yue Deng for their interest in my research and for taking time to serve in my committee. I'm indebted to Dr. Billy Quarles and Dr. Tobiash Hinse for collaborating with me in couple projects and help me drown out from the ocean of orbital dynamics.

I would like to express my deepest feelings towards my parents, brothers, lovely sisters. I am grateful to my astounding friends in the seven continents. Also, a big radio shout out to all the civilizations that may be extending as far away as 13.6 billion light years.

It should be possible to explain laws of physics to a bartender -Einstein

October 8, 2014

ABSTRACT

ORBITAL STABILITY ANALYSIS AND CHAOTIC DYNAMICS OF EXOPLANETS IN MULTI-STELLAR SYSTEMS

SUMAN SATYAL, Ph.D.

The University of Texas at Arlington, 2014

Supervising Professor: Zdzislaw Musielak

The advancement in detection technology has substantially increased the discovery rate of exoplanets in the last two decades. The confirmation of thousands of exoplanets orbiting the solar type stars has raised new astrophysical challenges, including the studies of orbital dynamics and long-term stability of such planets. Continuous orbital stability of the planet in stellar habitable zone is considered vital for life to develop. Hence, these studies furthers one self-evident aim of mankind to find an answer to the century old question: *Are we alone?*

This dissertation investigates the planetary orbits in single and binary star systems. Within binaries, a planet could orbit either one or both stars as S-type or P-type, respectively. I have considered S-type planets in two binaries, γ Cephei and HD 196885, and compute their orbits by using various numerical techniques to assess their periodic, quasi-periodic or chaotic nature. The Hill stability (HS) function, which measures the orbital perturbation induced by the nearby companion, is calculated for each system and then its efficacy as a new chaos indicator is tested against Maximum Lyapunov Exponents (MLE) and Mean Exponential Growth factor

of Nearby Orbits (MEGNO). The dynamics of HD 196885 AB is further explored with an emphasis on the planet's higher orbital inclination relative to the binary plane. I have quantitatively mapped out the chaotic and quasi-periodic regions of the system's phase space, which indicates a likely regime of the planet's inclination. In, addition, the resonant angle is inspected to determine whether alternation between libration and circulation occurs as a consequence of Kozai oscillations, a probable mechanism that can drive the planetary orbit to a large inclination.

The studies of planetary system in GJ 832 shows potential of hosting multiple planets in close orbits. The phase space of GJ 832c (inner planet) and the Earth-mass test planet(s) are analyzed for periodic-aperiodic orbits. The stability of the system is defined in terms of its *lifetime* and maximum eccentricity during the integration period then a regime is established for the known and injected planet's orbital parameters. The de-stabilizing resonances due to the outer planet extend by 1.36 AU towards the star, nonetheless, existence of two Earth-mass planets seems plausible. The radial velocity (RV) curves generated for the test planets reveals a weak RV signal that cannot be measured by currently available instruments.

A theory has been developed by extrapolating the radio emission processes in the Jupiter-Io system, which could reveal the presence of exomoons around the giant exoplanets. Based on this theory, maximum distance, radius and masses of exoplanets and exomoons are calculated that could be detected by the available radio telescopes. Observation time at the Low Frequency Array (LOFAR) radio telescope has been proposed to detect exomoon in five different stellar systems. Subjects of my future studies include analysis of the data from LOFAR, search for the additional transiting planets in Kepler 47 circumbinary system and observation at the Subaru telescope to verify the predicted planets in GJ 832 system by the method of direct imaging.

TABLE OF CONTENTS

LIST OF FIGURES

LIST OF TABLES

CHAPTER 1

INTRODUCTION

1.1 Prehistoric Astronomy

The quest of food led the prehistoric humans to wander from mountains to valleys, valleys to mountains and eventually across the continents. At some point in time the nomadic lifestyle came to a halt, marking a birth of human civilization. Human beings no longer lived their lives just to gather food, but to expand their minds in thoughtful observations of their surrounding. The humans questioned the very presence of fire, water and life itself; and such zeal did not take long to look up into the heavens and question the very rise of the Sun, the moon and the stars.

Different civilizations from different continents are found to have some sorts of history where they have direct involvement in recording the motions of heavenly bodies. Ancient Egyptians built the Great Pyramids in Giza that are Sun-oriented and directed towards the four points of the compass with astonishing precision. Egyptians made the earliest calendars with 365-days year and 30-days months. Other contribution to the prehistoric astronomy includes, but not limited to, observation of planetary motions by the Babylonians, the calendar cycles during Homer and Hesiod in the Greek and the Roman worlds. Based on lunar observation, the *Vedic* astronomy around the Indian sub-continents devised a fascinating scheme of *Naksatras*, the twenty seven stars the moon passes through in one month period.

The first calendar (12 months, 360 days) devised by the ancient Sumerians was based on the Moon, while the Egyptians based their calendar (12 months, 360 days) on the Sun. But after they noticed that extra days were required in specific

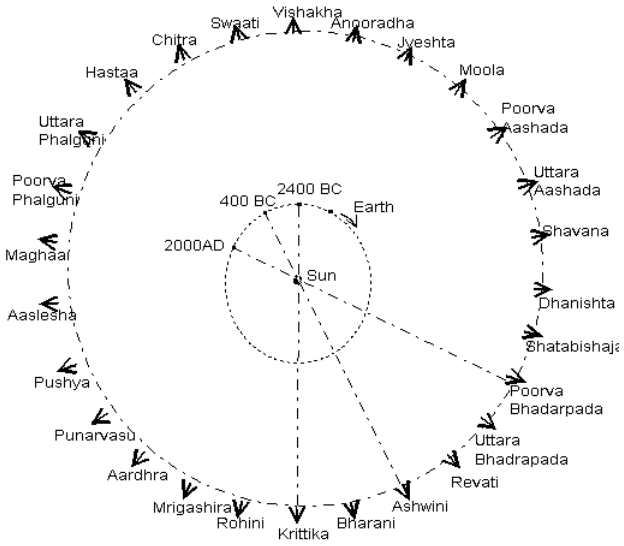

Figure 1.1. The effect of the Earth's precession on the Sun-Star-Earth position during vernal equinox over past 5,000 years. The twenty seven *Naksatras* are shown in the ecliptic plane. Image Credit: vedicastronomy.net.

intervals, they simply added 5 feast-days at the end of the year to essentially come up with an accurate calendar (Aughton 2008). These calendars were adopted by various civilizations for over 3,000 years and seeded an astronomical culture of record keeping the tracks of heavenly bodies across the sky. Such knowledge would greatly assist humans to determine the right time to harvest and cultivate their produce.

1.2 Medieval Planetary Astronomy

Even though the prehistoric humans made a giant leap in the studies and understanding of the celestial bodies, it took aeons for them to actually solidify the knowledge regarding positions and motions of Solar system bodies. It was long standing belief that the Earth was at the center of the Universe, and something they considered *Universe* later turned out to be the Milky way galaxy, one among the billions in the visible Universe. The Geocentric model of the universe came to an end when a Polish astronomer, Nicolaus Copernicus (1473-1543) came up with the observational

proof of the heliocentric (the word *Helios* comes from Greek, meaning *Sun*) model at the beginning of the 16^{th} century AD. A revolutionary idea of Copernicus was that the phenomena of the epicycles could be disregarded if the position of the Sun was moved to the center, such that all the planets would revolve around a central mass. Such corrections in the model explained that the four inner planet's orbital period would be longer than that of the outer planets, hence, addressed the issue about the Mars which appeared to change orbital direction. The heliocentric model set a concept that the Earth is one of the planets among many other bodies orbiting around the Sun. The Copernican principle would greatly impact the future explorations and observations of the heavenly bodies in and outside our Solar system.

Johannes Kepler (1571 - 1630), a German mathematician and astronomer became a key figure of 17^{th} century who continued the work on Copernican revolution. Planetary motion around the Sun was debated whether or not it followed the perfect circular path. Kepler then set up mathematical equations by using the observational data from a Danish nobleman, Tycho Brahe, who showed that the planets trace out an elliptical orbits around the Sun. Kepler formulated 3 laws of planetary motion around a central body which primarily states that, (1) the planets orbit in an elliptical path with the Sun at one of the foci, (2) the line joining a planet and the Sun sweeps out equal areas in equal intervals of time, and (3) the square of the planet's period around the Sun is directly proportional to the cube of its semimajor axis.

While Kepler was analyzing data and formulating the laws of planetary motion, in Italy, Galileo Galilei (1564 - 1642) developed a telescope that would allowed him to observe heavenly bodies with far more clarity then human being had ever seen with the naked eye. Actually, Galileo did not invent the telescope, but he modified, upgraded and improved its design following the work done by Hans Lippershey, Zacharias Janseen, and Jacob Metius (King 1955). With his telescope, Galileo demon-

strated that other planets, such as Jupiter, could host smaller bodies called moons and brought forth a notion that the Earth's moon was no different than the Jupiter's moon, a common alignment observed in the Solar system. The Galilian moons (Io, Europa, Ganymede and Callisto) surprised astronomers, common people and some religious groups as well. The evidence that the Universe is not geocentric, was a bitter truth which led Galileo into a house arrest, where he died in 1642.

Sir Issac Newton was born in the same year Galileo had died. Newton (1642 - 1727), the British physicist and astronomer, is known for formulating one of the most insightful theory which explains motion of heavenly bodies. *Universal law of gravitation*, one of his most celebrated laws, provided a well defined mathematical framework to determine motion of planets around the Sun. Later, including the Moon in the picture, Newton tried to solve the 3-body problem (Sun-Earth-Moon). Apart from the well known and the well studied Newton's three laws of motion, Newton's great contribution to science includes, but not limited to, classical mechanics, calculus, spectroscopy and optics.

Mercury, Venus, Mars, Jupiter and *Saturn* are known since prehistoric era. But it was not until 16th century that the Jupiter's moons and the rings of the Saturn were discovered by Galileo's state of the art telescope. In 1781 William Herschel discovered *Uranus* making it the first planet to be found using a modern tool. By tracking the perturbed orbit of the Uranus, astronomers mathematically calculated the possible location of a perturber which later was discovered as a 8^{th} planet in the solar system, now called *Neptune*. Johann Galle is credited for the discovery of Neptune in 1846, at the precise predicted location. Such indirect method of discovering celestial bodies becomes a popular tradition, which we shall discuss in detail in the upcoming sections. The discovery of new planets shed light on exploration and understanding our Solar system in depth using modern astronomical tools and methods. The search still

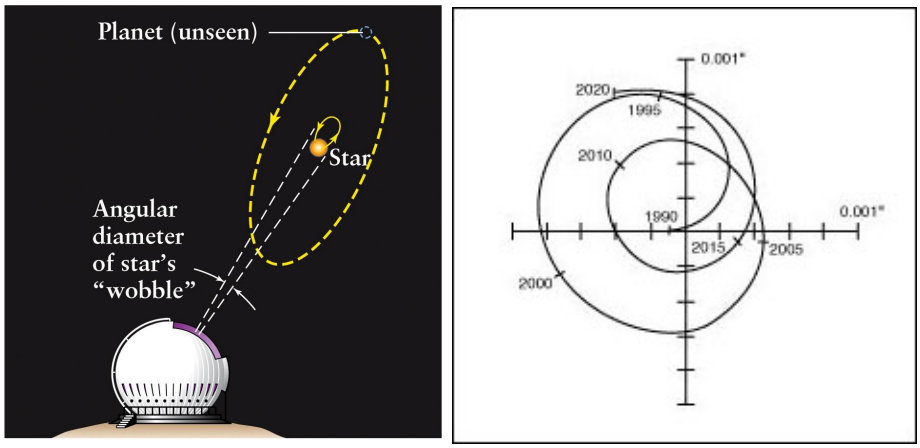

Figure 1.2. Astrometry involving the measurements of the positions and velocity of the stars. Image Credit: Rich Townsend (left), NASA JPL (right).

continues and the orbital path, location and orientation of planets are being known with very high precision.

1.3 Modern Planetary Science

After the discovery of Neptune, astronomers started to look for planet signatures outside our Solar system. These extra solar planets are referred to as *exoplanets*. The first attempted detection of such exoplanets was made using a technique called astrometry. Astrometry relies on the fact that a star experiences a force due to an unseen companion and if the proper motion or the motion projected onto the sky-plane can be measured accurately, then the existence of the unseen body can be determined. This technique was also used to detect an unseen secondary stars in binary star system. Astrometric measurements allow collecting data from distant stars using a telescope as shown in Fig. 1.2

W.S. Jacob , an astronomer working at Madras Observatory in India made some observations of the binary star system, 70 Ophiuchi, using the technique of

astrometry. It was reported that the orbital anomalies seen from the data made it highly probable that an unseen body may be existed in the system (Jacob 1855). In the year 1890, J.J. Thomas See from the University of Chicago and the United States Naval Observatory determined that a planet should exit with a 36-year period in the 70 Ophiuchi system (See 1896). The astronomical community did not take this finding of with much interest and as a result the discovery remained unknown. Other detection techniques did not exist at that time, thus all that remained was a theory to prove the credibility of those claims.

F.R. Moulton (1912) from the University of Chicago determined that the proposed planet would be unstable with the parameters observed by See, by using the framwork of the 3-body problem (Sherrill 1999). Although the astrometry technique was not accepted by the scientific community it was not rejected either. P. van de Kamp (1969) came up with a claim that there was a planet orbiting Barnard's star; however, the lack of any further evidence and proof persisted. Most of the claims on exoplanets discovery were considered erroneous prior to the contemporary age of exoplanet detection. Further advancement in science and technology gave rise to new scientific techniques that were more robust and would produce conclusive results. Some of them includes radial velocity method, transit method, gravitational lensing and direct imaging etc.

1.3.1 Radial Velocity Methods

The gravitational force from a star causes the planets to move around it in an orbit. Similarly, a planet also exerts force on the host star causing it to revolve around a counter-orbit. The size of the star's orbit depends on the size of a planet exerting force onto it's semimajor axis. For example, Jupiter induces an additional movement to the Sun with an amplitude of 13 m/s and a period of 12 years. Earth's affect is

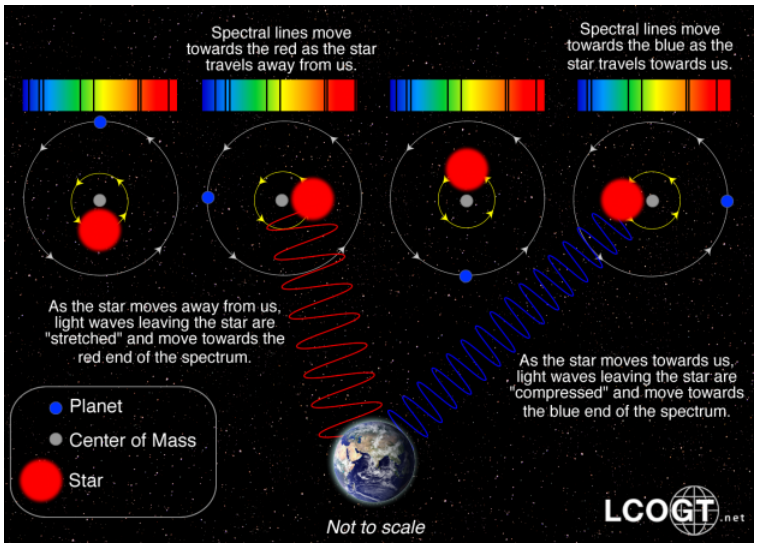

Figure 1.3. Illustration of radial velocity method used in the detection of exoplanets or secondary companion.

much smaller (0.1 m/s in 1 year). As viewed from a planet, the radial velocity of a star periodically changes when the star moves towards and away from the observer. Such back and forth movement of a star is detectable as a periodic blue shift and red shift in the star's spectral lines. In the developmental stage, radial velocity (r-v) measurements had errors of 1,000 m/s or more. Now these errors have been brought down to 1 to 10 m/s while carrying r-v measurements of exoplanets residing hundreds of light years away.

In 1988, a group of Canadian astronomers comprising of B. Campbell, G. Walker, and S. Yang (CWY88) came with subsequent confirmation of an exoplanet by using a technique that was never been used before. Using the idea of reflex motion, CWY88 used the spectral lines of the star, γ Cephei, to determine the radial velocity of the star and the unseen planet (Campbell et al. 1988). The technique is also called Doppler method since it relies on the Doppler effect described earlier. The Doppler method is illustrated in Fig. 1.3.

Due to the significant errors in the method, astronomers remained skeptical about the discovery made by CWY88. It would take several years of observations for the method to have acceptable errors, however, on the other hand, the radio astronomy took a giant leap and the first ever known exoplanet was detected around the milli-second pulsar called PSR1257 + 12 using the Arecibo Radio Telescope (Wolszczan & Frail 1992). The regularity of pulses coming from the object provided a way for measuring the reflex motion of the pulsar due to the gravitational influence of the unseen planets. As of now, three planets are confirmed to be orbiting the pulsar with the orbital periods of 25, 67 and 98 days.

The search for an exoplanet orbiting a solar-type star continued with technological advances resulting in the multiplied telescope power. On October 6, 1995, Michel Mayor and Didier Queloz from the University of Geneva became the first astronomers to detect an exoplanet orbiting the main sequence star, 51 Pegasi (Mayor & Queloz 1995). It was a Jupiter-like planet orbiting the G type star with a minimum mass of 0.47 MJ and a period of $\sim$4.23 days. Few days later the discovery was independently confirmed by Geoffrey Marcy and Paul Butler from San Francisco State University. And with that milestone, the modern planetary astronomy had just begun which would take a giant leap in the days to come.

Just as our Solar system is home to 8 planets, it was certain that there ought to be similar multi-planetary systems. The observational confirmation came from Jack Lissauer when he discovered ν Andromadae A housing 3 planets (Lissauer 1999). The fourth planet was discovered in 2011 (Curiel et al. 2011). In the next section I will show how common are the multi-planetary systems in the vicinity of our Solar system.

Despite its popularity, Doppler method had its own limitations. It would only provide information related to one degree of freedom only, i.e. the motion towards

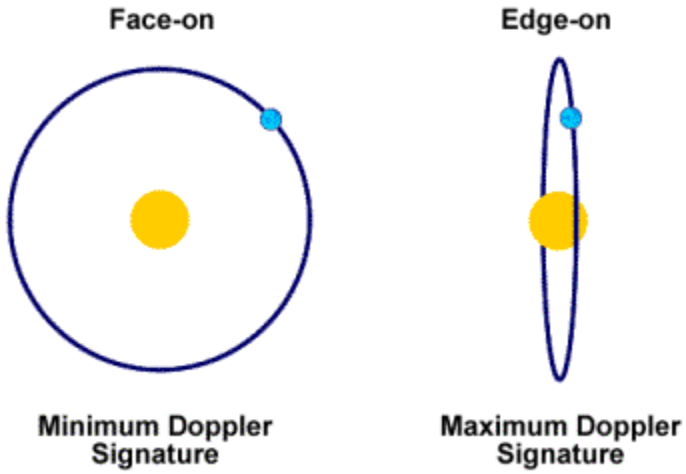

Figure 1.4. Effect of the orbital inclination on the Doppler signature as seen in the sky-plane. Image credit: UCAR.

and away from the observer. This sets a limit on the planetary mass ($M\sin i$) to its minimum. However, if the planet's orbital inclination can be obtained from the planet's spectral lines, hence its radial-velocity, the actual mass of the planet could be determined.

1.3.2 Transit Method

When a planet eclipses its host star (transits), the luminosity of the star decreases. This decrement was discovered accidentally by David Charbonneau while analyzing the brightness of star HD 209458 where he detected 1.8% drop. The change in luminosity is proportional to the size of the planet. For example, a Jupiter sized planet can potentially reduce the 1% of the light from a star. From the light curves obtained from the transit, the radius of the planet can be determined. And with the mass value obtained from the r-v methods, density of the planet is calculated. A light curve obtained from the transit method is illustrated in Fig. 1.5.

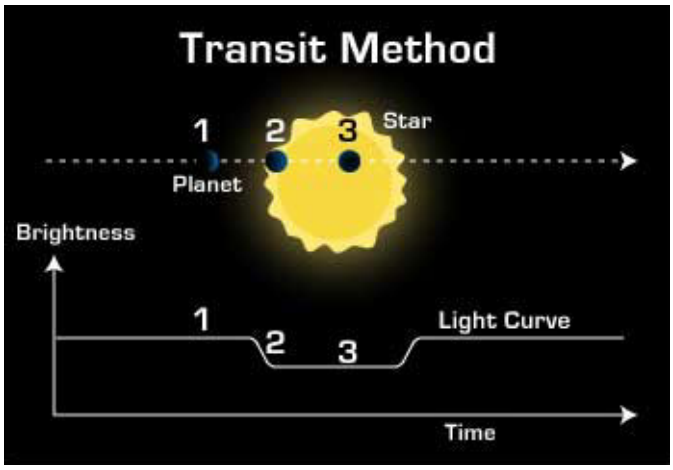

Figure 1.5. Illustration of the Transit method. Image credit: NASA.

Some limitations of the transit method includes a high occurrence of false positives due to the transient phenomena such as star spots, stellar variability, background stars, and foreground dust clouds. Three transits are required to confirm detection and account for the known sources of false positives. Independent verification using different method, such as r-v, is highly practiced in order to increase the robustness of the proposed detected planet. Other limitation is that the planetary transits are observable only when the orbit is aligned to the star from the astronomer's vantage point. For planets with smaller orbits this chance is higher, however for the larger orbits the recordable transits decreases significantly and collecting data of such transits would be painful because of the longer time period.

As of September 2014, more than 1800 exoplanets have been confirmed in single and multi-planetary systems. The National Aeronautics and Space Administration (NASA) launched a space telescope called *Kepler* in 2009 which uses the transit method to look for planet signatures and it has been the most successful mission to date. The Spitzer space telescope was at work before Kepler and it worked on the principles of Doppler method. And with more space based telescopes proposed for

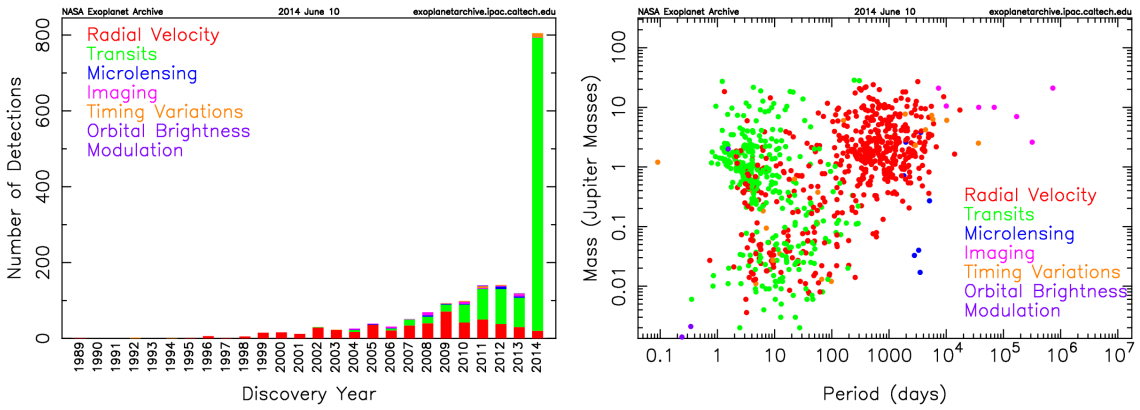

Figure 1.6. Distribution of planets detected by most of the techniques known to date. (left) Distribution of planets by year of discovery (right) Distribution of planets by their mass and orbital period.

the near future to search for transit signatures in thousands of star, these numbers are expected to grow larger.

The Doppler and Transit methods have been proven the most efficient technique for detection and characterization of exoplanets. Some other techniques which are effective but have more technical difficulties include microlensing, pulsar timing, nulling interferometry, and direct imaging. The observation from ground based telescopes always have a resolution barrier. This barrier is mainly due to turbulence in the Earth's atmosphere, also known as *seeing*. Adaptive optics have been applied to the data in order to minimize the noise due to the atmosphere. However, the best resolution measurements are made from the space based observations, thus space telescopes have higher preference.

The discovery rate of exoplanets using most of the known techniques is illustrated in Fig. 1.6.

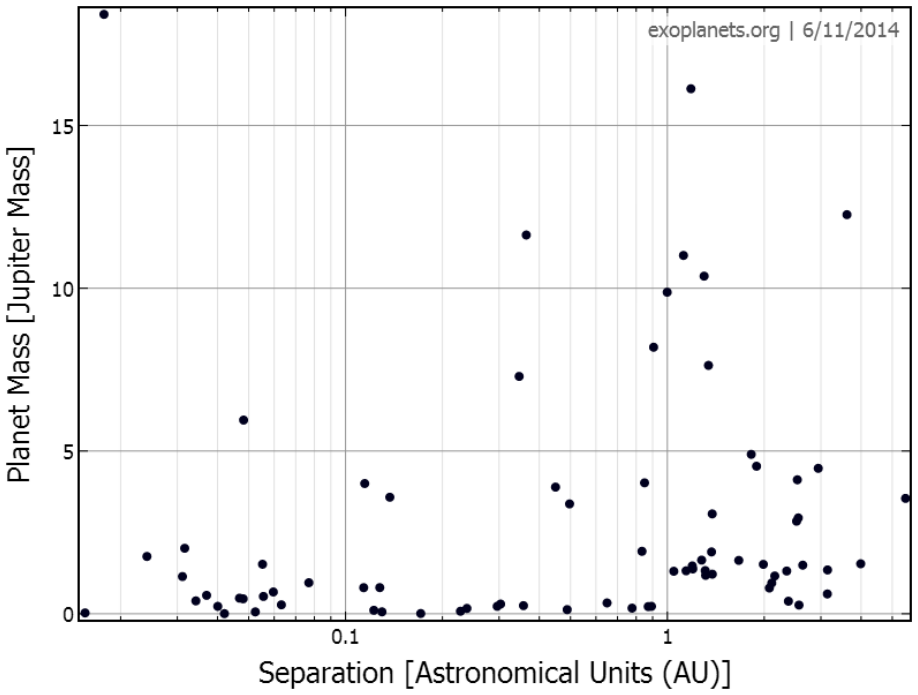

Figure 1.7. Distribution of known exoplanets in Binary Star systems.

1.4 Exoplanets in Binary Star Systems

The exoplanet discovered, but not confirmed, by the group CWY88 in 1988 happens to be a part of a binary star system called γ Cephei, which is only 45 light years away from us. Since then, approximately 79 exoplanets have been confirmed that are residing in the binary systems. Figure 1.7 illustrates the distribution of exoplanets in binary star systems as a function of planetary mass and distance from its host star. These numbers includes observations from the Doppler as well as the transit method. Prior to observations from the *Kepler* space telescope, most of the planets discovered in binary star systems were found to orbit within 5 astronomical unit (AU) from the host star, and the star separation was anywhere from 20 au to 6400 au. There were few systems where the stellar separation was less than 25 au (Patience et al. 2002; Eggenberger et al. 2004). Theoretical studies including

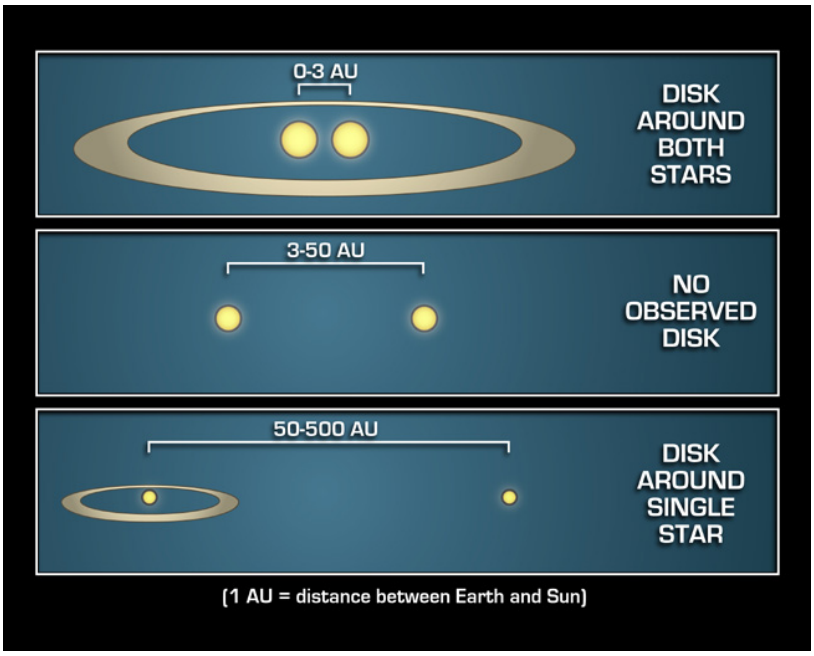

Figure 1.8. Depiction of planetary formation regimes in binary star system for varying stellar separation. Image credit: NASA.

analytical and numerical calculations showed that the existence of planets within relatively close binary systems is a possible scenario (Kley et al. 2001; Quintana et al. 2002, and others). Figure 1.8 depicts different planetary formation scenarios for various cases of binary separation, including the case for circumbinary exoplanets. Given a possible scenario for a planetary embryo to form, the studies have found that the terrestrial planet formation in such systems is possible.

Some recent observations have confirmed the existence of circumbinary planets, such as Kepler-16, Kepler-34, Kepler-35, and Kepler-47 etc (Doyle et al. 2011; Welsh et al. 2012; Orosz et al. 2012). First three systems contain a Saturnian planet. Kepler-47 is home to two known planets and two unconfirmed. I will discuss this system later with more details on its parameters and stability analysis of unconfirmed planets.

The numbers presented in Fig. 1.7 show continuous growth as the Kepler mission has observed 2,165 more eclipsing binary stars. With growing number of

planets in binaries, there is more variation and diversity among planets themselves, especially regarding the orbital elements. The study of such variational effects on the dynamics of the system is part of the motivation of this dissertation. Stability of the planet's orbital configuration as well as chaotic dynamics in presence of stellar companion will be discussed with great details.

1.5 Numerical Framework

Issac Newton introduced the topic of 3-body problem and he himself made rigorous attempts to find an analytical solutions. He tried to complete his theory related to the gravitation and motion of celestial bodies, but without any success. He was able to apply his theory to the known planets of the Solar system, but it produced inconsistent results when applied to the motion of the Moon (Sun-Earth-Moon system). He was still in the *Abacus* era, so searching for numerical solutions was beyond his scope. Several centuries later the advancement in computing technologies would allow numerical computations for not only 3-body problem but also for more general many-body (n-body) problem. Such n-body calculations using super-computers have been widely used in the current years to understand the galactic motion of the stars and has been successfully accomplished to some extent (Barnes & Hut 1986; Wisdom & Holman 1992; Aarseth 2003). Recently, n-body simulations of Milky Way and Andromeda have shown that these galaxies are on a collision course and will meet head-on after approximately 4.5 Gyr. n-body simulation primarily uses the techniques of symplectic mapping and hierarchical integration.

It may seem that with the rigorousness with which the 2 body problem was solved, adding one extra body would not change the difficulty of the problem. However, in the early 19^{th} century King Oscar II established a handsome prize for solving the n-body problem. It was awarded to an elite mathematician of the era, Henri

Poincaré, who actually did not solve the problem, and ironically his solutions even had an error (Diacu 1996). An infinite series solution was determined for the case of n= 3 by Karl Sundman (1912), but this series solution converges very slowly. As a result of these analytical shortcomings several approximations were made to simplify the problem (for details see Musielak and Quarles 2014).

Current era of exoplanet exploration in multiple configurations gives a wide variety of opportunities to conduct research and understand the dynamics of n-body systems. For the research on exoplanets presented in this dissertation, the following criteria have been set.

1. The masses are constant in time with 2 masses (M1,M2) dominating in magnitude over all other masses so that the much smaller masses do not affect the motion of the dominant masses. All other masses will be denoted in decreasing order (ie., M3, M4, ...).
2. The velocity of all the masses are small enough such that all motions will be considered non-relativistic.
3. The motion of the 2 largest masses (M1,M2) will be a solution to the 2 body problem.
4. The motion of the smaller masses may be coplanar or inclined with respect to the plane of the 2 largest masses (M1,M2).
5. To generalize the problem, the shape of the orbits are considered elliptic in most of the cases.

The first three assumptions limit the discussion to the restricted n-body problem. The general n-body problem in 3 dimensions have been studied. The motion of the 2 main bodies will be considered to be either elliptical or circular as the other cases (ie., hyperbolic and parabolic) do not produce periodic orbits. The mass regimes will be classified in terms of a comparable Solar System body such that stars will be

measured in Solar masses ($M_\odot$), giant planets will be measured in Jupiter masses (M_J), and terrestrial planets(moons) will be measured in Earth masses ($M_\oplus$). The distance between two bodies will be measured in astronomical units (AU) most of the time.

The primary question is what initial conditions in terms various orbital elements of stars or planets such as mass, semimajor axis (a), eccentricity (e), inclination (i), argument of periapsis (ω), ascending node (Ω), and mean anomly (M), will produce stable, periodic orbits for the planet being analyzed. A range of stellar masses, planetary starting positions, and other elements will be considered to address periodic, quasi-periodic or chaotic states in a very general manner.

1.6 Thesis Layout

The parameter space to address the n-body problem can be quite large and time consuming. For our systems of study the n-body problem has been confined to the cases where n = 3 to n = 6. The first project of this dissertation involves the study of the elliptic restricted 3-body problem and determining a stability criterion by using some known chaos techniques as well as some recently developed ones. Also, the new chaos technique will be tested for its integrity against other well established ones. Various binary planetary systems will be used as a test subject. The second project will explore the chaotic dynamics of a planet in a highly inclined orbits. Other sub-projects will include the detection of exomoons through observation of radio emission and stability analysis of possible new planets in GJ 832 system. The theory pertaining to these projects will be derived in detail in Chapter 2. The results of the projects will be presented and analyzed in Chapters 3,4, 5, and 6. In chapter 7 I will provide the summary and an outline of future endeavors.

CHAPTER 2

THEORY

A general *N-body problem* is used to describe motions of celestial bodies, which gravitationally interact with each other. An attempt to solve this problem first appeared in Newton's *Principia*. The simplest case of the problem is when N = 2, which is also the only case with known analytic solutions (Szebehely 1967; Murray & Dermott 1999). These two textbooks and a recent review paper by Musielak & Quarles (2014) will be extensively used to establish definitions, notations and conventions adopted in this dissertation on the circular restricted and elliptic restricted three-body problem, denoted as CRTBP and ERTBP, respectively. This chapter will focus on the theoretical aspects of Celestial Dynamics that will include the coordinate systems, the equations of motion, areas of chaos theory (Lyapunov exponents, Hill stability criterion, MEGNO maps) and numerical simulations.

2.1 Coordinate Systems

The first step in approaching the N body problem is through a choice of coordinate system. There are only a few choices when it comes to dealing with the orbital motion. The most common choices are the two types of coordinate systems: barycentric and astrocentric (Jacobi). In the barycentric coordinates, the center of mass remains fixed and the N bodies are allowed to orbit the center of mass in accordance with Newton's law of universal gravitation. Whereas the astrocentric coordinates allow one to choose the most massive body to remain fixed and motionless at the origin, hence simplifying the problem by reducing the set up to a N-1 body problem.

The first project in this dissertation, which will be discussed in details in Chapter 3, is based upon the consideration of the barycentric coordinate system. In the remaining projects, the astrocentric coordinate system is considered. However when the number of bodies N is greater than 2, there does exist another choice of coordinates. There can be a sidereal (inertial) or synodic (rotating) coordinate systems (see Figure 2.1. The usage of each of these coordinate systems varies by application and it will always be stated which of these conventions are being used. Sidereal coordinates and barycentric coordinates are interchangeable in their usage as they equally describe the same geometry. Synodic coordinates will be used mainly in application to the circular N body problem where N = 3 and will be denoted with a superscript * symbol (ie., x^*, y^*, z^*).

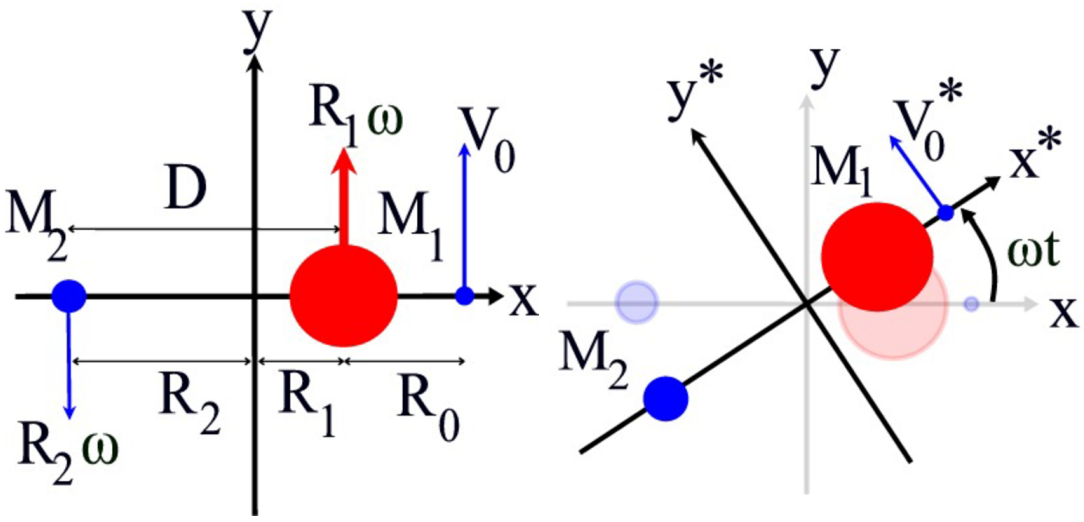

Figure 2.1. A general set up for the circular restricted three body problem. (left) Initial configuration in sidereal coordinates. (right) Initial configuration in synodic coordinates. All used symbols are described in the main text. Image Credit: Jason Eberle (2010).

2.2 Basic Definitions

Masses of astronomical bodies are denoted by M_i, where the index i describes the hierarchy of masses with $i = 1$ being the most massive object. In the description of the N body problem the total mass of the system is denoted as M where $M = M_1 + M_2 + \ldots + M_N$. Using this convention, a mass ratio may be defined, and in this dissertation the mass ratio $\mu = M_2/M$, and the complementary mass ratio $\alpha = M_1/M$. It is assumed that all the masses from M_3 to M_N will be sufficiently small so that the following relationship $\mu + \alpha = 1$ is satisfied. It is important to note that these mass ratios are dimensionless, so that they can be used in equations together with other normalized physical quantities.

Figure 2.1 illustrates the two possible coordinate systems for the CRTBP. A barycentric coordinate system is used such that the location of the two most massive bodies is denoted by R_1 and R_2 relative to the center of mass (the origin). The parameter R_0 describes location of the smaller mass, M_3, relative to the larger mass, M_1. In this setting, the most massive bodies orbit in circles with a speed $V_{1,2} = R_{1,2}\omega$ where ω, which denotes the mean motion (see below). Normalized units are often used in orbital mechanics to simplify the notation. The following set of equations demonstrates how a set of Cartesian coordinates can be normalized relative to the initial separation distance, D, between the masses and the orbital velocity in the case of negligible eccentricity. The mean motion is defined as, $\omega^2 = \frac{GM}{a^3}$ where G and a denote the constant of universal gravitation and semimajor axis between the largest masses (M_1, M_2), respectively, as given by

$$\begin{aligned} \xi &= \frac{x}{D} \quad \eta = \frac{y}{D} \quad \zeta = \frac{z}{D}, \\ \dot{\xi} &= \frac{\dot{x}}{D\omega} \quad \dot{\eta} = \frac{\dot{y}}{D\omega} \quad \dot{\zeta} = \frac{\dot{z}}{D\omega}. \end{aligned} \tag{2.1}$$

The dots in the above expressions represent the derivative with respect to time. Note also that the additional normalization is required to scale the orbital period, T. In this dissertation, the two most common choices are used, both involve redefining the value of the constant of universal gravitation, G. In the first choice $G = 4\pi^2$ because this inherently simplifies Newton's definition of Kepler's Third Law (ie., $T^2 = \frac{4\pi^2}{GM}a^3$), which also implies that some unit be chosen as well.

The second most intuitive choice is to let M be expressed in terms of $M_\odot$ and a in astronomical units (AU). The AU is equivalent to the mean distance of Earth from the Sun, which has a standard value of 1.49597870700 x 10^{11} m (Luzum et al. 2011) as defined by the International Astronomical Union (IAU). For simplicity the time unit will be equal to a Julian Earth year which has a standard value of 365.2422 days. Using the units of AU, $M_\odot$, and yr we can define $G = 4\pi^2 \frac{AU^3}{yr^2\, M_\odot}$. An alternate definition would be to change the magnitude of G to unity but leave the units unchanged, however this would change the definition of mass and force the $M_\odot = 4\pi^2$ in order for Kepler's Third Law to remain valid. Specifically, in this dissertation the first convention will be used.

2.3 Equations of Motion

From Newton's Laws of motion a general definition of force can be developed. First, considering the static gravitational problem of N masses, a general expression can be obtained to describe the force exerted on the i^{th} mass resulting from the presence of other j masses

$$\mathbf{F}_{ij} = -\frac{GM_iM_j}{r_{ij}^3}(\mathbf{r}_i - \mathbf{r}_j). \tag{2.2}$$

Equation 2.2 illustrates that the force due to gravity on the i^{th} would be directed radially inward as denoted by the difference of the vectors ($\mathbf{r}_i$,$\mathbf{r}_j$) which locate the masses relative to a point of reference. With modern numerical tools a slightly different form is required to advance the static definition to a dynamical one. As a result of Newton's 2$^{\text{nd}}$ Law, the acceleration $\mathbf{a}_{ij}$ is calculated rather than the force. A simple transformation can be obtained to define the acceleration as $\mathbf{a}_{ij} = \mathbf{F}_{ij}/M_i$. This expression is used most commonly to evaluate the N body problem, however there exists another formulation for the case where N = 3.

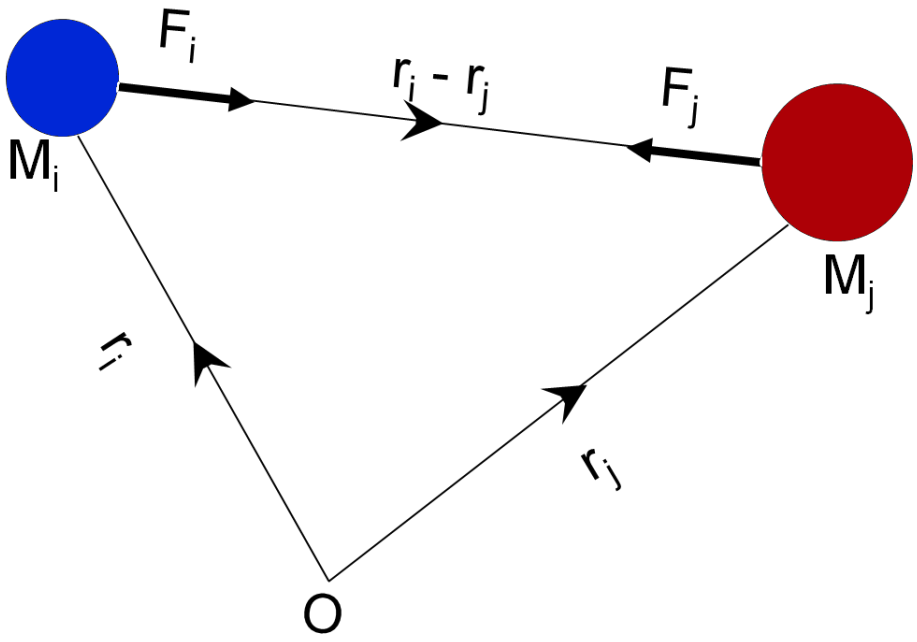

Figure 2.2. Illustrations of gravitational forces between the i^{th} and j^{th} masses.

In the CRTBP, a synodic coordinate system (see Figure 2.1b) can be used to reduce the problem to the motion of only 1 body. It is important to note that this is a simplification of the general three body problem as it is possible to rotate coordinates of the system using operations from the SO(3) group (Arfken & Weber 1995).

Specifically a rotation matrix can be applied with respect to the z-axis. However, the equations of motion must be defined in the sidereal coordinate system (ξ, η, ζ) in order to apply the resulting transformation. Using the vector form of Equation 2.2, the equations of motion of the third mass are

$$\ddot{\xi} = GM\left[\frac{\alpha\left(\xi_1 - \xi\right)}{r_1^3} + \frac{\mu\left(\xi_2 - \xi\right)}{r_2^3}\right], \tag{2.3}$$

$$\ddot{\eta} = GM\left[\frac{\alpha\left(\eta_1 - \eta\right)}{r_1^3} + \frac{\mu\left(\eta_2 - \eta\right)}{r_2^3}\right], \tag{2.4}$$

$$\ddot{\zeta} = GM\left[\frac{\alpha\left(\zeta_1 - \zeta\right)}{r_1^3} + \frac{\mu\left(\zeta_2 - \zeta\right)}{r_2^3}\right], \tag{2.5}$$

where

$$r_1^2 = \left(\xi_1 - \xi\right)^2 + \left(\eta_1 - \eta\right)^2 + \left(\zeta_1 - \zeta\right)^2, \tag{2.6}$$

$$r_2^2 = \left(\xi_2 - \xi\right)^2 + \left(\eta_2 - \eta\right)^2 + \left(\zeta_2 - \zeta\right)^2. \tag{2.7}$$

The necessary rotation matrix, R_{ab}, is given by

$$R_{ab} = \begin{pmatrix} \cos\theta & \sin\theta & 0 \\ -\sin\theta & \cos\theta & 0 \\ 0 & 0 & 1 \end{pmatrix}. \tag{2.8}$$

Equation 2.8 gives the general form of the necessary rotation matrix. The CRTBP requires a specific form which involves making the substitution $\theta = \omega t$. This substitution is not permitted in the ERTBP, because the latter does not permit this due to Kepler's 2$^{\text{nd}}$ Law of planetary motion that changes ω from a constant into a time dependent parameter. In the following, it is shown how the equations of motion

are determined for the CRTBP and then the appropriate modifications are made to satisfy the ERTBP.

First, the sidereal coordinates (ξ, η, ζ) are rotated using Equation 2.8 with the aforementioned transformation

$$\begin{pmatrix} \xi^* \\ \eta^* \\ \zeta^* \end{pmatrix} = \begin{pmatrix} \cos\omega t & \sin\omega t & 0 \\ -\sin\omega t & \cos\omega t & 0 \\ 0 & 0 & 1 \end{pmatrix} \begin{pmatrix} \xi \\ \eta \\ \zeta \end{pmatrix} \tag{2.9}$$

If we now differentiate Equation 2.9 twice, we obtain the following accelerations $(\ddot{\xi}^*, \ddot{\eta}^*, \ddot{\zeta}^*)$

$$\begin{pmatrix} \ddot{\xi}^* \\ \ddot{\eta}^* \\ \ddot{\zeta}^* \end{pmatrix} = \begin{pmatrix} \cos\omega t & \sin\omega t & 0 \\ -\sin\omega t & \cos\omega t & 0 \\ 0 & 0 & 1 \end{pmatrix} \begin{pmatrix} \ddot{\xi} - 2\omega\dot{\eta} - \omega^2\xi \\ \ddot{\eta} + 2\omega\dot{\xi} - \omega^2\eta \\ \ddot{\zeta} \end{pmatrix} \tag{2.10}$$

Using Equations 2.3, 2.4, and 2.5 substitutions can be made to obtain the following equations of motion in the synodic coordinate system

$$\ddot{\xi}^* - 2\omega\dot{\eta}^* - \omega^2\xi^* = -GM\left[\alpha\frac{\xi^* + GM\mu}{r_1^3} + \mu\frac{\xi^* - GM\alpha}{r_2^3}\right], \tag{2.11}$$

$$\ddot{\eta}^* - 2\omega\dot{\xi}^* - \omega^2\eta^* = -GM\left[\frac{\alpha}{r_1^3} + \frac{\mu}{r_2^3}\right]\eta, \tag{2.12}$$

$$\ddot{\xi}^* = -GM\left[\frac{\alpha}{r_1^3} + \frac{\mu}{r_2^3}\right]\zeta, \tag{2.13}$$

where (r_1, r_2) are redefined as

$$\begin{aligned} r_1^2 &= (\xi^* + GM\mu)^2 + \eta^{2*} + \zeta^{2*}, \\ r_2^2 &= (\xi^* - GM\alpha)^2 + \eta^{2*} + \zeta^{2*}. \end{aligned} \tag{2.14}$$

It is important to note that as a result of the synodic reference frame the Coriolis and centrifugal acceleration are introduced into the equations of motion. In addition, Equations 2.11, 2.12, and 2.13 can be written as the gradient of a psuedopotential U:

$$\begin{aligned} \ddot{\xi}^* - 2\omega\dot{\eta}^* &= \frac{\partial U}{\partial \xi^*}, \\ \ddot{\eta}^* + 2\omega\dot{\xi}^* &= \frac{\partial U}{\partial \eta^*}, \\ \ddot{\zeta}^* &= \frac{\partial U}{\partial \zeta^*}, \end{aligned} \tag{2.15}$$

where $U = U\left(\xi^*, \eta^*, \zeta^*\right)$ is given by

$$U = \frac{\omega^2}{2}\left(\xi^{2*} + \eta^{2*}\right) + GM\left(\frac{\alpha}{r_1} + \frac{\mu}{r_2}\right). \tag{2.16}$$

The equations of motion in the ERTBP are similar to those of the CRTBP but there are some important differences between them. First of which is that in the ERTBP the true anomaly, f, is incorporated into the equations of motion because Kepler's 2^{nd} Law forces f to vary with time. This also implies that the synodic coordinate system cannot be rotated at a constant rate. Thus an additional equation of motion must be included to determine f at each instant of time. Moreover,the eccentricity also effects the equations of motion so that the CRTBP psuedopotential U becomes the ERTBP psuedopotential Ω given by

$$\Omega = (1 + e\cos f)^{-1}\left[\frac{1}{2}\left(\xi^{2*} + \eta^{2*} - e\zeta^{2*}\cos f\right) + GM\left(\frac{\alpha}{r_1} + \frac{\mu}{r_2}\right) + \frac{\mu\alpha}{2}\right], \tag{2.17}$$

and

$$\dot{f} = \frac{GM^{\frac{1}{2}}}{[a(1-e^2)]^{\frac{3}{2}}}(1 + e\cos f)^2. \tag{2.18}$$

2.4 Orbital Elements

An alternate method of analyzing the problems described above can be found in celestial dynamics. When a clear hierarchy of mass is considered as in the CRTBP and ERTBP, it is useful to describe the system in terms of the orbital elements of each body. The orbital elements are also constants of motion for the appropriate two body problem. In the three body problem orbital elements are defined relative to a Jacobi coordinate system with the most massive body is taken to be the reference. Therefore M_2 and M_3 would have each a set of orbital elements relative to M_1.

For the two body problem the orbital elements are the semimajor axis (a), inclination (I), eccentricity (e), argument of periapsis (ω), longitude of ascending node (Ω), and true anomaly (f).

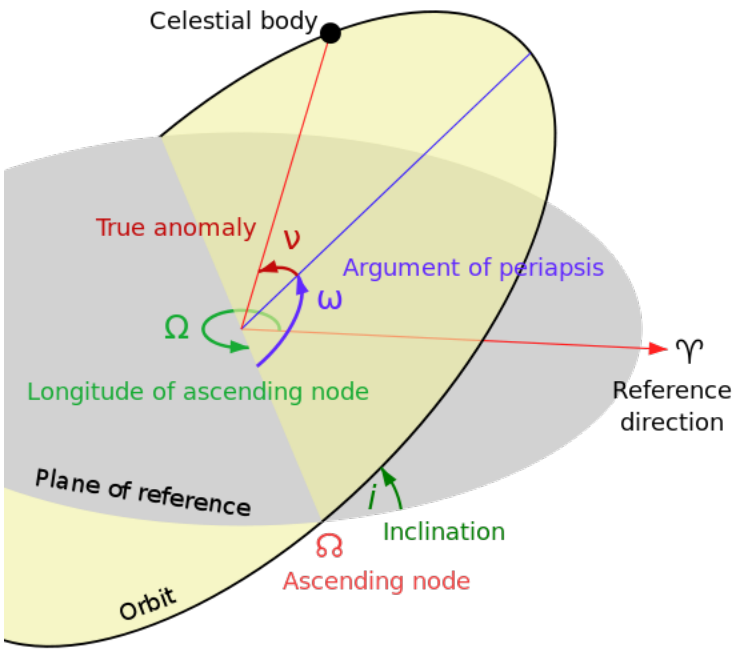

Figure 2.3. Illustration of the orbital elements that exist in a system that is not coplanar. Image Credit: Wikipedia.

At any given time the position of the planet is given as (Murray & Dermott 1999)

$$\begin{pmatrix} X \\ Y \\ Z \end{pmatrix} = r \begin{pmatrix} \cos\Omega\cos(\omega+f) - \sin\Omega\cos i\sin(\omega+f) \\ \sin\Omega\cos(\omega+f) + \cos\Omega\cos i\sin(\omega+f) \\ \sin i\sin(\omega+f) \end{pmatrix}$$

Then the velocities can be calculated by taking the time derivative of the above position matrix

$$\begin{aligned} V_x &= -r(\dot{\omega}+\dot{f})\left[\cos\Omega\sin(\omega+f) + \sin\Omega\cos i\cos(\omega+f)\right] \\ &\quad + r\dot{\Omega}\left[\cos\Omega\cos i\sin(\omega+f) - \sin\Omega\cos(\omega+f)\right] - r\dot{i}\left[\sin\Omega\sin i\sin(\omega+f)\right] \\ &\quad + \left[\cos\Omega\cos(\omega+f) - \dot{r}\sin\Omega\cos i\sin(\omega+f)\right] \end{aligned} \tag{2.19}$$

$$\begin{aligned} V_y &= -r\left[\sin\Omega\sin(\omega+f)\dot{\omega} + \dot{f} - \cos\Omega\cos(\omega+f)\dot{\Omega}\right] \\ &\quad + r\left[\cos\Omega\cos i\cos(\omega+f)\dot{\omega} + \dot{f} - \cos\Omega\sin i\sin(\omega+f)\dot{i} - \sin\omega\cos i\sin(\omega+f)\dot{\omega}\right] \\ &\quad + \dot{r}\left[\sin\Omega\cos(\omega+f) + \cos\Omega\cos i\sin(\omega+f)\right] \end{aligned} \tag{2.20}$$

$$V_z = r\left[\cos(\omega+f)\sin i(\dot{\omega}+\dot{f}) + \dot{i}\cos i\sin(\omega+f)\right] + \dot{r}\left[\sin(\omega+f)\sin i\right] \tag{2.21}$$

Applying the initial conditions

$$\dot{\Omega} = \dot{\omega} = \dot{i} = 0 \qquad \text{and}$$

$$\dot{f} = \frac{na}{r\sqrt{1-e^2}}\left(1 + e\cos f\right) \tag{2.22}$$

Equations (1), (2) and (3) become

$$
\begin{aligned}
V_x &= \frac{na}{\sqrt{1-e^2}} \{e \sin f \left[\cos\Omega \cos(\omega+f) - \sin\Omega \cos i \sin(\omega+f)\right] - \\
&\qquad (1+e\cos f)\left[\cos\Omega \sin(\omega+f) + \sin\Omega \cos i \cos(\omega+f)\right]\} \\
V_y &= \frac{na}{\sqrt{1-e^2}} \{e \sin f \left[\sin\Omega \cos(\omega+f) + \cos\Omega \cos i \sin(\omega+f)\right] + \\
&\qquad (1+e\cos f)\left[\cos\Omega \cos i \cos(\omega+f) - \sin\Omega \sin(\omega+f)\right]\} \\
V_z &= \frac{na}{\sqrt{1-e^2}} \sin i \left[\cos(\omega+f)(1+e\cos f) + \sin(\omega+f) e \sin f\right]
\end{aligned} \tag{2.23}
$$

Figure 2.3 shows the orbital elements that they are non-zero in the case of orbits that are not coplanar. The remaining orbital elements exist regardless of the reference plane. Using Lagrange's planetary equations, a system can be simulated with respect to the orbital elements (Murray & Dermott 1999) which is an optional parameter in integration packages such as Mercury and Swifter. This dissertation makes use of how the orbital elements can change with time due to the nonlinearity of the N body problem. As such, the simulations are performed within the previously defined coordinates systems and appropriate conversions are made to the corresponding orbital elements using the orbital state vectors. More details concerning these transformations are given in Appendix A.

2.5 Zero Velocity Surface and Functions

The Zero Velocity Surface (ZVS) is used in the CRTBP to define the region of space where the third mass is allowed to move. For the elliptic case a Zero Velocity Function (ZVF) is employed that is dependent on the true anomaly, f, of the two more massive bodies. Both the ZVS and ZVF are determined from the corresponding Jacobi integral.

The Jacobi integral in the CRTBP produces the so-called Jacobi constant, C_J. This comes from multiplying Equation 2.11 by $\dot{\xi}^*$, Equation 2.12 by $\dot{\eta}^*$, Equation 2.13 by $\dot{\zeta}^*$, and summing the results together to get

$$\dot{\xi}^*\ddot{\xi}^* + \dot{\eta}^*\ddot{\eta}^* + \dot{\zeta}^*\ddot{\zeta}^* = \frac{dU}{dt}. \tag{2.24}$$

Equation 2.24 can thus be integrated to give

$$\begin{aligned} \dot{\xi}^{2*} + \dot{\eta}^{2*} + \dot{\zeta}^{2*} &= 2U - C_J, \\ v^2 &= 2U - C_J. \end{aligned} \tag{2.25}$$

Therefore, the ZVS can be formally defined as the points for which $v = 0$ or $2U = C_J$. To draw the appropriate contours, the value of C_J is determined from the initial conditions and then the previous condition is applied. Also the quantity C_J becomes a constant of motion for the CRTBP. Regions beyond the ZVS or forbidden regions are not allowed because to enter such regions would imply a purely imaginary velocity, which obviously corresponds to an unphysical solution.

The generalized ZVF is an extension of the ZVS that incorporates the parameters for eccentricity and true anomaly. This is determined in a similar manner but with $C_J(f)$ rather than only a constant C_J. It is easily written by replacing the psuedopotential U with Ω as given in Equation 2.17 to produce the relation $C_J(f) = 2\Omega(\xi^*, \eta^*, \zeta^*, f)$. Solving analytically the integrals for $C_J(f)$ can be especially daunting but numerical methods exist and a Hill-stability criterion has been formulated based on the numerical result (Szenkovits & Makó 2008).

2.6 Tools from Chaos Theory

Chaos theory has been effectively applied to different astronomical problems, including some problems of orbital mechanics. Many of these applications have been explored in the study of asteroids within the Solar System. In this dissertation, certain techniques that have been developed starting in the 1980s (Benettin et al. 1980; Froeschle 1984; Ferraz-Mello & Dvorak 1987; Dvorak & Karch 1988; Smith & Szebehely 1993; Murray & Holman 2001, and references therein) will be utilized. Specifically, the theory for the calculation of Lyapunov exponents will be described as well as a brief introduction to linear stability theory and perturbation theory.

2.7 Fourier Transform

Some of the basic tools for the analysis in chaos theory comes from advancements made prior to its development. One of those great achievements is called the Fourier transform (Fourier 1822). This mathematical tool was developed by Jean Baptiste Fourier to study the time evolution of heat diffusion. However, the use of this tool has been extended to much broader applications including the analysis of a time series. The basic definition of the Fourier transform involves a time dependent function $\chi(t)$. This function can exist in another mathematical space called *phase space* where the frequency becomes the independent coordinate. The Fourier transform demonstrates mathematically how to obtain the form of the function in both spaces, position and phase. This relationship is given by

$$\chi(t) = \int_{-\infty}^{\infty} F(f) e^{2i\pi ft} df, \tag{2.26}$$

$$F(f) = \int_{-\infty}^{\infty} \chi(t) e^{-2i\pi ft} dt. \tag{2.27}$$

The Fourier transform (Equation 2.26) and the inverse Fourier transform (Equation 2.27) provide an analytic means of performing analysis upon a source function. As it can take quite a long time to calculate the Fourier transform for a general function, numerical techniques were introduced. The fast Fourier transform (FFT) was introduced in the 1960s and the Cooley-Tukey algorithm is one of the most commonly used (Cooley & Tukey 1965). However, it was later discovered that this algorithm was merely reinvented and originally determined by Gauss in 1805 (Heideman et al. 1984). Since numerical techniques evolve over time there is another computational library which has made the FFT the most optimized into the FFT of the west (FFTW). FFTW (Frigo & Johnson 1998) has undergone 3 distinct versions to the current version FFTW3 (Frigo & Johnson 2005). This dissertation heavily uses this particular tool and the libraries of FFTW in the software package Matlab® (MATLAB 2011).

The importance of the use of the FFT is that it can differentiate a periodic source into three categories: noisy, quasi-periodic, and periodic signals (Tsonis 1992). A noisy signal is indicated by the lack of a specific frequency that would dominate over all other frequency in the time series. A periodic signal will show one distinct frequency that will dominate over all others in an appropriate power spectrum. A quasi-periodic signal can be characterized as the linear combination of many frequencies which is represented in a power spectrum by many frequencies dominating over the background (noise). Since the objects in the N body problem experience periodic influences from their neighbors this tool is appropriate in such research.

2.8 Linear Stability

The N body problem exhibits inherent nonlinear behavior, but whether that nonlinear behavior will lead to instability is a topic of current research. The most common first step in trying to determine the stability of a nonlinear system is to

approximate the system as linear over a sufficiently small time. This section outlines the basics of linear stability theory to provide the necessary background to discuss future nonlinear analysis methods.

Linear systems in mathematics are generally studied using a set of coupled first order differential equations. Let us consider, for example, a set of two linear, first order homogeneous differential equations:

$$\begin{aligned} \dot{x_1} &= a_{11}x_1 + a_{12}x_2, \\ \dot{x_2} &= a_{21}x_1 + a_{22}x_2, \end{aligned} \tag{2.28}$$

where a_{ij} represent constants. Equation 2.28 can be rewritten into a matrix form, $\dot{\mathbf{x}} = A\mathbf{x}$, where

$$A = \begin{pmatrix} a_{11} & a_{12} \\ a_{12} & a_{22} \end{pmatrix} \qquad \mathbf{x} = \begin{pmatrix} x_1 \\ x_2 \end{pmatrix} \qquad \dot{\mathbf{x}} = \begin{pmatrix} \dot{x_1} \\ \dot{x_2} \end{pmatrix} \tag{2.29}$$

Considering that the solution to the scalar equation $\dot{x} = ax$ exists, we should assume a similar solution as it matches the form of $\dot{\mathbf{x}}$ which is

$$\mathbf{x}(t) = \mathbf{c}e^{\lambda\, t}, \tag{2.30}$$

where λ is a scalar and $\mathbf{c}$ is a nonzero vector $\binom{c_1}{c_2}$. Substituting this solution into $\dot{\mathbf{x}}$ the result is obtained as $A\mathbf{c} = \lambda\mathbf{c}$ with the eigenvector λ. A nontrivial solution is desired, thus properties of matrices are used from linear algebra including the Identity matrix I. It is necessary that

$$\mathrm{Det}(A - \lambda\, I) = 0. \tag{2.31}$$

Equation 2.31 can be solved using the appropriate coefficients from A and the eigenvector λ. The solution results in a characteristic equation in terms of λ in the form

$$\lambda^2 + \lambda \,\text{Trace}\, A + \text{Det}\, A = 0. \tag{2.32}$$

The property of Equation 2.32 which is important is that the eigenvalues λ_1, λ_2 are either both real or complex, which corresponds to the exponential and oscillatory solutions, respectively. Also we can solve for the eigenvalues using the general solution to a quadratic equation so that

$$\lambda_{1,2} = \frac{\text{Trace}\, A - \sqrt{(\text{Trace}\, A)^2 - 4\,\text{Det}\, A}}{2} \tag{2.33}$$

Equation 2.33 provides two important properties that are used in this dissertation. It can easily be shown that

$$\begin{aligned} \lambda_1 \lambda_2 &= \text{Det}\, A \\ \lambda_1 + \lambda_2 &= \text{Trace}\, A \end{aligned} \tag{2.34}$$

The result given by Equation 2.34 holds true for a general homogeneous system of n first order differential equations.

2.9 Nonlinear Stability

When dealing with nonlinear systems, an analytic solution is usually not obtainable. In this case the system is expressed in terms of a set of nonlinear functions

of the appropriate coordinates. Again we use the form $\dot{\mathbf{x}} = A\mathbf{x}$, however the elements of $\dot{\mathbf{x}}, A$, and $\mathbf{x}$ will be considered to be n dimensional such that

$$A = \begin{pmatrix} a_{11} & a_{12} & \cdots & a_{1n} \\ a_{21} & a_{22} & \cdots & a_{2n} \\ \vdots & \vdots & & \vdots \\ a_{n1} & a_{n2} & \cdots & a_{nn} \end{pmatrix} \tag{2.35}$$

Applying Equation 2.31 to Equation 2.35 and assuming $\mathbf{x}$ to contain n nonlinear functions dependent on n coordinates, it can be shown that the matrix A represents the Jacobian matrix J, ie., $A = J$. Then Equation 2.35 becomes

$$A = \begin{pmatrix} \frac{\partial f_1}{\partial x_1} & \frac{\partial f_1}{\partial x_2} & \cdots & \frac{\partial f_1}{\partial x_n} \\ \frac{\partial f_2}{\partial x_1} & \frac{\partial f_2}{\partial x_2} & \cdots & \frac{\partial f_2}{\partial x_n} \\ \vdots & \vdots & & \vdots \\ \frac{\partial f_n}{\partial x_1} & \frac{\partial f_n}{\partial x_2} & \cdots & \frac{\partial f_n}{\partial x_n} \end{pmatrix} \tag{2.36}$$

Nonlinear systems are usually categorized as being either conservative or dissipative. This is determined by the Hamiltonian and some properties of the Jacobian. First, the category can be determined by inspection of the Hamiltonian for time dependence. Dynamical systems whose Hamiltonian does not vary with time are designated as being conservative. Otherwise, the system is considered to be dissipative. The Hamiltonian of the gravitational N body problem is time independent, thus the results obtained in this dissertation are within the conservative regime of nonlinear dynamics.

Conservative systems have some useful properties, the most important for this dissertation is the conservation of volumes in phase space. This is shown by con-

sidering the N body problem to be like a fluid. Thus using generalized coordinates (q,p), which represent phase space, the density ρ of the fluid at a time t with the fluid moving with a velocity $\mathbf{v}$ obeys the following continuity equation

$$\frac{\partial \rho}{\partial t} + \nabla \cdot (\rho \mathbf{v}) = 0. \tag{2.37}$$

In order to solve Equation 2.37, the variable dependence must be determined. The density has the form $\rho = \rho(q, p, t)$ and the velocity has the form $\mathbf{v} = \mathbf{v}(q, p)$ such that the chain rule can be applied

$$\nabla \cdot (\rho \mathbf{v}) = \mathbf{v}(\nabla \cdot \rho) + \rho(\nabla \cdot \mathbf{v}). \tag{2.38}$$

Recalling that for the conservative systems $\nabla \cdot \mathbf{v} = 0$, the resulting equation becomes

$$\nabla \cdot (\rho \mathbf{v}) = \mathbf{v}(\nabla \cdot \rho). \tag{2.39}$$

Substituting Equation 2.39 into Equation 2.37 and rewriting in terms of the full time derivative

$$\frac{\mathrm{d}\rho}{\mathrm{d}t} = 0. \tag{2.40}$$

Since $m = \rho V$, where V denotes volume and m is constant with respect to time, the result is $\frac{\mathrm{d}V}{\mathrm{d}t} = 0$. This demonstrates that the volume in phase space is conserved, which indicates that the Trace $A = 0$. Using a generalization of Equation 2.34, the resulting eigenvalues can be shown to have the following property

$$\lambda_1 + \lambda_2 + \ldots + \lambda_n = 0. \tag{2.41}$$

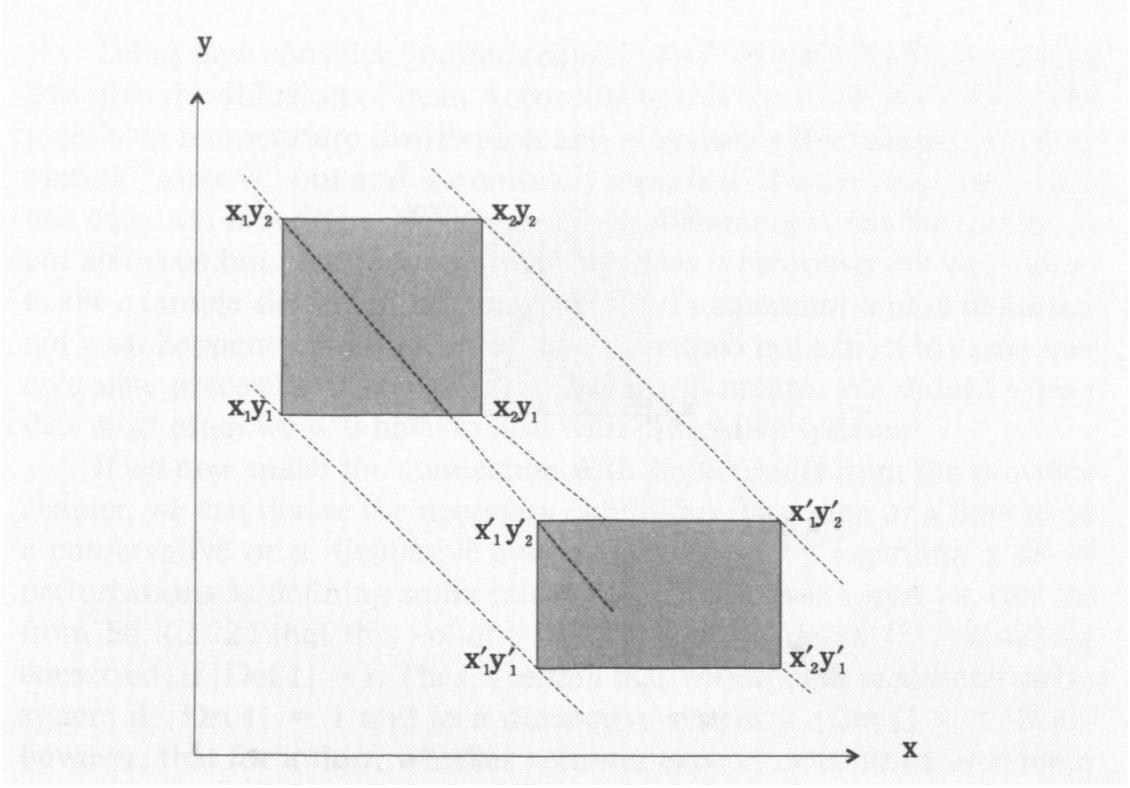

Figure 2.4. Illustration of the conservation of volumes in the phase space (x,y). The volumes may be deformed, but they remain the same. Image Credit: Anastasios Tsonis (1992).

2.10 Lyapunov Exponent

In the analysis of nonlinear phenomena, many different methods exist to gauge the stability within a nonlinear system. One such method involves the calculation and interpretation of the Lyapunov exponents (Lyapunov 1907). This dissertation uses this method to determine the timescale for which a particular system is deterministic and as a stability criterion. The Lyapunov exponents are a measure of the change in nearby trajectories differentiated by initial conditions (See Figure 2.5). This description is analogous to the eigenvalues given in Equation 2.33 and display the same properties as given in Equation 2.34. The positive Lyapunov exponents measure the rate of divergence of neighboring orbits, whereas negative exponents measure conver-

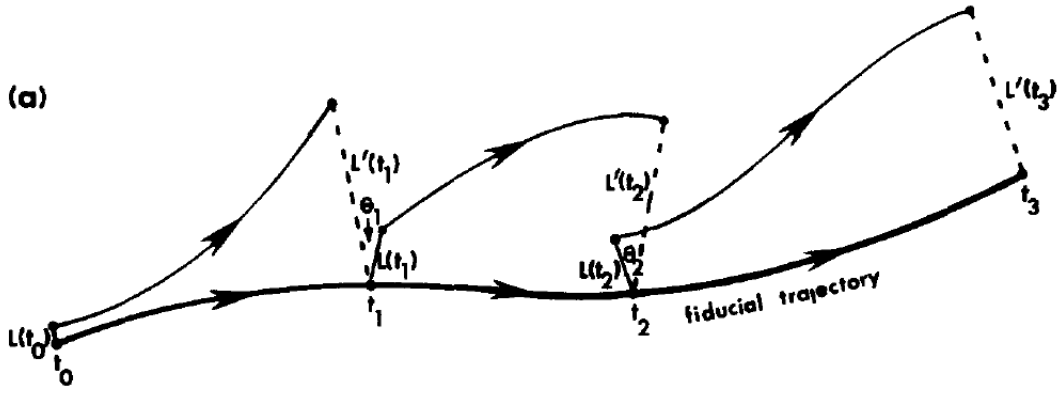

Figure 2.5. Illustration of the variations of nearby trajectories that define the Lyapunov exponents. Image Credit: Wolf et al. (1985).

gence rates between stable manifolds. For dissipative dynamical systems the sum of all Lyapunov exponents is less than 0 (e.g., Musielak & Musielak 2009); however, for Hamiltonian (non-dissipative) systems the sum is equal to 0 (e.g., Hilborn & Sprott 1994). In addition the inverse of the maximum Lyapunov exponent will provide an estimate of how long a system will remain deterministic or a measure of predictive time (Musielak & Musielak 2009).

Specific applications of the Lyapunov exponents to the CRTBP have been discussed by many authors, including Gonczi & Froeschle (1981), Jefferys & Yi (1983), Lecar et al. (1992), Milani & Nobili (1992), Smith & Szebehely (1993) and Murray & Holman (2001). In order to use the method of Lyapunov exponents on the gravitational N body problem, the Jacobian A must be defined for such a system. Since there exists two possible types of barycentric coordinate systems (sidereal and synodic), the Jacobian is defined for both and each one is used with the appropriate coordinate system. In the case of the synodic barycentric system, the third mass has its own Jacobian, where as the sidereal case each mass has its own Jacobian.

A dynamical system with n degrees of freedom is represented in $2n$ phase space; thus, to fully determine stability of the system all $2n$ Lyapunov exponents must be calculated. The previously obtained results for the CRTBP clearly show that the Lyapunov exponents can be calculated for the case of the CRTBP, for which we have $2n = 6$. This requires a state vector, $\mathbf{x}$, for the system containing 6 elements $(\xi, \eta, \zeta, \dot{\xi}, \dot{\eta}, \dot{\zeta})$. It is the convention that positive Lyapunov exponents indicate that both dissipative (e.g., Hilborn & Sprott 1994) and non-dissipative (e.g., Ozorio de Almeida 1990) systems are chaotic. In this dissertation, the end value of the maximum Lyapunov exponent in a time series is used to make distinction between chaotic and non-chaotic orbits. The synodic Jacobian uses the equations of motion given by Equation 2.15 with

$$A = \begin{pmatrix} 0 & 0 & 0 & 1 & 0 & 0 \\ 0 & 0 & 0 & 0 & 1 & 0 \\ 0 & 0 & 0 & 0 & 0 & 1 \\ \frac{\partial \ddot{\xi}^*}{\partial \xi^*} & \frac{\partial \ddot{\xi}^*}{\partial \eta^*} & \frac{\partial \ddot{\xi}^*}{\partial \zeta^*} & 0 & 2 & 0 \\ \frac{\partial \ddot{\eta}^*}{\partial \xi^*} & \frac{\partial \ddot{\eta}^*}{\partial \eta^*} & \frac{\partial \ddot{\eta}^*}{\partial \zeta^*} & -2 & 0 & 0 \\ \frac{\partial \ddot{\zeta}^*}{\partial \xi^*} & \frac{\partial \ddot{\zeta}^*}{\partial \eta^*} & \frac{\partial \ddot{\zeta}^*}{\partial \zeta^*} & 0 & 0 & 0 \end{pmatrix}. \tag{2.42}$$

Using the synodic Jacobian is useful to investigate the CRTBP and ERTBP, but it cannot be used to investigate a N body problem. Thus the Jacobian in the sidereal barycentric coordinates can be generalized as

$$A_i = \begin{pmatrix} 0 & 0 & 0 & 1 & 0 & 0 \\ 0 & 0 & 0 & 0 & 1 & 0 \\ 0 & 0 & 0 & 0 & 0 & 1 \\ \frac{\partial \ddot{\xi}_i}{\partial \xi_i} & \frac{\partial \ddot{\xi}_i}{\partial \eta_i} & \frac{\partial \ddot{\xi}_i}{\partial \zeta_i} & 0 & 0 & 0 \\ \frac{\partial \ddot{\eta}_i}{\partial \xi_i} & \frac{\partial \ddot{\eta}_i}{\partial \eta_i} & \frac{\partial \ddot{\eta}_i}{\partial \zeta_i} & 0 & 0 & 0 \\ \frac{\partial \ddot{\zeta}_i}{\partial \xi_i} & \frac{\partial \ddot{\zeta}_i}{\partial \eta_i} & \frac{\partial \ddot{\zeta}_i}{\partial \zeta_i} & 0 & 0 & 0 \end{pmatrix}. \tag{2.43}$$

The sidereal Jacobian, A_i, carries with it an index to denote the Jacobian for the i^{th} mass. Also, it is important to note that Equation 2.43 can be represented by 4 matrices with 3 x 3 elements so that the null matrices (top left and bottom right) can be excluded to reduce the number of calculations. Additionally, Equations 2.3, 2.4, and 2.5 provide the necessary accelerations to evaluate the sidereal Jacobian, A_i. However, the number of calculations will increase as N increases so that the usage of A_i can become computationally expensive.

The details of the calculation of the Lyapunov exponents can be found in Appendix A. The particular algorithm used in the calculations is adapted from an algorithm given by Wolf et al. (1985). This algorithm uses Gram-Schmidt renormalization which can become computationally expensive. Alternate methods using Lyapunov exponents as a basis of analysis have been introduced (Froeschle 1984; Laskar et al. 1992; Lohinger et al. 1993; Lohinger & Froeschle 1993; Froeschlé et al. 1997; Froeschlé & Lega 2000; Fouchard et al. 2002, and references therein). The most commonly used

alternative is the fast Lyapunov indicator (FLI) which measures the largest change in the tangent vector $\dot{\mathbf{x}}$. The FLI is calculated via the expression

$$\mathrm{FLI} = \sup_{0<k<T} \log \left\| \dot{\mathbf{x}}_k(t) \right\| . \tag{2.44}$$

Usage of the FLI is much less computationally expensive to the calculation of the Lyapunov exponents via the Wolf method (Wolf et al. 1985) due to the fact that it involves only evaluations and not the integration of the tangent vector, $\dot{\mathbf{x}}$. Other methods include the relative Lyapunov indicator, orthogonal FLI, and the orthogonal FLI_2. This dissertation uses the full Lyapunov exponent spectrum for much of the analysis as it was developed for the simulation methods by Eberle (2010).

2.11 Perturbation Theory

The evaluation of resonant phenomena often requires analysis considering perturbation theory. This section will provide a brief introduction to the theory along with a description of possible numerical applications. Perturbation theory assumes that the accelerations of the lesser massive bodies (M_2, M_3)are dominated by a central or primary body. This implies that the motions of (M_2, M_3) result in conic sections with small deviations due to their mutual gravitational perturbations (Murray & Dermott 1999). The assumption considers a disturbing function, R, which can be introduced to account for the interaction terms of the perturbation.

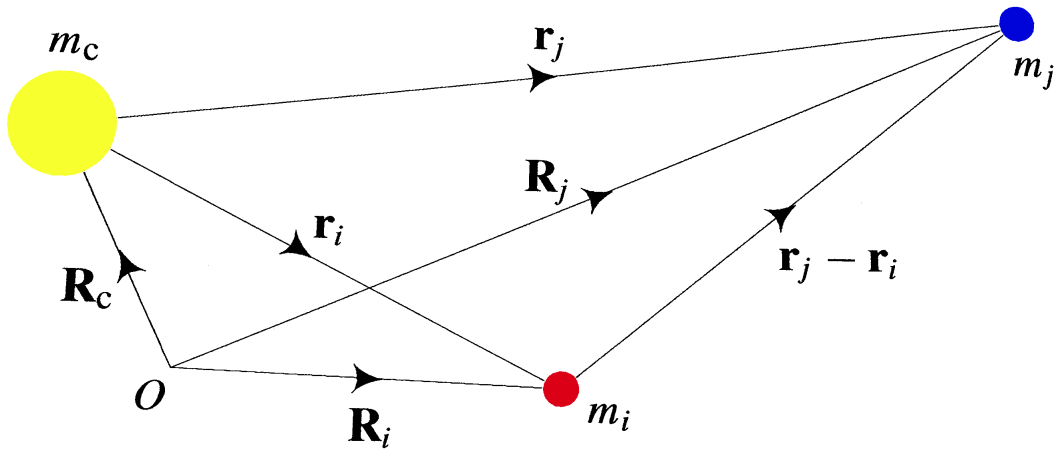

Figure 2.6. The position vectors $\mathbf{r}_i$ and $\mathbf{r}_j$, of two masses m_i and m_j with respect to the central mass m_c. The three masses have position vectors $\mathbf{R}$, $\mathbf{R}'$, and $\mathbf{R}_c$ with respect to an arbitrary, fixed origin O. This figure was adapted from Murray & Dermott (1999).

Comparing Figure 2.1a to 2.6, it can easily be shown that the arbitrary, fixed origin O could be chosen as the barycenter which would make the figures equivalent. Using this equivalence, the disturbing functions R_i and R_j can be shown to be

$$R_i = Gm_j \left(\frac{1}{|\mathbf{r}_j - \mathbf{r}_i|} - \frac{\mathbf{r}_i \cdot \mathbf{r}_j}{r_j^3} \right),$$

and

$$R_j = Gm_i \left(\frac{1}{|\mathbf{r}_j - \mathbf{r}_i|} - \frac{\mathbf{r}_i \cdot \mathbf{r}_j}{r_i^3} \right). \tag{2.45}$$

Equation 2.45 clearly shows each disturbing function to be a first order expansion of the corresponding gravitational potential. Thus the standard practice of an

expansion of $|\mathbf{r}_j - \mathbf{r}_i|$ into Legendre polynomials can be performed using the angle ψ that is made with respect to $\mathbf{r}_j$ and $\mathbf{r}_i$ to give

$$\frac{1}{|\mathbf{r}_j - \mathbf{r}_i|} = \frac{1}{r_j}\sum_{l=0}^{\infty}\left(\frac{r_i}{r_j}\right)^l P_l\left(\cos\psi\right). \tag{2.46}$$

Equation 2.46 assumes that $r_i < r_j$ and if this condition were to fail, then the resulting situation would describe a system where the indices i and j are interchanged. Following this point it becomes more useful to express the disturbing function in terms of orbital elements rather than Cartesian coordinates, which gives

$$R_i = Gm_j \sum S(a_i, a_j, e_i, e_j, I_i, I_j)\cos\varphi. \tag{2.47}$$

The expression for R_j would have the same form with a change in the respective indices. Finding the angle φ is at the center of the analysis of resonances, so a procedure to determine this angle is now presented.

The angle φ is also called the resonant angle. This is because a relationship between the mean longitudes (λ), longitudes of pericenter (ϖ), and right ascensions of the ascending node (Ω) can be made using integers k, l, and m. The resonant angle is defined as

$$\varphi = k_j\lambda_j + k_i\lambda_i + l_j\varpi_j + l_i\varpi_i + m_j\Omega_j + m_i\Omega_i \tag{2.48}$$

where $k_j + k_i + l_j + l_i + m_j + m_i = 0$ due to the azimuthal invariance of the central mass' potential.

In practice determining the integers k, l, and m can become difficult using only analytical means. As a result a number of methods exist for determining k, l, and m through the determination of orbital resonances. Orbital resonances are defined to

be rational expressions of the frequencies/periods of the smaller masses, m_j and m_i. For example, a 2:1 mean motion resonance (MMR) would describe a case where m_i would orbit m_c two times for every orbit of m_j around m_c and the term mean motion denotes that the resonance is a simple integer ratio (See Figure **??**).

Hadjidemetriou (1993) used the method of averaging as well as the method of computing periodic orbits numerically. He showed how to utilize these methods to determine MMRs; furthermore, he discussed the advantages and disadvantages of each method as well as the effects of their inherent limitations on the attained results. Another method of finding MMRs is based on the concept of Lyapunov exponent as introduced by Nesvorný & Morbidelli (1998) with its further development by Morbidelli & Nesvorny (1999) and Nesvorný et al. (2002).

This dissertation uses a modified version of the method presented by Nesvorný et al. (2002). This modified method adopts the maximum Lyapunov exponent as an indicator to provide information about the position of MMRs with respect to distance from m_c. Furthermore, it uses numerical tools such as FFT to determine the orbital periods of the masses orbiting m_c. Once the type of resonance is identified, it can then be classified as a resonance that leads to periodic, quasi-periodic, or non-periodic behavior.

CHAPTER 3

APPLICATION OF CHAOS INDICATORS

I now consider two individual planets in two known binary star systems γ Cephei and HD 196885, and compute their orbits by using various numerical techniques to assess their chaotic or quasi-periodic nature. The Hill stability (HS) function, which measures the orbital perturbation of a planet around the primary star due to the secondary star, is also calculated for each system. The maximum Lyapunov exponent (MLE) time series are generated to measure the divergence/convergence rate of stable manifolds, which are used to differentiate between chaotic and non-chaotic orbits. Then, I calculate the dynamical Mean Exponential Growth factor of Nearby Orbits (MEGNO) maps by solving the variational equations together with the equations of motion. These maps allow us to accurately differentiate between stable and unstable dynamical systems. The results obtained from the analysis of HS, MLE, and MEGNO maps are analyzed for their dynamical variations and resemblance. The HS test for the planets shows stability and quasi-periodicity for at least ten million years. The MLE and the MEGNO maps also indicate the local quasi-periodicity and global stability in a relatively short integration period. The orbital stability of the systems is tested using each indicator for various values of planet inclinations ($i_{pl} \leq 25^{\circ}$) and binary eccentricities. The reliability of the HS criterion is also discussed based on its stability results compared with the MLE and MEGNO maps.

3.1 Background

A number of discovered extra solar planets has been growing substantially since the first planet, 51 Pegasi b, was detected almost two decades ago (Mayor & Queloz 1995). Since then 1822 extra solar planets have been confirmed as of September 22, 2014[1]. Near half of solar type stars (Duquennoy & Mayor 1991; Raghavan et al. 2006) and a third of all stars in the Galaxy (Raghavan et al. 2010) are in a binary or multi-star system with 40 planets confirmed in such systems (Desidera & Barbieri 2007). The confirmation of the existence of planets in binaries has raised a new astrophysical challenge which includes the study of long term orbital stability of such planets. The ultimate destiny of exoplanet research, including observations from the Kepler mission[2], is to detect a planet on a stable orbit within the habitable zone of the host star (Borucki et al. 1997; Koch et al. 2006; Borucki et al. 2008, 2010). The degree of stability is largely governed by the planet's semimajor axis, eccentricity and orbital inclination. Orbital long-term stability is believed to be a necessary condition for life to develop. The study of orbital stability furthers one self-evident aim of mankind which is to find an answer to the century old question, "Are we alone in the Milky Way Galaxy?".

By using different stability criteria the question of stability has been addressed by many others in the past. While studying the Trojan type orbits around Neptune, Zhou et al. (2009) showed that the inclination of orbits can be as high as 60° while maintaining orbital stability. Several authors (Szebehely 1980; Szebehely & McKenzie 1981; Szenkovits & Makó 2008) calculated orbital stability of planets by using several techniques that include the integrals of motion, zero velocity surfaces (ZVS), and a Hill stable region that is mapped by a parameter space of orbital radius and mass ratio,

[1] www.exoplanet.eu

[2] www.nasa.gov/mission_pages/kepler/overview/index.html

Table 3.1. Orbital parameters of γ Cephei (Neuhauser et. al. 2007)

γ **Cephei**	**A**	**B**	**Ab**
Mass	1.4 $M_\odot$	0.362 $M_\odot$	1.6 M_J
Semimajor Axis (a)	19.02 AU		1.94 AU
Eccentricity (e)	0.4085		0.115
Argument of Periapsis (ω_p)	0°	180°	94°

μ, for a coplanar CRTBP. Quarles et al. (2011) also used the maximum Lyapunov exponent (MLE) to determine the orbital stability or instability for the CRTBP case. The stability limits were defined based on the values of MLE that are dependent on the mass ratio μ of the binaries and the initial distance ratio ρ_0 of the planet. Other chaos indicator techniques such as Mean Exponential Growth factor of Nearby Orbits (MEGNO) maps have also been used to study the dynamical stability of irregular satellites (Hinse et al. 2010) and extrasolar planet dynamics (Goździewski & Maciejewski 2001; Goździewski et al. 2001). The MEGNO criterion is known to be efficient in distinguishing between chaotic and quasi-periodic initial conditions within a dynamical phase space.

Knowing the orbital stability of planets is a crucial step for further studies of planetary systems. In order to probe a planet for its habitability, there exists a primary requirement that the system be orbitally stable. In this project, I used three stability indicators, the HS, MLE, and MEGNO maps, in my study of the orbital dynamics of planets in the selected stellar binaries. I also compared all the results from the three different methods in order to determine if the HS can be considered a reliable, efficient tool in the stability analysis of exoplanets.

Table 3.2. Orbital parameters of HD 196885, (Chauvin et al. 2007)

HD 196885	**A**	**B**	**Ab**
Mass	1.33 $M_\odot$	0.45 $M_\odot$	2.98 M_J
Semimajor Axis (a)	21 AU		2.6 AU
Eccentricity (e)	0.42		0.48
Argument of Periapsis (ω_p)	0°	180°	93.2°

3.2 Basic Definitions Equations

For the motion of a planet of mass m_1 around a star of mass m_2 in an orbital plane, the initial velocity was calculated using the time derivative of the position matrix given by Murray & Dermott (1999). While calculating the initial conditions I used the values of the parameters (a, e, i Ω, ω and f) whenever they have been observationally determined.

Our particular interest is in the stellar binaries that are less than or equal to 25 AU apart. For the stars with greater than 25 AU separations, the effects of the secondary star on the planet would not be significant, especially while considering the intent of our present study.

The list of planets in the binaries and their orbital parameters are given in Tables 3.1 and 3.2. The initial setup in our simulations is in a barycentric coordinate system with the appropriate placement of Star B (left) and Star A (right) relative to the barycentre. The positive x-axis is taken to be the reference. The true anomaly of both the binary and planet are assumed to be equal to zero.

For two primaries in elliptic orbits moving about their barycentre the dynamical system of a third smaller mass can be written as the first order differential equations. The equations of motion are given below (Szebehely 1967; Szenkovits & Makó 2008). In order to conform to the prescribed notation a simple variable substitution is used

$(\xi, \eta, \zeta, \dot{\xi}, \dot{\eta}, \dot{\zeta})^* = (x, y, z, u, v, w)^*$, respectively.

$$
\begin{aligned}
x' &= u & u' &= 2v + \frac{1}{(1+e\cos f)}\left[x - \frac{\alpha(x+\mu)}{r_1^3} - \frac{\mu(x-1+\mu)}{r_2^3}\right], \\
y' &= v & v' &= -2u + \frac{y}{(1+e\cos f)}\left[1 - \frac{\alpha}{r_1^3} - \frac{\mu}{r_2^3}\right], \\
z' &= w & w' &= -z + \frac{z}{(1+e\cos f)}\left[1 - \frac{\alpha}{r_1^3} - \frac{\mu}{r_2^3}\right],
\end{aligned} \tag{3.1}
$$

where

$$
\begin{aligned}
\mu &= \frac{m_2}{(m_1+m_2)}, \\
\alpha &= 1-\mu, \\
r_1^2 &= (x-\mu)^2 + y^2 + z^2, \\
r_2^2 &= (x+\alpha)^2 + y^2 + z^2.
\end{aligned} \tag{3.2}
$$

The Jacobi constant (C_0) for a initial state (x_o, y_o, z_o, f_o) is given by

$$
C_0 = \frac{x_0^2 + y_0^2 + \frac{2(1-\mu)}{r_1} + \frac{2\mu}{r_2}}{1+e\cos(f_0)} - \dot{x}_0^2 - \dot{y}_0^2 - \dot{z}_0^2. \tag{3.3}
$$

In Equation 3.1, the variables represent the velocity of a test particle (planet) in Cartesian coordinates (x, y, z). The distances r_1 and r_2 are defined in terms of mass ratio, normalised coordinates, and the position of the stars within a pulsating-rotating coordinate system. Although the masses were integrated using a N-Body representation, I have included the ERTBP equations of motion to illustrate the

necessary transformations to arrive at the pulsating-rotating coordinate system (see Szebehely (1967) for full details) used in Sect. 3.6.

The variables in the above equations describe the position of the planet, which in essence constitutes a test particle, within a synodic coordinate system. Its position is defined in Cartesian coordinates $\{x,\ y,\ z\}$. I denote the time derivative or velocity of a coordinate using the dot notation $\left\{\dot{x} = \frac{\mathrm{dx}}{\mathrm{dt}}\right\}$. I also represent the set of second order differential equations, the equations of motion, by a set of first order differential equations (see Section 2.8). The velocity is defined by the coordinates $\{u,\ v,\ w\}$ whose time derivatives are the accelerations. By defining the mass ratio and using normalized coordinates, I can then define the distances $\{r_1,\ r_2\}$ with reference to the location of the stars in the rotating coordinate system. This particular convention assumes that $GM = 1$ such that the above equations can be described in the same manner as Equations 2.11, 2.12, and 2.13.

I enumerate the co-linear Lagrange points (positions of zero potential) in the synodic frame by the order of which the ZVC opens. The point between the stars opens first; therefore, I denote it as L1. The point to the left of the star that does not host the planet opens second; thus, I denote it L2. The point to the right of the star hosting the planet opens third and it is denoted L3. The two Trojan Lagrange points which are of lesser importance to our study are L4 and L5.

3.3 Lyapunov Exponents

For stable planetary orbits, the two nearby trajectories in phase space converge, and for unstable orbits the trajectories diverge exponentially. The rate of divergence is measured by using the method of Lyapunov exponents (Lyapunov 1907). Wolf et al. (1985) developed a numerical method of computing the Lyapunov exponents in FORTRAN following the earlier works by Benettin et al. (1980).

Lyapunov exponents are commonly used because they give the measure of an attractor of a dynamical system as it converges or diverges in phase space. The positive Lyapunov exponents measure the rate of divergence of neighbouring orbits, whereas negative exponents measure the convergence rates between stable manifolds (Tsonis 1992; Ott 1993). The sum of all Lyapunov exponents is less than zero for dissipative systems (Musielak & Musielak 2009) and zero for non-dissipative (Hamiltonian) systems (Hilborn & Sprott 1994). Lyapunov exponents for the circular restricted three body problems (CRTBP) have been calculated previously (Gonczi & Froeschle 1981; Murray & Holman 2001) and similar methods have been used in the ERTBP. In this work, I calculated the Lyapunov exponents for the N-body problem where $N = 3$. In order to compute the Lyapunov exponents a dynamical system with n degrees of freedom is represented in a $2n$ phase space. Then the state vectors ($2n$) containing 6 elements are used to calculate the Lyapunov exponents. The details on the calculation of Jacobian J from the equations of motion can be found in Quarles et al. (2011).

For a Hamiltonian system (see above) to be stable, the sum of all the Lyapunov exponents should be zero. In order to numerically meet such a criterion, a simulation of the system would require an impractically long period of time. Within the limits of simulation, the sum of all six exponents must remain numerically close to zero ($\sim 10^{-10}$). I used the largest positive Lyapunov exponent to determine the magnitude of the chaos while ignoring the lesser positive and the negative exponents as they do not provide significant additional information about the evolving system. The positive maximum Lyapunov exponent is known to indicate a chaotic behavior in both dissipative (Hilborn & Sprott 1994) and non-dissipative (Ozorio de Almeida 1990) systems. Chaos can be proven up to the integration time if a given chaos indicator has converged to an unstable manifold.

3.4 Hill Stability

Hill (1878a,b) developed the equations of motion for a particle around the primary mass in presence of a nearby secondary mass. The purpose of the Hill equations was to calculate the orbital perturbation of the particle due to the secondary mass. Later the idea was further developed and used in the study of orbital stability of planets (Szebehely 1967; Walker & Roy 1981; Marchal & Bozis 1982).

The significant radial gravitational influence of the secondary mass reaches as far as the Lagrange points, L1 and L2, forming the Hill sphere (Hill 1878a,b). The contour lines within the sphere are the zero velocity curves. After measuring a particle's position and velocity, a constant of motion relation can be implemented (Szebehely 1967; Murray & Dermott 1999) $2U$ - $v^2 = C_J$, where v is the velocity, U is the generalized potential, and C_J is the constant of integration called the Jacobi constant. When the velocity of the particle is zero, $2U = C_J$, a contour represents a zero velocity surface (ZVS) and the motion of a particle within such a surface is considered Hill stable.

The measure of Hill stability for the ERTBP, $S(f)$, is given by a parameter dependent potential, $\Omega(\boldsymbol{X}, f)$, where f is the true anomaly and C_{cr} is the value of the Jacobi constant at the Hill radius or the Lagrange point L1 (Szenkovits & Makó 2008)

$$\begin{aligned}\Omega(x, y, z, f) &= \frac{1}{2}\left[x^2 + y^2 - ez^2\cos(f)\right] + \frac{1-\mu}{r_1^2} + \frac{\mu}{r_2^2} \\ &\quad + \frac{1}{2}\mu(1-\mu), \\ S(f) &= \frac{1}{C_{cr}}\left[2\Omega(\boldsymbol{X}, f) - \left[1 + e\cos(f)\right]v^2\right] - 1. \end{aligned} \tag{3.4}$$

Using the orbital parameters obtained from the numerical integration, the potential $\Omega(\boldsymbol{X}, f)$, is calculated to obtain the Hill stability function $S(f)$. Although the Hill stability function depends on the true anomaly, it can also be represented as a time series. I have implemented this representation in our results concerning the Hill stability function. When the measure of $S(f)$ of a planet is positive then we have the indication of quasi-periodic orbits and its motion is Hill stable. But when the measure of $S(f)$ is negative then the planet enters the instability region.

3.5 The MEGNO Chaos Indicator

The MEGNO criterion was first introduced by Cincotta & Simó (1999, 2000) and Cincotta et al. (2003),who found wide-spread applications in dynamical astronomy (Goździewski et al. 2001, 2008; Goździewski & Migaszewski 2009; Hinse et al. 2008, 2010; Frouard et al. 2011; Compère et al. 2012; **?**). The MEGNO (usually denoted as $\langle Y \rangle$) formalism has the following mathematical properties. In general, MEGNO has the parametrization $\langle Y \rangle = \alpha \times t + \beta$ (see references above). For a quasi-periodic initial condition, it has $\alpha \simeq 0.0$ and $\beta \simeq 2.0$ (or $\langle Y \rangle \to 2.0$) for $t \to \infty$ asymptotically. If the orbit is chaotic, then $\langle Y \rangle \to \lambda t/2$ for $t \to \infty$. Here λ is the maximum Lyapunov exponent (MLE) of the orbit. In practice, when generating the MEGNO maps, I terminate a given numerical integration of a chaotic orbit when $\langle Y \rangle > 12.0$. Quasi-periodic orbits have $|\langle Y \rangle - 2.0| \leq 0.001$.

The MECHANIC[3] software (Słonina et al. 2012) is used which is optimized to N-body code to calculate the orbits of the given masses and the MEGNO maps on a multi-CPU computing environment. Typically 60 CPUs are allocated for the calculation of one map considering a typical grid of (500×300) initial conditions in (a, e) space. The numerical integration of the equations of motion and the associated

[3]http://www.git.astri.umk.pl/projects/mechanic

variational equations (Mikkola & Innanen 1999) are based on the ODEX integration software (Hairer et al. 1993) which implements a Gragg-Bulirsch-Stoer algorithm. The MEGNO indicator is calculated from solving two additional differential equations as outlined in Goździewski et al. (2001). For reason of completeness I have outline some details of the MEGNO formalism. Following Cincotta & Simó (2000) MEGNO (Y) is defined as

$$Y(t) = \frac{2}{t} \int_{t_0}^{t} \frac{\parallel \dot{\boldsymbol{\delta}}(s) \parallel}{\parallel \boldsymbol{\delta}(s) \parallel} \; s \; ds, \tag{3.5}$$

along with its time-averaged mean value

$$\langle Y \rangle(t) = \frac{1}{t} \int_{t_0}^{t} Y(s) \; ds. \tag{3.6}$$

The quantity $\boldsymbol{\delta}$ is the variational state vector and t is time. The absolute norm of $\boldsymbol{\delta}$ measures the distance between two nearby points in phase space using an Euclidean metric. The variational vector is found from solving the variational equations of motion in parallel to the Newtonian equations of motion (Mikkola & Innanen 1999; Goździewski et al. 2001; Hinse et al. 2010). Equations 3.5 and 3.6 can be rewritten (Goździewski et al. 2001) as the two first-order differential equations

$$\frac{dx}{dt} = \frac{\dot{\boldsymbol{\delta}} \cdot \boldsymbol{\delta}}{\parallel \boldsymbol{\delta} \parallel^2} \; t \qquad \text{and} \qquad \frac{dw}{dt} = 2 \; \frac{x}{t}, \tag{3.7}$$

which are solved in tandem alongside the equations of motion and variational equations of motion. At the end of each integration step the quantities $Y(t)$ and $\langle Y \rangle(t)$ can be determined from $Y(t) = 2x(t)/t$ and $\langle Y \rangle(t) = w(t)/t$. When generating MEGNO maps we chose to plot the mean value $\langle Y \rangle$.

MEGNO and the maximum Lyapunov exponent (MLE) have a close relation as these two indicators provide the magnitude of the exponential divergence of orbits. Froeschlé et al. (1997) introduced the fast Lyapunov indicator (FLI), which exhibits the least dependency on initial conditions. Mestre et al. (2011) showed that MEGNO and FLI are related to each other. FLI is used to detect weak chaos and is considered a faster means to determine the same characteristics as MLE. Recently, Maffione et al. (2011) compared various chaos indicators including FLI and MEGNO. The MEGNO technique and FLI are considered to be in the same class of chaos detection tools (Morbidelli 2002), and we have chosen the MEGNO technique to compare against the Hill stability criterion. More on mathematical properties of MEGNO and its relationship with the Lyapunov exponents can be found in Hinse et al. (2010).

In this dissertation, each map is generated with 1.5×10^5 initial conditions, for a resolution of 300×500 in various orbital elements and simulated up to 400 Kyr. The purple/blue color in the map denotes the quasi periodic region and the yellow is the region of chaos. The MEGNO quantity $\langle Y \rangle$ is color-coded in the color bar.

3.6 Results and Discussion

3.6.1 Numerical Simulation

To establish the Hill stability (HS) criterion and calculate the maximum Lyapunov exponents (MLE), I numerically simulated each of the planets in the stellar binaries using a Yoshida sixth order symplectic and a Gragg-Bulirsch-Stoer integration scheme (Yoshida 1990; Grazier et al. 1996; Hairer et al. 1993). A step of ϵ=10^{-3} years/step was used in each case to have a better measure of the precision of the integration scheme. The error in energy was calculated at each step, which falls in the range of 10^{-14} to 10^{-10}, during the total integration period. Numerical simulations

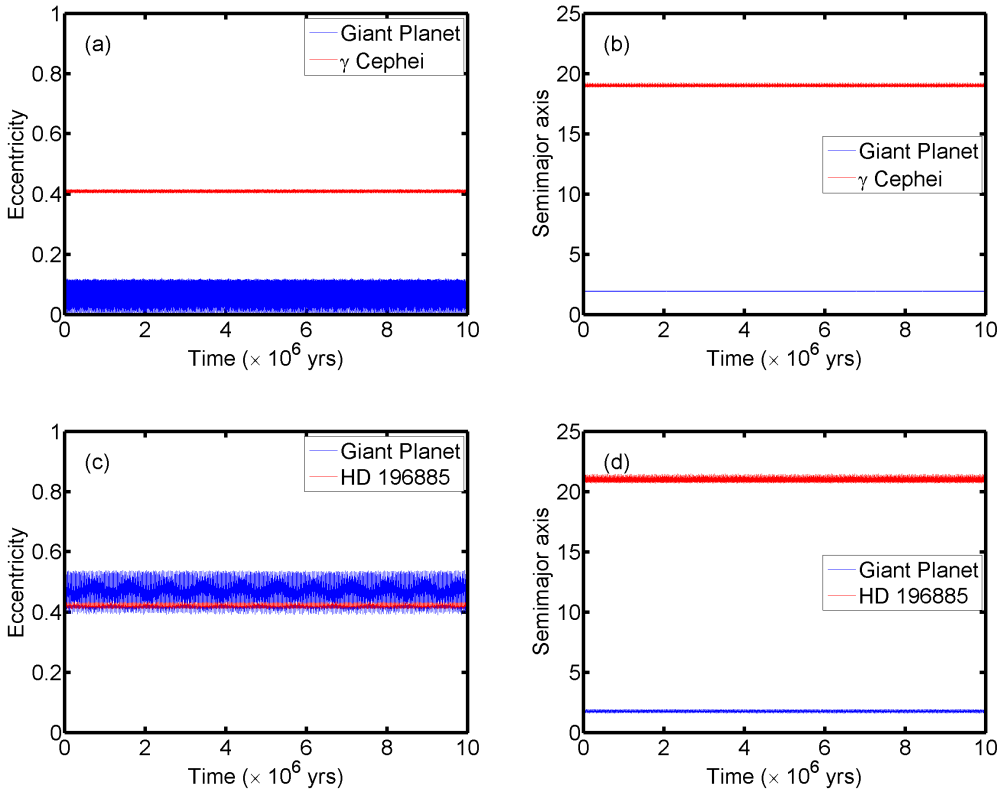

Figure 3.1. Variations in the orbital elements (semi-major axis and eccentricity) for the giant planets in γ Cephei and HD 196885 ($i_{pl} = 0.0$) simulated for 1×10^7 years (Satyal et al. 2013).

were completed for a million years to calculate the MLE and 10 million years to calculate the HS. MEGNO maps are calculated using 100,000 years per initial condition. Chaos, quasi-periodicity, or regular motion can be shown up to the integration time; however, the long term evolution of these systems can only be proven for chaos where the other types of motion are inferred due to the moderate presence or lack of chaos.

The purpose of simulating for 10 million years was to display the evolution of eccentricity and semimajor axis without applying any indicator tools to provide a consistent comparison in order to analyze the orbital behavior and to establish the full effectiveness of the indicators. The time series plots for the systems, γ Cephei and HD

196885, are relatively constant with minor oscillations for 10 million years (Fig. 3.1). In these cases I found that the eccentricity of the giant planets is oscillating with a constant amplitude. For example, Figs. 3.1a and 3.1c demonstrate oscillations from 0 to 0.1 and 0.4 to 0.5 in values of eccentricity for γ Cephei and HD 196885, respectively. The amplitude of the oscillation changed with a different choice of initial conditions. As a result, specific choices can minimize the oscillation amplitude and can render the simulation for γ Cephei to be in a closer agreement with previous studies by Haghighipour (2006). One such initial condition involves the choice of eccentricity. If $e = 0$ for the planetary orbit initially, I observed that the amplitude of oscillation is minimum and consistent with Haghighipour (2006) while the amplitude increases with larger initial e values.

3.6.2 MLE: Indicator Analysis

The maximum Lyapunov exponent (MLE) time series for the simulated planets in the stellar binaries are given in Figs. 3.2 and 3.3. The MLE is plotted using a logarithmic scale along the y-axis and a linear scale along the time-axis. I obtained six Lyapunov exponents from our simulation among which three are negative and three are positive. I inspected the first three positive LEs and found the magnitude of the largest value which is used for our purpose of establishing the stability of a system. In Figure 3.2, I taken the maximum Lyapunov exponent as the primary indicator of the orbital stability. For a given initial condition, the MLE must quickly drop below a cut off value similar to Quarles et al. (2011) and decrease at a constant rate,so I can determine it as stable or unstable.

The MLE indicates stability for both of the considered systems in the coplanar case, as expected from the observations. This is demonstrated by the values of the MLE, which start on the order of 1 and slowly converge down by orders of 10 on a

logarithmic scale. The MLE for γ Cephei is calculated using three values of initial binary eccentricity: first at the nominal observational value (Fig. 3.2a), second within the semi-chaotic region (Fig. 3.2b) and third within a region of chaos (Fig. 3.2c). The e_{bin} values assumed for the semi-chaotic and chaotic regions were obtained from MEGNO maps (section 3.6.4). While varying the value of e_{bin}, the orbital inclination was kept constant at 0°. For the first case ($e_{bin} = 0.4085$), Fig. 3.2a shows the MLE slowly decreasing to -13 in a million years. The MLE also shows a similar trend for the second case ($e_{bin} = 0.6$). Hence, considering this decreasing trend and the nature of Lyapunov exponents (Sect. 2.2), the results reflect the outcome of orbital stability for the planet for our two choices of e_{bin}. For the third choice of $e_{bin} = 0.65$, the MLE time series began displaying instabilities within 2.25×10^5 years.

The MLE for γ Cephei Ab (Fig. 3.2d) is also calculated using three additional values of initial orbital inclination (i_{pl} = 7°, 15°, 25°). While varying the initial planetary inclination, e_{bin} was set to the nominal value. Irrespective of our considered initial values in inclination the MLEs of the planet remained unaffected where all cases demonstrate a decreasing trend to -13 in a million years, reflecting the criterion for orbital stability.

Similar to the case of γ Cephei, I calculated the MLE for the planet in HD 196885 for three values of binary eccentricity. For the nominal observational value of e_{bin} (Fig. 3.3a) and e_{bin} chosen to be at the semi-chaotic region (Fig. 3.3b), the MLEs clearly display stable orbits. But, as the e_{bin} was raised to 0.6 the MLE time series displayed an orbital instability within 1×10^3 years (Fig. 3.3c), as also shown by the MEGNO result (see Fig. 3.9c).

The MLE time series for HD 196885 Ab, Fig. 3.3 is distinct for all considered initial values of the planet's inclination, i_{pl}, and the orbit of the planet exists in a stable configuration. However, when using our four choices of i_{pl} values, the MLE

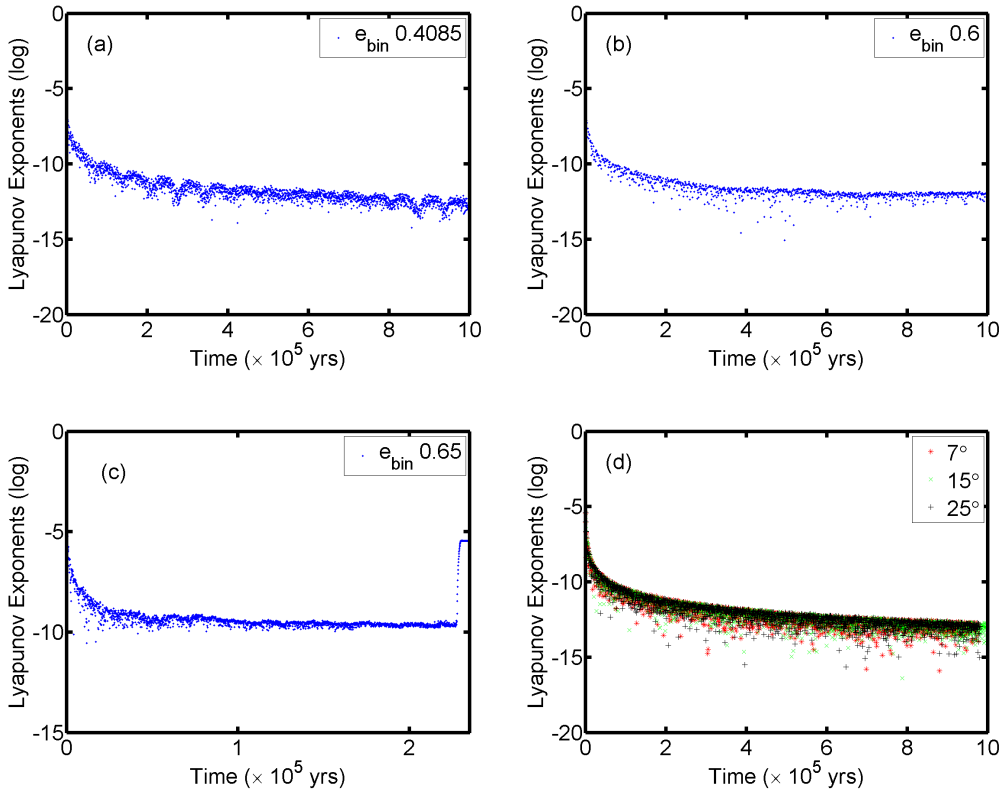

Figure 3.2. Lyapunov exponent time series for the giant planet in γ Cephei with respect to variations in e_{bin} and i_{pl}. The coplanar cases shown (a),(b) and (c) considered initial values of $e_{bin} = 0.4085$, 0.6, and 0.65, respectively. (d) illustrates the time series with the same e_{bin} as in (a) but with different initial values for $i_{pl} = 7°$, 15° and 25° as indicated by the legend. Note that the time axis of (c) has been truncated to the point of instability (Satyal et al. 2013).

time series demonstrates that the planetary orbits are more perturbed when they are positioned at 7° and 15°. The MLE values drop quickly to -7 and levels off indicating chaotic behavior but does not lead to instability. This may be due to the effects of a near resonance behavior. However, the stability criterion is not violated, thus this system could exhibit long term chaotic motions akin to Pluto in the Solar System. For $i_{pl} = 0°$ and 25° cases, the MLE values appear to be converging slower up to -10

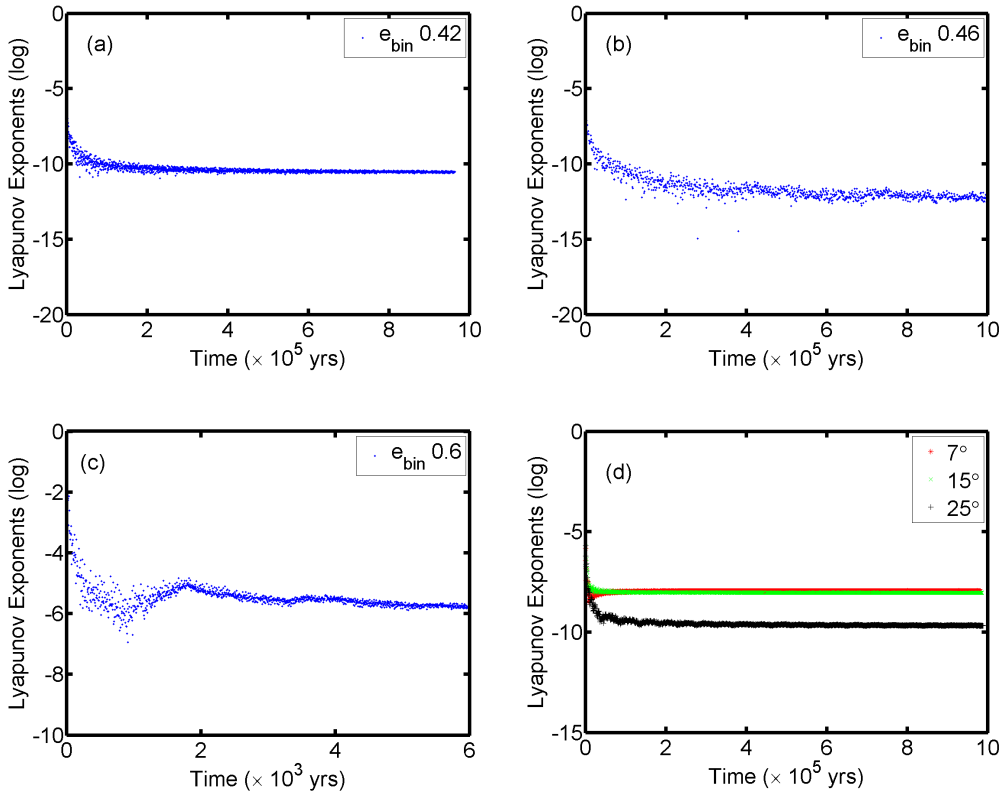

Figure 3.3. Lyapunov exponent time series for the giant planet in HD 196885 with respect to variations in e_{bin} and i_{pl}. The coplanar cases shown (a), (b) and (c) considered initial values of $e_{bin} = 0.42$, 0.46, and 0.6, respectively. (d) illustrates the time series with the same e_{bin} as in (a) but with different initial values for $i_{pl} = 7°$, 15° and 25° as indicated by the legend. Note that the time axis of (c) has been truncated to illustrate the nature of the instability (Satyal et al. 2013).

for the first few thousand years than the other considered cases and indicate stable orbits.

3.6.3 Establishing the Hill Stability criterion

The Hill stability time series for the planets in γ Cephei and HD 196885 are shown in Figs. 3.4-3.7. Starting with the coplanar case and the nominal value of binary eccentricity, I studied the cases when $i_{pl} = 7°$, 15° and 25°. I also calculated

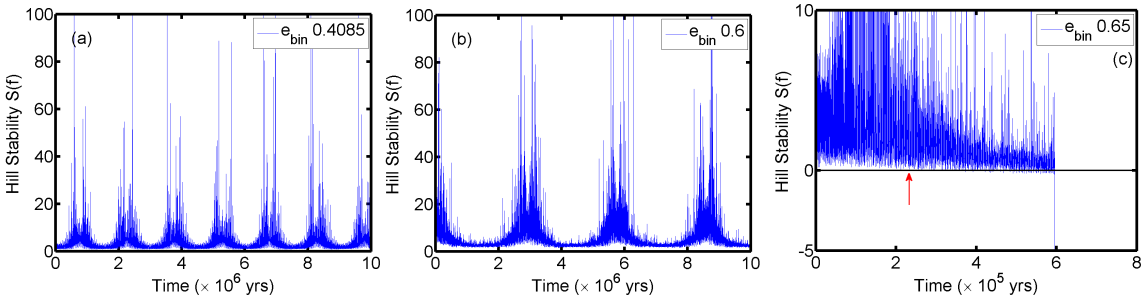

Figure 3.4. The Hill Stability function for the giant planet in γ Cephei for different cases of binary eccentricity (for $i_{pl} = 0°$) simulated for 1×10^7 years (see Figs. 3.2(a), (b) and (c)). Note that the time axis of (c) has been truncated to illustrate the nature of the instability (shown by the vertical arrow) and the point of ejection (Satyal et al. 2013).

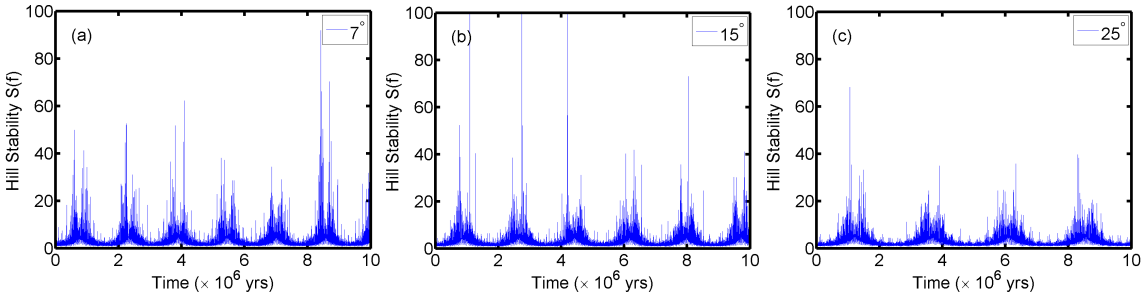

Figure 3.5. The Hill Stability function for the giant planet in γ Cephei for different cases of initial planetary inclination (for $e_{bin} = 0.4085$) simulated for 1×10^7 years (see LE time series Fig. 3.2(d)) (Satyal et al. 2013).

the HS functions for two other choices of e_{bin}. The choices of our e_{bin} and i_{pl} values are similar to the ones that I used to calculate the MLE time series and MEGNO maps for both of the binary systems.

The measure of Hill stability for γ Cephei Ab stays positive for $e_{bin} = 0.4085$ and $e_{bin} = 0.6$ throughout the integration period (10 million years) (Figs. 3.4a,b). The oscillations on average are small and positive, which reflects the condition for HS criterion established by Szenkovits & Makó (2008). In their calculations, the Hill stability is positive and constantly increases in time for million years, which is

consistent with our result. However, the plots are limited to million years in the calculations of Szenkovits & Makó (2008), and this makes the periodicity for long term oscillations of the planets to be unclear. For the nominal case, 7 spikes in the Hill stability are noted, which indicates that the planet shows a quasi-periodic motion every 1.4 million years. When e_{bin} is increased to 0.6, the period of the HS function decreases and occurs every 2.5 million years. This periodicity is caused by the gravitational perturbation on the planet due to the secondary star near the pericenter of the binary. As the e_{bin} is increased, the effects of secondary star on the planet is minimized because the time of interaction has been significantly reduced due to Kepler's 2nd Law, thus also reducing the period of HS function.

The HS criterion showed that the orbital stability of the planet decreases as I increase the e_{bin} of γ Cephei. When the e_{bin} was set to 0.65, the planet starts to display orbital instability at $\sim 2.25 \times 10^5$ years, a point where the HS function starts a negative trend in the time series (a cut off point shown by a vertical arrow, see Fig. 3.4c). The planet was ejected from the system at $\sim 6 \times 10^5$ years. The results supplement our previous instability prediction made from MLE analysis.

I also found that the measure of the Hill stability for γ Cephei Ab is positive for all of our choices of i_{pl}. However, the periodicity decreases with the increase in i_{pl} values (Figs. 3.5a, 3.5b, and 3.5c). The increment in orbital inclination of the planet minimizes the effect due to the secondary star's close approach to the planet.

Similarly, the Hill stability time series stays positive for the planet in HD 196885 binary system for the cases when e_{bin} is set at 0.42 (observational value) and 0.46 (Figs. 3.6a,b). The planet displays a quasi periodic motion every 1.1 million years for our first choice of e_{bin}. But I found insignificant change in the periodicity for the second choice of e_{bin}. The periodicity was not affected because of the minute difference in e_{bin}, (0.04).

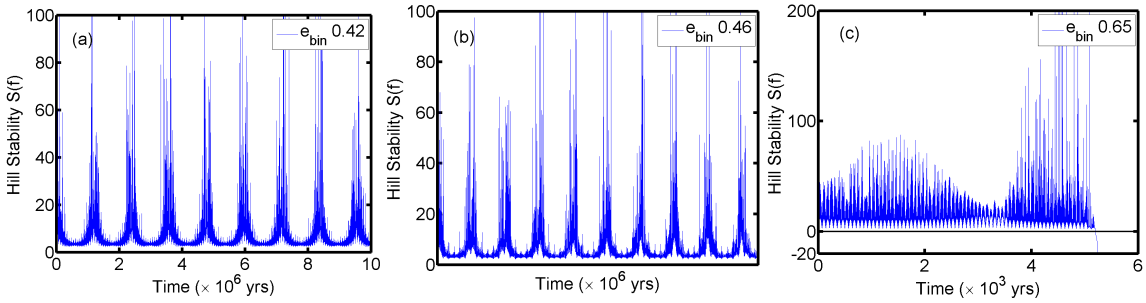

Figure 3.6. The Hill Stability function for the giant planet in HD 196885 for different cases of binary eccentricity (for $i_{pl} = 0°$) simulated for 1×10^7 years (see Figs. 3.2(a), (b) and (c)). Note that the time axis of (c) has been truncated to illustrate the nature of the instability and the point of ejection (Satyal et al. 2013).

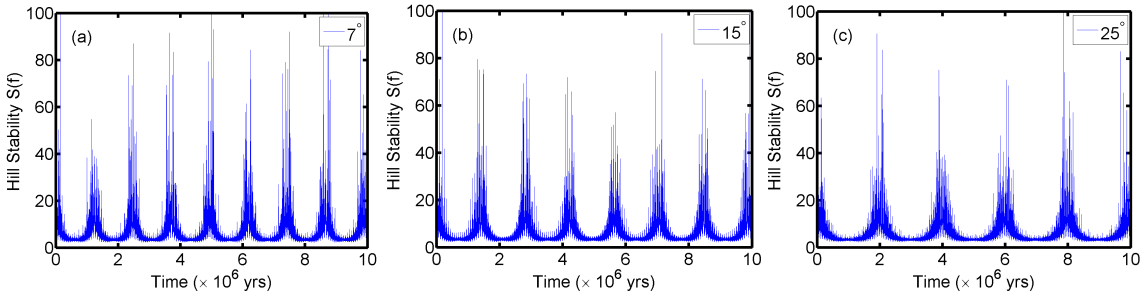

Figure 3.7. The Hill Stability function for the giant planet in HD 196885 for different cases of initial planetary inclination (for $e_{bin} = 0.42$) simulated for 1×10^7 years (see LE times series Fig. 3.3(d)) (Satyal et al. 2013).

When the e_{bin} of HD 196885 was set to 0.6 within the presumed unstable region, the HS time series demonstrates that the stability was lost within 5×10^3 years (Fig. 3.6c). For this system, the ejection of the planet also occurs at $\sim 5 \times 10^3$ years of simulation time. The ejection occurs in such a short period because the HS function was not efficient enough to predict the instability.

The stability of HD 196885 Ab was not affected by our choice of orbital inclination. The system demonstrates stable orbits for i_{pl} values as high as 25°. The HS time series remains positive reflecting the established stability criterion from Szenkovits & Makó. Just like the planet in γ Cephei, the period of HS function for HD 196885

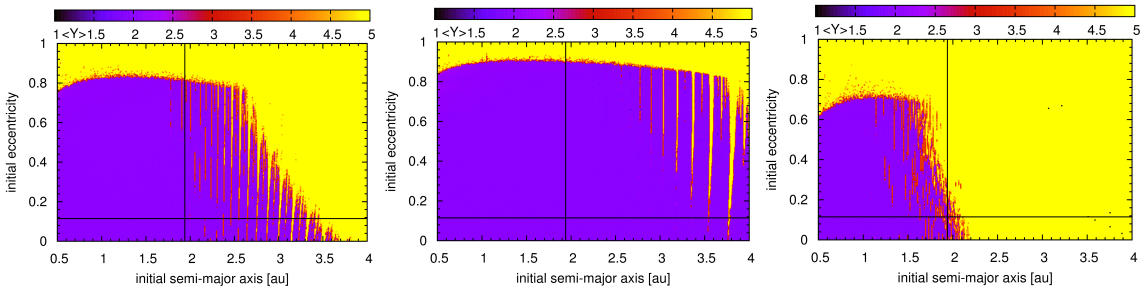

Figure 3.8. MEGNO Maps for the planet in γ Cephei at $i_{pl} = 0°$ and various binary eccentricities simulated for 1×10^5 years (left: $e_{bin} = 0.4085$, middle: $e_{bin} = 0.2$, right: $e_{bin} = 0.6$) (Satyal et al. 2013).

Ab decreases with the increase in i_{pl}. It would be interesting to exploit the nature of HS at higher i_{pl} values when the system hits the kozai resonances, but I limited my choice of i_{pl} at 25° in this dissertation.

3.6.4 Analysis of MEGNO maps

The dynamical maps of MEGNO are generated using a resolution of (500 x 300) producing 150,000 initial conditions in eccentricities and semimajor axes for the respective planets within the selected binaries. In Figs. 3.8 and 3.9 MEGNO maps for various binary eccentricities were simulated for 1×10^5 years. The cross hair in each subplot represents the osculating orbit of planet Ab for the respective binary (see Tables 3.1 and 3.2). The color bar on top of each map indicates the strength in the value of MEGNO($< Y >$). The blue color denotes regions of quasi-periodicity and the yellow indicates regions of chaos.

For different eccentricity values of the binary in γ Cephei, Fig. 3.8, the MEGNO indicator shows a clear distinction between quasi-periodic and chaotic regions. Within the observational value, $e_{bin} \sim 0.4085$ (Fig. 3.8a), the planet's motions are represented as stable orbits. When the binary eccentricity, $e_{bin} = 0.2$ (Fig. 3.8b), is decreased the

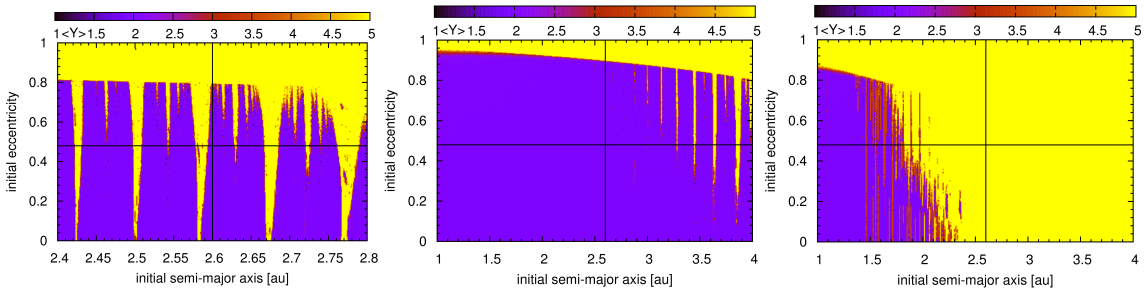

Figure 3.9. MEGNO Maps for the planet in HD 196885 ($i_{pl} = 0°$) and various binary eccentricities simulated for 1×10^5 years (left: $e_{bin} = 0.42$, middle: $e_{bin} = 0.2$, right: $e_{bin} = 0.6$) (Satyal et al. 2013).

cross hair is completely inside the quasi-periodic region, hence increasing the orbital stability. Conversely, as the eccentricity of the binary orbit is increased, e_{bin}=0.6, the location of the chaotic mean-motion resonances (yellow spikes at constant semimajor axis) are shifted to lower semimajor axes of the planet (Fig. 3.8c), hence decreasing the orbital stability. Studies done by Haghighipour (2006) for e_{bin} = 0.20-0.45 at interval of 0.05 and $i_{pl} = 0°$ also show that the planet in γ Cephei demonstrates stable orbits.

I also tested the stability of the planet in γ Cephei for the given values of orbital elements by generating a global map of e_{bin} vs. i_{pl}, where e_{bin} ranges from 0.0 to 1.0 and i_{pl} ranges from 0° to 25° (Fig. 3.10). The dynamics of the planet was found unchanged for the e_{bin} as high as 0.6 and any choice of $i_{pl} \leq 25°$. The system seems to show chaotic behavior at $e_{bin} = 0.6$ and low i_{pl} values but our earlier investigation (Fig. 3.8c) indicates the cross hair at the semi-chaotic region. I, then investigated a finer resolution window concerning this region and determined that the initial condition existed on the border of a chaotic region. Nonetheless, this confirms that for our choice of orbital inclination of the planet with the binary orbit, the planet is stable but may display chaos within the long-term (> 10 Myr). Moreover, our results are

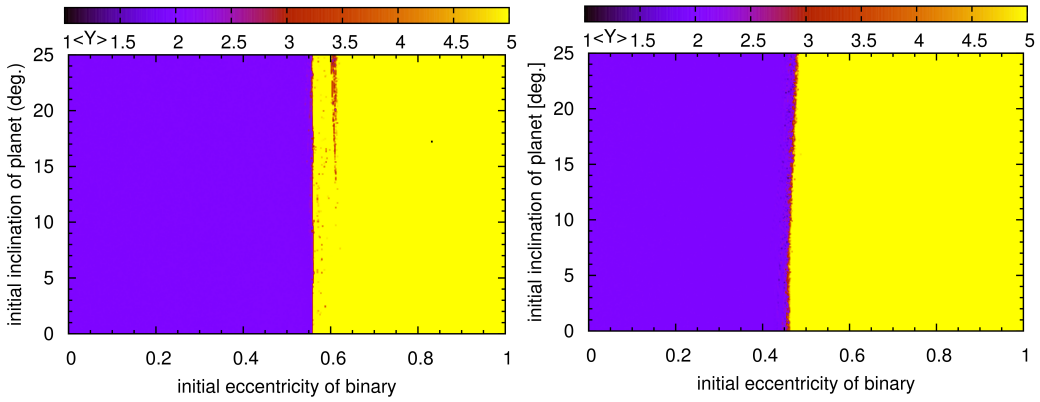

Figure 3.10. MEGNO Maps for the planet in (left) γ Cephei showing variation in the (e_{bin},i_{pl}) plane for the nominal (a_{pl},e_{pl}) values and (right) HD 196885 showing variation in the (e_{bin},i_{pl}) plane for its respective (a_{pl},e_{pl}) values simulated for 1×10^5 years (Satyal et al. 2013).

consistent with those obtained by Haghighipour (2006), who showed that the stable configuration of the system for all values of the planet's orbital inclination is less than 40°.

Figure 3.9a shows a locally stable region for the planet in HD 196885 system. The cross hair in the map is located right at the edge of the stable region. A small change in semimajor axis of the planet can divert the planet towards the chaotic region loosing global stability. Similarly the location of cross hair indicates that the quasi-periodicity increases with a decrease in the e_{bin}, Fig. 3.9b, while the system becomes chaotic with increment in e_{bin}, Fig. 3.9c.

Figure 3.10b, displays the case with the previously observed values of e_{bin} (Fig. 3.9) in a global map of e_{bin} vs. i_{pl} for the given values of orbital parameters of the system. It is found that the dynamics of HD 196885 Ab is unaffected by the choices of $e_{bin} \leq 0.46$ and $i_{pl} \leq 25°$. Giuppone et al. (2012) showed that the system is mostly stable when the planetary orbit is nearly coplanar or highly inclined orbits near the Lidov-Kozai equilibrium point, ($i_{pl} = 47°$). I did not test the system for i_{pl}>25°,

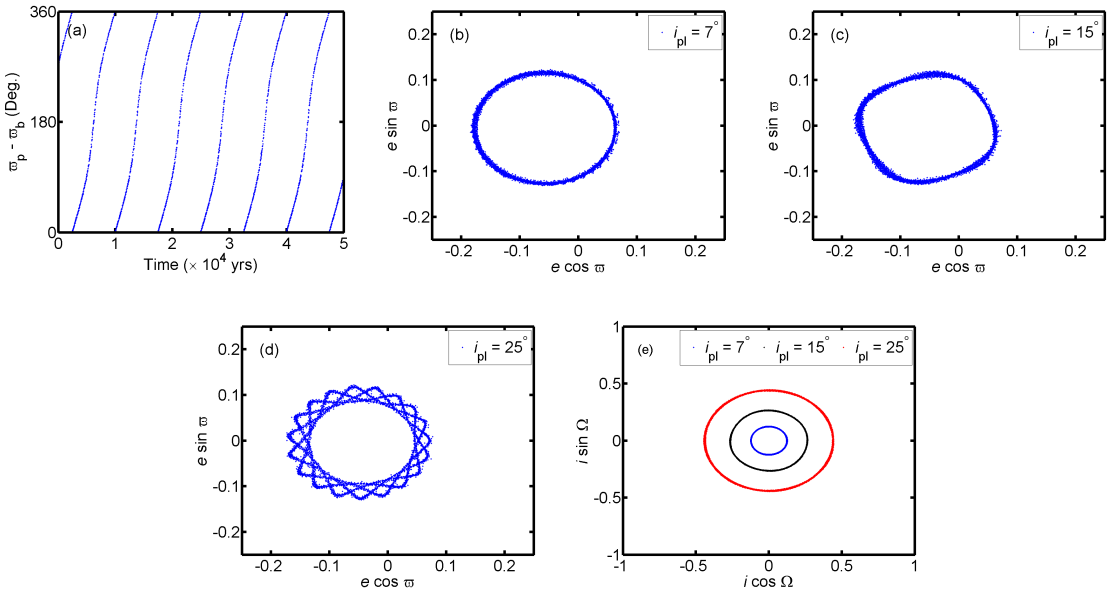

Figure 3.11. (a) Difference between the osculating longitude of pericentres (ϖ) for γ Cephei for 5×10^4 years. (b), (c), and (d) Evolution of osculating values ($e\cos\varpi$, $e\sin\varpi$) for different orbital inclinations. (e) Evolution of osculating values (i cos Ω, $i\sin\Omega$) for different orbital inclination (Satyal et al. 2013).

however, our result is consistent to the previous work with respect to MLE and HS time series of the respective inclination range.

3.6.5 Evolution of Osculating parameters

Considering the orbital parameters of γ Cephei and HD 196885 from the observations, the evolution of argument of periapsis (ω) and longitude of ascending node (Ω) are studied. In Figs. 3.11a and 3.12a, I presented the difference between longitude of periapsis between the planet and the binary (where $\varpi = \omega + \Omega$). The longitude of periapsis oscillates and is bound within 0° to 360° which exhibits an apocentric libration phenomenon (Murray & Dermott 1999).

Plots of the osculating values, $e\cos\varpi$ and $e\sin\varpi$, for the planet's nominal choice of parameters indicate no change in the osculating parameters of both systems.

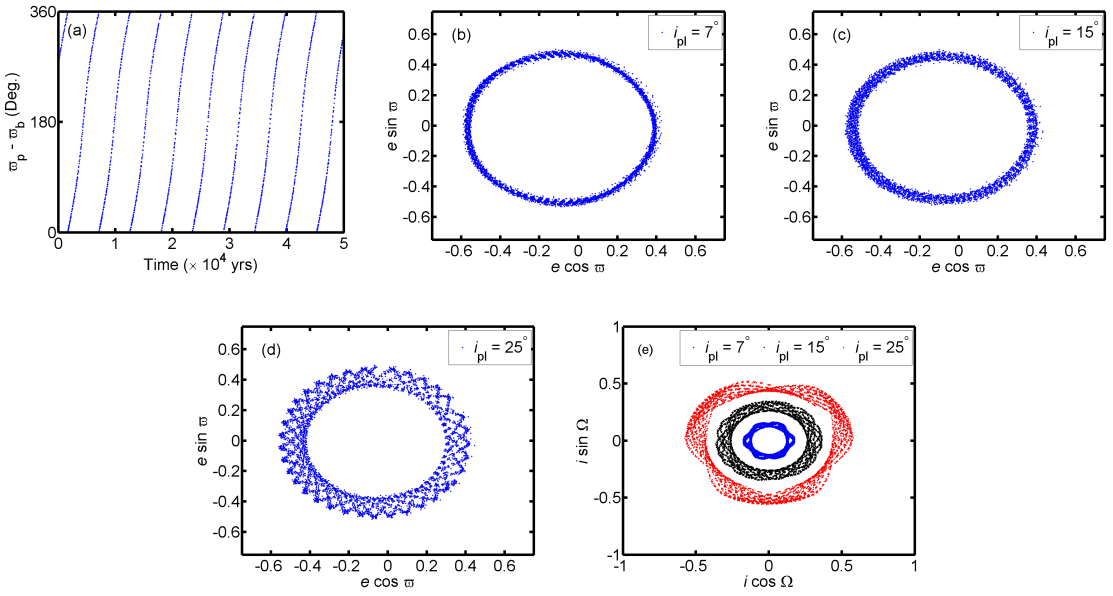

Figure 3.12. (a) Difference between the osculating longitude of pericenters (ϖ) for HD 196885 for 5×10^4 years. (b), (c), and (d) Evolution of osculating values ($e\cos\varpi$, $e\sin\varpi$) for different orbital inclinations. (e) Evolution of osculating values ($i\cos\Omega$, $i\sin\Omega$) for different orbital inclination (Satyal et al. 2013).

When the orbital inclination is increased (up to 25°), the precession rates are also noticeably increased (see Figs. 3.11b, c, d and 3.12b, c, d), an effect similar to period-doubling bifurcation (Ott 1993) leading to chaos. This change is not noticed directly in LE time series for γ Cephei (Fig. 3.2d) but I do observe variation (different converging rate) in the LE time series for HD 196885 (Fig. 3.3d) and variation (decreasing periodicity) in HS time series for both of the systems (Figs. 3.5 and 3.7).

Figures 3.11e and 3.12e display plots of the osculating parameters, $i\cos\Omega$ and $i\sin\Omega$, for different cases of orbital inclination. For the coplanar case, I would have a point-circle at the origin and the circle would grow larger for larger values of i_{pl}, as seen in these diagrams. The osculating parameters with respect to inclination indicates regular motion in the case of γ Cephei. But in the case of HD 196885 significant variations occur with increases in inclination (Fig. 3.12e).

3.6.6 Reliability of Hill stability function

Following the work done by Szenkovits & Makó (2008), I used the Hill stability criterion to study the orbital stability of planets in stellar binaries (γ Cephei and HD 196885). I also used the previously well known chaos indicators, MLE and the MEGNO maps to study the same systems. The maximum Lyapunov exponent (Figs. 3.2a and 3.3a) and the cross hair in the quasi periodic region of MEGNO map (Figs. 3.8a and 3.9a) demonstrate a stable configuration for given parameters in each of the considered systems. The positive value and non-decreasing global trend of Hill stability time series (Figs. 3.4a and 3.6a) also provides the necessary evidence of stable system. The HS time series indicates that the systems are quasi-periodic and the periodicity decreases as the planet's inclination and binary eccentricity is increased. Since the calculation for MLE is limited to one million years, I am unable to notice any periodicity in the time series as seen in the HS time series but it does also indicate trends toward stability. Similarly, MEGNO maps do not demonstrate any changes in stability when the respective planet's inclination increased up to 25°, nonetheless, it shows that the planets in both of the system exist within a stable configuration.

The stability of the planets is tested for highly eccentric binary orbits using MLE and MEGNO maps (Figs. 3.2c and 3.3c and 3.10). These figures clearly demonstrate unstable orbits for chosen e_{bin} values. Similar tests done by using HS time series (Figs. 3.4c and 3.6c) produce similar results regarding stability of the system.

The HS time series supplements two of our results from MLE and MEGNO for the cases when orbits are periodic and chaotic, thus establishing itself as a reliable stability criterion. For the planet in γ Cephei (see Figs. 3.2c and 3.4c), the HS function indicates an instability within the planetary orbit on an equal simulation timescale compared to MLE (see section 3.6.2). However, it took a slightly longer

simulation time to predict instability as compared to MLE for the case of HD 196885. For the system where the planet ejects in relatively short time ($\sim 5 \times 10^3$ years in this case) MLE is more efficient to predict regular or chaotic dynamical systems and the HS function seems to be an inefficient indicator (Figs. 3.3c and 3.6c).

There are limitations to the definition of HS as well. Most notably HS is defined for S-Type orbits only. Considering this limitation, it may be best suited in future work to the study of hypothetical or observed moons around gas giants as observed S-Type planet populations remain modest (Kipping et al. 2012). However, the populations of multi-planet single star systems are rapidly increasing with the use of Transit Timing Variations (see Lissauer et al. (2011, 2013) for recent results) and the HS criterion would provide adequate stability determinations for similar systems.

3.7 Summary

I applied various chaos indicator techniques in order to study the dynamics of S-type extrasolar planets in the binaries that are less than 25 AU apart. With the time series obtained from the maximum Lyapunov exponent, the Hill stability function, and the maps from the MEGNO indicator, I showed that both systems exist within a stable configuration for given parameters. Using these chaos indicators, I also tested the orbital stability of the system for various choices of binary eccentricity and planet's orbital inclination.

The calculated MLE and HS time series for the planets in both systems for different values of planet's orbital inclination, $i_{pl} = 0°$, $7°$, $15°$, $25°$, and given e_{bin} value display the orbital stability of the system. For the given values of orbital parameters it is found that the planet in γ Cephei/HD 196885 can maintain stability for e_{bin} as high as 0.6/0.46. Similar studies made by using the global MEGNO maps of e_{bin} vs. i_{pl} for given orbital parameters concur with our results from MLE and HS

and demonstrate that the planet in γ Cephei/HD 196885 can maintain stability for $i_{pl} \leq 25^{\circ}$ and $e_{bin} \leq 0.6/0.46$.

The MEGNO chaos indicator is effective in determining the quasi-periodic regions. The location of eccentricity-semimajor axis cross hairs in the MEGNO maps for the planets in γ Cephei and HD 196885 systems (Figs. 3.8a and 3.9a) are located well inside the quasi periodic region (blue) and in the teeth between the chaotic and quasi periodic regions, respectively. This resembles the global and local stability of the planets. These planets do not survive if the binary orbits are highly eccentric (see Figs. 3.10a,b).

The Hill stability time series for a planet is successfully measured using the numerical integration of orbital parameters and conversion into a potential related to the elliptic restricted three body problem. The measure of the Hill stability of the planets in γ Cephei and HD 196885 has shown changes in periodicity with the variation of i_{pl} and e_{bin} values. These periodicity are believed to have originated due to the differences in the time of interaction on the planet due to the secondary star near time of periastron passage for the binary.

A concise study of evolution of osculating parameters shows that they have insignificant variation in both of the systems for the nominal case. But, as I increase the i_{pl} values up to 25° the osculating values ($e\cos\varpi$ and $e\sin\varpi$) evolve causing the precession rate in γ Cephei and HD 196885 to increase. In the set of osculating parameters ($i\cos\Omega$ and $i\sin\Omega$), the inclination varies with a very small amplitude while the longitude of ascending node rotates in the full range $[0^{\circ}, 360^{\circ}]$. In case of HD 196885 these parameters display significant evolution, which provides possible evidence towards chaotic behavior in this regime.

Aside from the dynamical analysis of planets in stellar binaries, I am able to successfully test the reliability of Hill stability against the results obtained from both

MLE and MEGNO. Direct comparison of stability shows that the Hill stability test can be set as one of the three stringent criteria in the study of stable/unstable nature of a planetary orbit. Our results show that the HS indicator is comparable, in the context of determining the orbital stability, to other well known indicators. Like MLE and MEGNO, it has consistently predicted the stable/unstable nature of planets in binaries. Calculations show that the HS function predicts instability of orbits in comparable time with LE (case of γ Cephei). Also, unlike MEGNO maps, HS time series cannot produce definite quasi-periodic, chaotic or decreasing stability regions without considering a map of a larger parameter space.

CHAPTER 4

CHAOTIC DYNAMICS OF THE PLANET IN HD 196885 AB

Depending on the planetary orbit around the host star(s), a planet could orbit either one or both stars in a binary system as S-type or P-type, respectively. In this dissertation, I analysed the dynamics of the S-type planetary system in HD 196885 AB with an emphasis on a planet with a higher orbital inclination relative to the binary plane. The mean exponential growth factor of nearby orbits (MEGNO) maps are used as an indicator to determine regions of periodicity and chaos for the various choices of the planet's semimajor axis, eccentricity and inclination with respect to the previously determined observational uncertainties. I have quantitatively mapped out the chaotic and quasi-periodic regions of the system's phase space, which indicates a likely regime of the planet's inclination. In addition, I inspect the resonant angle to determine whether alternation between libration and circulation occurs as a consequence of Kozai oscillations, a probable mechanism that can drive the planetary orbit to a very large inclination. Also, I demonstrate the possible higher mass limit of the planet and improve upon the current dynamical model based on our analysis.

4.1 Background

The study of exoplanets has made a significant advance since the first planet around a solar type star, 51 Pegasi b (Mayor & Queloz 1995) was discovered almost two decades ago. The number of confirmed exoplanets has already reached 1822 as of September 22, 2014[1]. New exoplanets are being added almost everyday into the

[1] `www.exoplanet.eu`

database. The ultimate conquest of the contemporary exoplanet research is to find a planet within its respective habitable zone with a stable planetary orbit and a terrestrial mean density. Various ground based surveys and space based telescopes, such as the *Kepler*[2] mission and future missions such as the transiting exoplanet survey satellite (TESS) (Ricker et al. 2010) and the James Webb[3] space telescope are set for the detection and characterization of exoplanetary systems, which will deliver a promising future in the search for terrestrial planets that could support life. Meanwhile, the search for exomoons is also an ongoing process and recent work by Kipping et al. (2013) has produced a list of candidate hosts of such moons around transiting exoplanets. **?**) recently calculated the minimum required flux from the exoplanetary radio emissions in order to detect the exomoons using several ground based radio telescopes. Although an exomoon has yet to be detected, theorists have already determined relations to constrain an exomoon's habitability by considering energy flux (i.e., radiative and tidal) and orbital stability (Heller 2012; Cuntz et al. 2013).

The focus of this chapter, however, is on the study of the dynamics of an exoplanet whose orbital eccentricity and inclination relative to the binary plane are significantly higher than the median of those discovered. The orbital stability of such a system depends on various orbital parameters and the long-term stability is vital for life to develop under current theories. Thus, understanding the complete dynamics of a system bears vital requirement. Various numerical tools have been developed and used in the past to address the orbital configuration leading to the stability, instability or chaos of planets in a binary system. Quarles et al. (2011) used the maximum Lyapunov exponent (MLE), originally developed by Lyapunov (1907),

[2]`http://kepler.nasa.gov/`
[3]`http://www.jwst.nasa.gov/`

to determine the orbital stability or instability for the CRTBP case. The mean exponential growth factor of nearby orbits, MEGNO maps (Cincotta & Simó 1999) have been used to study the dynamical stability of irregular satellites (Hinse et al. 2010), and extrasolar planet dynamics (Goździewski & Maciejewski 2001; Goździewski et al. 2001). Recently, Satyal et al. (2013) used MLE, MEGNO and the Hill stability time series methods (Szenkovits & Makó 2008) to study the orbital perturbation of a planet due to the stellar companion in the binary systems of γ Cephei and HD 196885.

Planets that are formed from a planetary disk are expected to have near circular orbits due to tidal circularization, yet roughly 19% of known exoplanets with well-known orbital parameters have an eccentricity greater than 0.4[4]. This estimate, however, could be biased and may not include the true population. The actual intrinsic phenomenon on how such highly eccentric orbits are formed while maintaining orbital stability is not quite fully understood, however, some theories do exist that postulate such origins. Kozai (1962) and Lidov (1962) proposed a mechanism, now referred to as *Lidov-Kozai* mechanism, to explain the variations of a test particle's eccentricity and inclination. This mechanism was first applied to the exoplanets by Holman et al. (1997) while studying the chaotic variations in the eccentricity of the planet in 16 Cygni AB. Furthermore, its application to the planets includes the work done by Innanen et al. (1997), Wu & Murray (2003), Fabrycky & Tremaine (2007), Wu et al. (2007), Veras & Ford (2010), Correia et al. (2011), Lithwick & Naoz (2011), Naoz et al. (2011), Katz et al. (2011), Naoz et al. (2012), Naoz et al. (2013a) and Li et al. (2013). Some other mechanisms have also been proposed, such as planet-planet scattering to explain such variations (see for example, Rasio & Ford (1996); Chatterjee et al. (2008); Nagasawa et al. (2008)). In this work, I use the *Lidov-Kozai*

[4] `www.exoplanet.eu`

mechanism to explain such highly eccentric but stable orbits of the S-type planet, HD 196885 Ab. The planet is part of a binary star system (HD 196885 AB) whose eccentricity is observationally determined to be 0.48 and the planet's inclination is unconstrained which implies a value anywhere between zero and ninety degrees (for prograde motion) with the binary plane.

The dynamics of the planet in HD 196885 have been studied in the work by Satyal et al. (2013). In that study, investigations were performed in a restricted manner where the planet's inclination, $(i_{pl}) \leq 25^{\circ}$ with the binary plane, and the dynamics of the system was not fully explored. In this dissertation, I consider a full range of prograde orbits in i_{pl} value, from 0° to 90°, and made use of the chaos indicator, MEGNO, to produce maps which demonstrate regions of periodicity and chaos for a variety of initial conditions. For similar initial conditions, a dynamical *lifetime* map is produced by using the information about the planet's ejection *time* from the system or the collision *time* with the stellar host. Also, the dynamics of the system is studied in terms of the planet's maximum eccentricity. Then, the resonant angle is analyzed for evidence of a mean motion resonance at the best-fit location of the planet and for possible alternation between libration and circulation arising due to chaos induced by the Kozai oscillations.

If a system demonstrates quasi-periodic orbits (as in the case of MEGNO maps) and/or the planet survives the total simulation time (*lifetime* map), I consider it a stable system. If the planet gets ejected from the system or collides with the central body within the simulation time, it would be an unstable system. For some initial conditions the planetary orbit displays a chaotic motion, which I shall confirm from the evaluation of the time evolution of the resonant angle. Even though the motion is chaotic it does not mean that its unstable and the system can maintain (in some cases it has maintained) a stable configuration for millions of years.

Table 4.1. Best-fit orbital parameters of the HD 196885 system as obtained from (Chauvin et al. 2011). Mass of primary star, $m_A = 1.33\ M_\odot$. The planet's inclination (i_{pl}) is measured relative to the binary orbit, then for $i_{pl} = 0°$, the planetary orbit is coplanar with the binary orbit.

HD 196885	**B**	**Ab**
Mass (m)	0.45 $M_\odot$	2.98 M_J
Semimajor Axis (a)	21 ± 0.86 AU	2.6 ± 0.1 AU
Eccentricity (e)	0.42 ± 0.03	0.48 ± 0.02
Inclination (i)	0°	[0° - 90°]
Argument of Periapsis (ω_p)	241.9° ± 3.1	93.2° ± 3.0
Ascending node (Ω)	79.8° ± 0.1	0.0°
Mean Anomaly (M)	121° ± 45	349.1° ± 1.8

4.2 Theory

4.2.1 The Lidov-Kozai Mechanism

Kozai (1962) developed an analytical theory to explain the secular perturbations induced by Jupiter on the asteroids in the Solar System. Similar theory was developed by Lidov (1962) to study the evolution of orbits of artificial satellites of planets that are directly influenced by the gravitational perturbations of the Sun. For this, Kozai considered the perturber's (Jupiter) orbit to be circular. Thus the asteroid's vertical angular momentum and the secular energy is conserved and the system is integrable. As a consequence of the conservation of the quantity $\sqrt{1-e_{pl}^2}\cos i_{pl}$ the time evolution of eccentricity and inclination of the planetary orbit is anti-correlated, when the eccentricity is small, then the inclination is high and vice versa. For relative orbital inclinations less than 39.2 degrees the argument of pericentre circulates between 0° and 360° and the planet's orbit is precessing. This property remains true for other values of initial eccentricity. However, for relative inclinations larger than 39.2 degrees, the planet becomes a Kozai librator (Kozai regime) with it's argument

of pericentre locked and exhibiting either librations (oscillations) around 90 or 270 degrees. These libration centers are known to be stable fixed points.

A Kozai librator with an initially circular orbit will undergo a large variation in eccentricity and inclination within the Kozai cycles. For relative inclinations close to the critical value of 39.2 degrees, the argument of pericentre exhibits intermittent behaviour displaying alternations between circulations and librations. In general, the coupling between eccentricity and inclination provides an effective removal mechanism. For a large initial relative inclination the amplitude of the planet's eccentricity variation increases. Following Innanen et al. (1997) the maximum extent in eccentricity for a Kozai cycle can be expressed as,

$$(e_{max})_{pl} = \sqrt{1 - \frac{5}{3}\cos^2 (i_o)_{pl}}, \tag{4.1}$$

where $(i_o)_{pl}$ is the initial relative inclination of the planet. Eventually, for a large enough eccentricity, the planet is either ejected from the system or collides with the primary component rendering its orbit to be unstable.

However, the vertical angular momentum and the secular energy are conserved only when the pertuber's orbit is circular. When the perturber is eccentric or if the planet has non-negligible mass, the vertical angular momentum component of the planet and the perturber is not conserved and the planet shows qualitatively different behaviour. For such cases, Lithwick & Naoz (2011) and Naoz et al. (2013a) further developed the *Lidov-Kozai* mechanism discussed earlier and formulated for the eccentric perturber, which they have called it the *eccentric Kozai mechanism* (EKM). When the perturber has an eccentric orbit the quadrupole-order approximation is insufficient and requires the octupole-order term as well (Ford et al. 2000). Following Lithwick & Naoz (2011) and Naoz et al. (2013a), the energy function and the constant

of motion, F, in quadrupole and octupole term is, $F \equiv F_{quad} + \epsilon F_{oct}$ and the constant is given by

$$\epsilon \equiv \frac{a_{pl}}{a_{per}} \frac{e_{per}}{1 - e_{per}^2}, \tag{4.2}$$

where a_{pl} and a_{per} are the semimajor axis of a planet and pertuber respectively, and e_{per} is the pertuber's eccentricity.

In a binary star system with an S-type planet around the primary star, as in our case, the secondary star would be a perturber. When $e_{per} = 0$, $\epsilon = 0$, thus F reduces to the case with the quadrupole term only. Further mathematical set up of equations of motion concerning the quadrupole and octupole order terms can be found in Naoz et al. (2013a). During their study of the EKM, some of the remarkable results were obtained including the flipping of the planetary orbit from prograde to retrograde and its eccentricity reaching to the extreme values ($\sim$ 1). Two main cases have been discussed regarding the initial conditions in e_{pl} and i_{pl}: high eccentricity, low inclination (HeLi) and low eccentricity, high inclination (LeHi). Primarily, only the octupole term is in play during HeLi flip (Li et al. 2013) and both terms (quadrupole and octupole) are in play during LeHi flip (Naoz et al. 2011, 2013a). From Li et al. (2013), the flip criterion is given as

$$\epsilon > \frac{8}{5} \frac{1 - e_{per}^2}{7 - e_{per}(4 + 3e_{per}^2) cos(\omega_{per} + \Omega_{per})}, \tag{4.3}$$

where ϵ is the constant parameter (Eq. 4.2), e_{per}, ω_{per} and Ω_{per} are the perturber's initial eccentricity, argument of periapsis and ascending node, respectively.

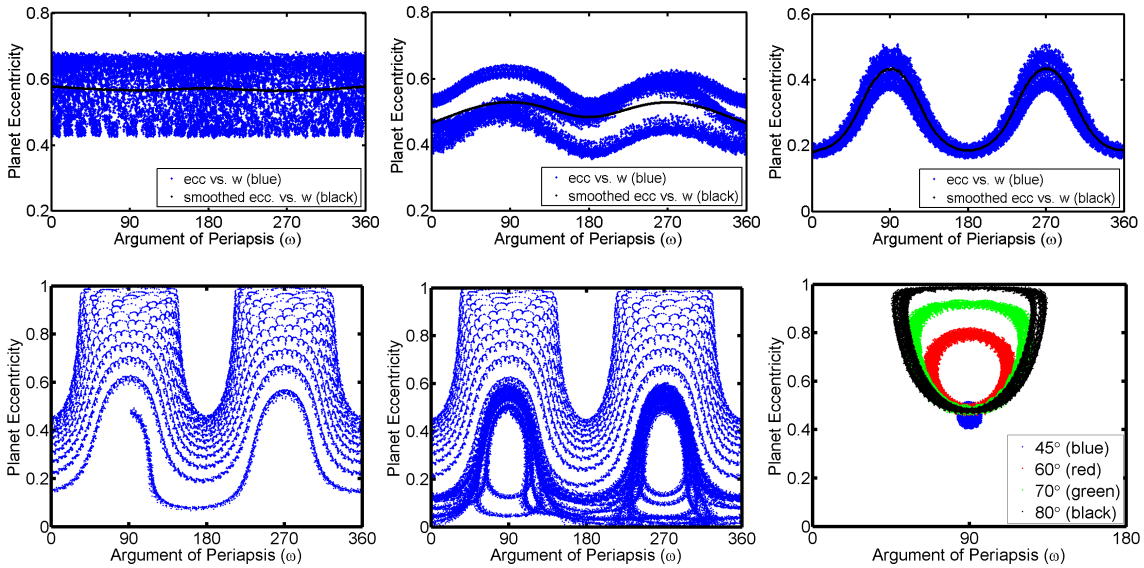

Figure 4.1. Evolution of the eccentricity and argument of periapsis for various choices of planet's orbital inclination with the binary plane, simulated for 1 $\times 10^5$ years [(a)Initial $i_{pl} = 0°$, (b)Initial $i_{pl} = 20°$, (c)Initial $i_{pl} = 35°$, (d)Initial $i_{pl} = 39.2°$, (e)Initial $i_{pl} = 39.7°$, (f)Initial $i_{pl} = 45°$, 60°, 70°, 80°]. The Savitzky-Golay smoothing function with third degree polynomial is used to smooth the high frequency data as shown in (a),(b) and (c). For the first three choices of i_{pl} values, the ω is circulating within 0° to 360°. In contrast to the coplanar case, the amplitude of circulation is varying and is maximum at 90° and 270° (b and c). When $i_{pl} = 39.2°$ (d), the ω shows circulation in the region of phase space with eccentricity amplitude maximum at 90° and 270°, and for even higher i_{pl} (39.7°) the phase space divides into two distinct regions where ω shows circulation and libration around 90° and 270° (e). This is, however, an unstable region where the amplitude of eccentricity oscillation reaches ∼1. When i_{pl} is set to 45°, 60°, 70° and 80° (f), the ω librates around 90° and the libration amplitude in eccentricity is found to increase with increasing i_{pl} until the planet collides with the central body for i_{pl} greater than 80° (Satyal et al. 2014b).

4.2.2 Numerical Approach and methods

Now I consider the motion of a planet of mass, m_{pl} around a star of mass, m_A. When calculating the initial conditions in position and velocity, I used the best-fit orbital elements, semi major axis (a), eccentricity (e), inclination (i), argument of periapsis (ω), ascending node (Ω) and mean anomaly (M), that are obtained from the radial velocity measurements (Chauvin et al. 2011). For any unconstrained

parameters, the values are taken in a range or considered zero. The list of orbital parameters of the HD 196885 system are given in Table 3.2. The subscripts *bin* and *pl* are used to denote the secondary binary component and the planet, respectively. The mean longitude (λ) that is used to calculate the resonant angle (Φ) is calculated from the longitude of the periapsis ($\varpi = \Omega + \omega$) and the orbit's mean anomaly (M), which is given as $\lambda = \varpi + M$.

Using the orbital integration package MERCURY (Chambers & Migliorini 1997; Chambers 1999), the built-in Radau algorithm was used to integrate the orbits of the system in astrocentric coordinates when investigating the evolution of orbital elements for a single initial condition and to produce a *lifetime* map for multiple initial conditions. MERCURY was effective in monitoring the ejection/collision of a planet due to close encounter with the secondary star and provided robust results for the purpose of determining the existence of orbital resonance. A time step of $\epsilon = 10^{-3}$ year/step was considered to have high precision because the error in change in the total energy and total angular momentum was calculated at each time step that fell within the range of 10^{-16} to 10^{-13} in both cases during the total integration period of 50 Myr. The data sampling (DSP) was done per year for shorter integration periods (up to 100 kyr) and per thousand years for longer integration periods. The *lifetime* map and the maximum eccentricity map are generated for 12,000 initial conditions in a_{pl} and i_{pl}, and simulated for 50 Myr.

4.3 Results and Discussion

4.3.1 The Phase Space Evolution

To observe the system that is evolving in the phase space, the planet's eccentricity (e) is plotted versus the argument of periapsis (ω), for various choices of the

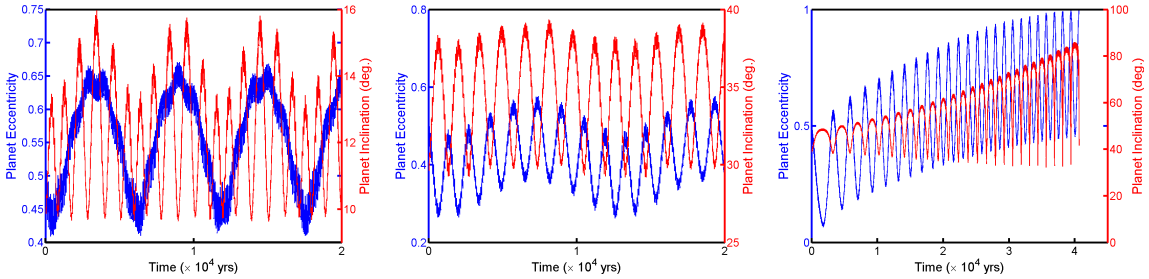

Figure 4.2. Planet's eccentricity and inclination time series when planet's initial orbital inclination with the binary plane is set at 10°, 30° and 39.2°. In these double-axis plots, the left y-axis has eccentricity and right y-axis has inclination plotted versus time along the common x-axis. The orbital integration was carried out for 50 Myr but (a) and (b) are truncated at 2×10^4 years to clearly demonstrate the oscillations of both elements (e and i). (c) is plotted up to the instability point ($\sim 4\times10^4$ years) after which the planet collided with the central body (Satyal et al. 2014b).

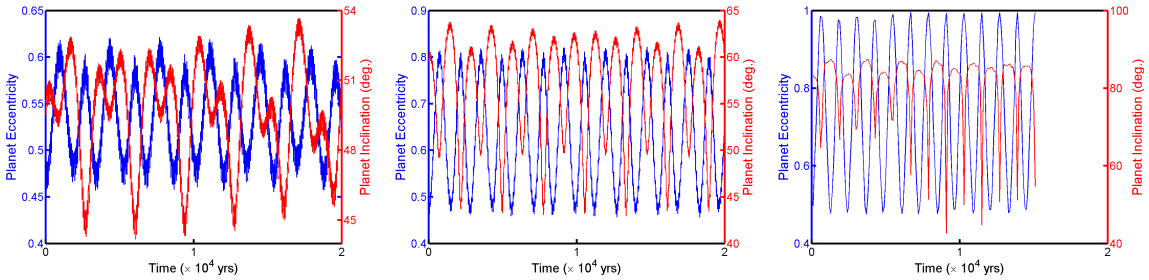

Figure 4.3. Planet's eccentricity and inclination time series when planet's initial orbital inclination with the binary plane is set at 50°, 60° and 83°. The time series at (a) and (b) are truncated at 2×10^4 years and the time series at (c) is plotted up to the instability point ($\sim 1.5\times10^4$ years) after which the planet collided with the central body (Satyal et al. 2014b).

planet's relative orbital inclination with the binary plane (Fig. 4.1). The Savitzky-Golay smoothing function is used to filter the data as I am interested in the secular dynamics of the system and the secular perturbation theory that initiates the Kozai mechanism in the case of inclined orbits. I find that, below 39° and for our choice of i_{pl} values, the phase space starts to evolve when ω starts to circulate between 0°

and 360°. The eccentricity, however, oscillates with large and increasing amplitude for increasing i_{pl} (for example 20° to 35°) while compared to the coplanar case (see Figs. 4.1a,b,c).

When the initial i_{pl} is set at 39.2°, the ω shows circulation only with eccentricity amplitude maximum at 90° and 270° (Fig. 4.1d), but the system becomes orbitally unstable as the e_{pl} reaches its maximum value causing the planet to collide with the central body within 50 Kyr. Further increment in the i_{pl} value to 39.7° makes the phase space divide into two distinct regions while the ω is found to circulate as well as librate (Fig. 4.1e). This is also a transition regime of the phase space beyond which the ω displays libration only. Holman et al. (1997) showed a similar behaviour in the momemtum variable (1-e^2) plotted versus its conjugate angle (ω) for a highly inclined ($i_{pl} = 60°$) planetary orbit.

Furthermore, when the i_{pl} is set in increasing order from 45° to 80°, the amplitudes of the e_{pl} oscillations is found to increase as well, and in this inclination regime the argument of periapsis only shows libration around 90° (Fig. 4.1f). The libration amplitude increases with the increase in the initial i_{pl} values, eventually entering a regime where the planet can escape from the system or collide with its host star when i_{pl} reaches a value greater than 82° and e_{max} approaches 1.0 (Eq. 4.1).

4.3.2 The Kozai Resonance

The evolution of a planet's eccentricity and inclination was further explored for a wide range of i_{pl} values. The conservation of the Kozai integral term (see Sec. 4.3.2) suggests that as the system evolves in time, the decrease/increase in planet's eccentricity is compensated by the increase/decrease in its inclination relative to the binary plane, also shown by Holman et al. (1997) for circular perturber and by Lithwick & Naoz (2011) for an eccentric perturber. For small initial i_{pl} values (i.e.,

10°) I found a constant-amplitude oscillation of e_{pl} and i_{pl} at the average values of 0.55 and 12°, respectively (Fig. 4.2a) for the integration period of 50 Myr. As the initial value of i_{pl} is increased the amplitude of oscillations of both parameters increase as well. In Fig. 4.2b I have shown a case for $i_{pl} = 30°$. In this double-axis plot, the y-axis on the left side indicates the time evolution of eccentricity from its best-fit value of 0.48. As the system evolves, the eccentricity varies between 0.25 and 0.55. The y-axis on right side illustrates the variation in inclination from its initial assigned value of 30°. The i_{pl} value oscillates between 30° and 40° and the variation in its amplitude from the initially assigned value behaves in an anti-correlated fashion to that of e_{pl}. Also, the variation in the e_{pl} agrees with the case when the perturber has an eccentric orbit, the inner orbit's eccentricity can reach extremely large values (Ford et al. 2000; Naoz et al. 2013a; Teyssandier et al. 2013). The x-axis in Figs. 4.2a and 4.2b are truncated at 20 Kyr to clearly demonstrate the oscillations of the two parameters, (e_{pl} and i_{pl}). The amplitude of the oscillations merely changed during its evolution for given total integration time.

When the initial i_{pl} value is further increased to 39.2°, the planet follows a path to instability within 40 kyr through a growing value of eccentricity. It is also found that there is a small instability window (most of the time the planet collided with the central body) when i_{pl} is set at ∼(39° - 40°). The time series plot of e_{pl} and i_{pl} (Fig. 4.2c) shows increasing values of the planet's eccentricity and inclination until it reaches an extreme value ∼1 and i_{pl} oscillates up to 80°, hence minimizing the periastron distance and eventually forcing the planet to collide with its host star. From a theoretical aspect, it can be inferred that when the relative inclination hits the critical angle mark ($i_c = 39.2°$), the long-period oscillations between eccentricity and inclination ensue. The initial eccentricity becomes insensitive leading to the forced eccentricity that is the basis for the Kozai resonance. The other factor causing the

planet to exhibit Kozai cycles is the libration of the argument of periapsis (ω) around 90°, whose significant evolution is observed in Fig. 4.1 for i_{pl} greater than 39°. I did not consider the tidal dissipation within the regimes of close approach which may as well produce misalignment (Winn et al. 2010). Also, general relativity is not included in our calculations the precession, which can lead to large eccentricity oscillations (Naoz et al. 2013b; Antonini & Merritt 2013).

For greater orbital inclination values, such as, when initial i_{pl} is set to 50° (or, 60°) (Fig. 4.3a,b) the amplitudes of eccentricity and inclination oscillations reach as high as $\sim$ 0.6 and 53° (or, $\sim$ 0.8 and 64°), respectively, and the system continues to maintain the periodic orbits throughout the integration period of 50 Myr. Also, further increasing the i_{pl} value pushes e_{pl} to its extreme limit resulting in the planet-star collision when the i_{pl} value is increased beyond 82°. Above the critical value of the planet's orbital inclination with the binary plane ($i_c = 39.2°$), the precession of the argument of pericentre is replaced by libration around 90° as discussed earlier. Satyal et al. (2013) encountered a similar dynamical behaviour in their study of the planet in the HD 196885 system for the planet's orbital inclination less than 25 degrees. For higher initial i_{pl}, as shown here, the secular perturbation causes the e_{pl} and i_{pl} values to oscillate with higher amplitudes, which can eventually cause instability in the system due to the collision of the planet with the central body or escape due to a parabolic or hyperbolic orbit. For example, when the initial $i_{pl} = 83°$ and the e_{pl} is forced beyond 1 within a short integration period (15 kyr, Fig. 4.3c).

For specific initial conditions, Lithwick & Naoz (2011) showed that the planetary orbit can flip when the criterion given in Equation 4.3 is satisfied. But the initial parameters from our system does not satisfy this criterion despite the presence of the highly eccentric perturber. For the given initial parameters of HD 196885 AB, $\epsilon = 0.063$ (ϵ is a constant term given by Eqn. 4.2) while the value obtained from Eqn.

4.3 is 0.174. Thus, the planet is not expected to flip its orbit, which is in agreement with Fig. 4.3c and Fig. 4.4. The planet's maximum eccentricity reaches the extreme values, from 0.7 to ~ 1, (see the maximum eccentricity map, Fig. 4.4) for the orbital inclination greater than 55°; nonetheless, the planet survives the total integration time until the i_{pl} is raised to 82° . The e_{max} stays relatively low, between 0.48 and 0.68, for the i_{pl} values less than 55° excluding the case when i_{pl} is $\sim$ 39°. Before reaching the flipping point (90°) the planet gets ejected from the system when $i_{pl} \geq$ 82° and the e_{max} reaches close to 1.0 within the integration time. I note that e_{max} appears to decrease in Fig. 4.4 for very high inclinations (85°−90°), but this is due to the approach to instability occurring faster than our data output frequency.

4.3.3 The MEGNO and the MMR Analysis

I generated the MEGNO maps considering a wide parameter space of the planet's initial inclination and semimajor axis, which illustrates variations in the quasi-periodic and chaotic phase space for varying i_{pl} and a_{pl} values (Fig. 4.5). I found that, for i_{pl} less than 39°, the best-fit value of a_{pl} (the vertical line at 2.6 au) lies within the chaotic region. However, it's important to note that a chaotic orbit does not necessarily imply an unstable one, as it is shown through the orbital integration of the selected initial conditions. Also, the global *lifetime* map of i_{pl} vs. a_{pl} (Fig. 4.6) shows which initial conditions are the best suited for the full integration time. The colour code in the *lifetime* map is based on the planet's survival, ejection or collision time where the lightest colour represents the full survival of the planet. And the dark coloured vertical bands signifies instability, which means that the planet at these initial conditions did not survive the total simulation time of 50 Myr.

The mean motion resonance (MMR) associated with the chaotic regions in the MEGNO maps can be estimated by calculating its position from the perturbation

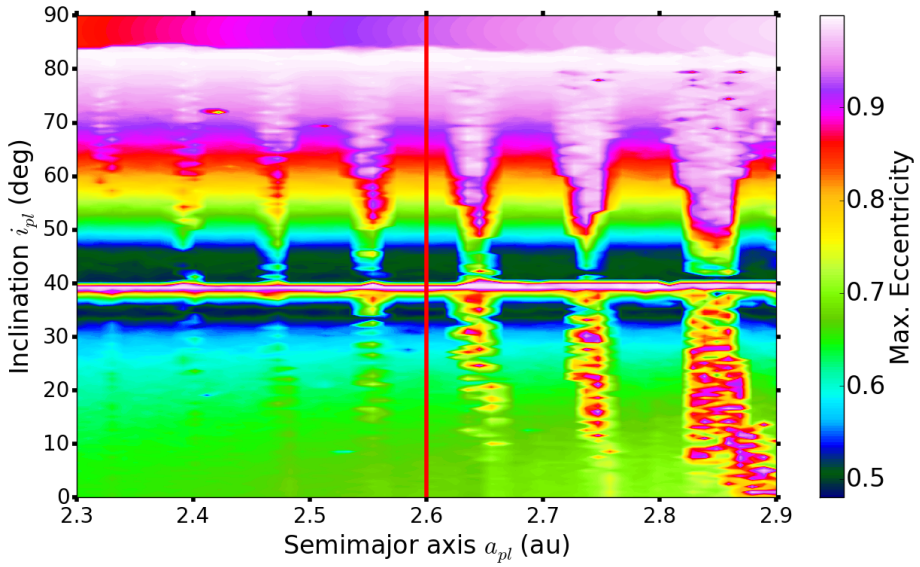

Figure 4.4. A maximum eccentricity (e_{max}) map of the planet, HD 196885 Ab, for varying i_{pl} and a_{pl}, simulated for 50 Myr. The colour bar indicates the e_{max} reached by the planet during the total simulation time, which also includes the cases when the planet suffers an ejection or collision (especially when e_{pl} reaches a value greater than 0.9). The darker colour represents the best-fit e_{pl} parameter (0.48) and the lightest colour represents the e_{max} value the planet attained for the respective choices of initial conditions in i_{pl} and a_{pl}. The red line at 2.6 au is the best-fit semimajor axis of the planet. This map compliments the *lifetime* map (Fig. 4.6) in a way that the vertical instability bars are located at the same regions where the planet's e_{max} exceeds 0.7 (Satyal et al. 2014b).

theory. For the best-fit values of the planet's and binary semimajor axes, and masses of the stars, the ratio of the $(p+q)/p$ commensurability can be calculated as (see Murray & Dermott (1999)),

$$\frac{p+q}{p} = \left(\frac{a_{bin}}{a_{pl}}\right)^{\frac{3}{2}} \left(\frac{m_A}{m_A + m_B}\right)^{\frac{1}{2}}, \tag{4.4}$$

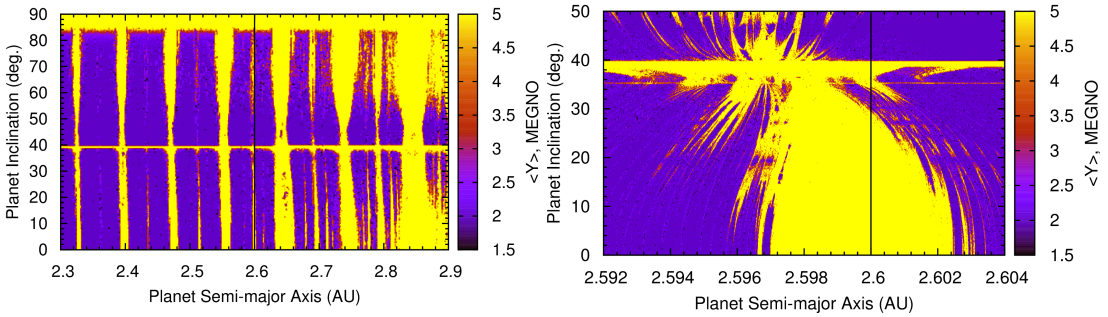

Figure 4.5. MEGNO maps indicating the quasi-periodic and chaotic regions of the giant planet in the HD 196885 system for inclination varying from (left) 0° to 90° and semimajor axis ranging from [2.3-2.9] au, simulated for 2 $\times 10^5$ years. Vertical line indicates the location of the best-fit semimajor axis of the planet at a_{pl} = 2.6 au. A small area along the vertical line and for lower i_{pl} region is magnified to clearly differentiate between the quasi-periodic and chaotic regions (right panel) and simulated for 8 $\times 10^5$ years. The planet's *near* 39:2 MMR is located slightly left of the planet's best-fit location. The MMR stops when i_{pl} reaches $\sim$ 30°, with a small semi quasi-periodic region extending from 30° to 34° which I expect to vanish for longer simulation time. Yellow region signifies the chaotic orbits within the total simulation time and dark purple region signifies the periodic orbits. The colour bar indicates the strength in the value of MEGNO, $< y >$ (Satyal et al. 2014b).

where m_A and m_B represent masses of the primary and secondary star, respectively; q is the order of the resonance and p is its degree. To search for chaos associated with (p+q)/p MMR, I considered the resonant angle (Φ) of the form

$$\Phi = k_1\lambda_{bin} + k_2\lambda_{pl} + k_3\varpi_{bin} + k_4\varpi_{pl} + k_5\Omega_{bin} + k_6\Omega_{pl}, \tag{4.5}$$

where the coefficients follow the relations k_1 = p+q, k_2 = -p, and $\sum_i k_i = 0$. The mean longitude λ is a function of the mean anomaly, M, and longitude of pericenter, ϖ. Also, the sum of k_5 and k_6 is even as required by symmetry in the d'Alembert rules.

For the planet at 2.6 au from the primary component an interaction with the mean motion resonance (MMR) is found to be *near* a 39:2 commensurability with

the secondary component (some of the angles in Fig. 4.7 show a temporary lock). The time evolution of the angles $\varpi_{pl} - \varpi_{bin}$ (secular resonance, Fig. 4.7,f) shows circulation between 0° and 360° when the i_{pl} is set at lower values (for example 0°), which suggests that the observed chaos is caused by the MMR. Secular resonance at the semi quasi-periodic region (i_{pl} = 35°) shows circulation as well, but with a different orientation (Murray & Dermott 1999). Then, the MMR value is used to search for a librating resonant angle (Eq. 4.5), for k_1 = 39 , k_2 = -2, and various other combinations of k_3, k_4, k_5 and k_6 due to the influence of secular components. In our case, the i_{pl} was varied with respect to the binary orbital plane and the orbits were integrated using astrocentric coordinates, considering the primary at the origin. Thus, k_5 in Equation 4.5 would be zero as Ω_{bin} becomes undefined (i_{bin} = 0°) and convention dictates that it be set to zero.

Initial conditions for different i_{pl} values, but along the best-fit semimajor axis line, were picked where the measure of MEGNO is chaotic (Fig. 4.5, right panel), and the orbits were integrated for a short period with a high data sampling frequency. I would expect the resonance angle (Φ) time series to alternate between modes of circulation and libration for initial conditions taken from the chaotic region and Φ to circulate only when the initial condition is taken from the quasi-periodic region. At 0°, 10°, 31° and 35°, Φ is found to librate and circulate as expected for chaotic behaviour (Fig. 4.7, a-d). This also confirms the earlier indication of the planet's interaction with a near 39:2 MMR with the secondary star. One of the factors inducing chaos in the region of low inclination orbit is possibly due to this near 39:2 MMR. The MMR in the case of higher inclination orbit changes its dynamical character which results in the periodic orbits. The location of the planet (vertical line at 2.6 au) is almost at the center of the MMR, thus minimizing the amplitude of the libration. The 39:2 MMR has a minimal effect for i_{pl} greater than 40° and the planet enters a quasi-periodic

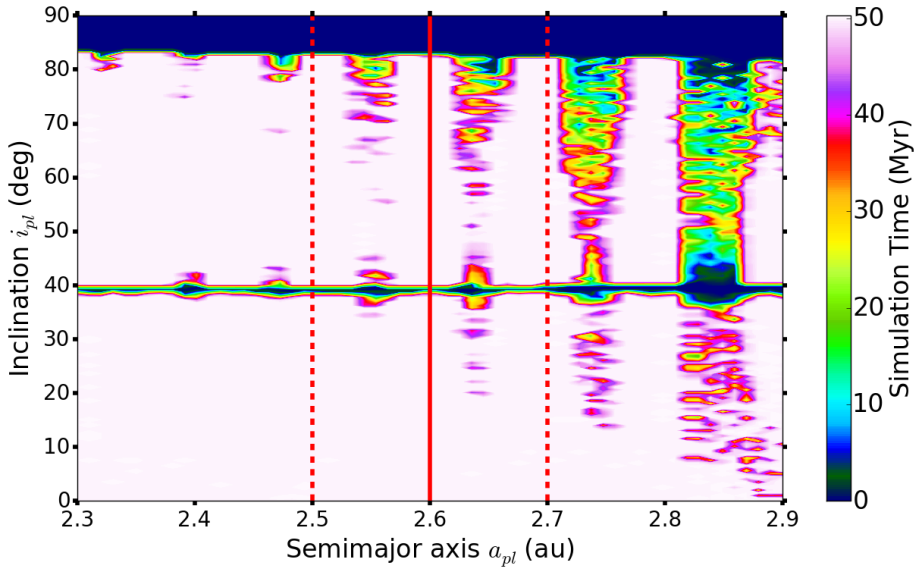

Figure 4.6. A global dynamical *lifetime* map of the planet, HD 196885 Ab, for varying i_{pl} and a_{pl}, simulated for 50 Myr. The colour bar indicates the survival time, where darker colour represents the instability (ejection or collision) and the lightest colour represent the stability (survival) up to the integration period. The solid red line at 2.6 au is the best-fit semimajor axis of the planet. Two dotted lines indicate the observational uncertainty of ±0.1 au (see Table 1). The vertical bars evident in Figs. 4.4 and 4.5 at 2.45, 2.55, 2.65, 2.75 au also appear (Satyal et al. 2014b).

region for i_{pl} up to 55°, a region where the e_{max} deviates least from its best-fit value. The resonant angle is found to circulate only in these quasi-periodic regions. As seen in Fig. 4.7e Φ plotted for the initial conditions at 50° shows circulation. This gives a strong evidence that one of the factors responsible for the chaos below 39° is produced by the near 39:2 MMR interaction. Also, the secular perturbation induced by the precession of ω and Ω is found to contribute to the observed chaotic dynamics of the system in the Kozai regime. The libration and circulation of resonant angle seen in Fig. 4.7 is obtained only when the coefficients of ϖ_{pl} and Ω_{pl} are included in the Φ term.

A small region of possible quasi-periodicity appears when the initial i_{pl} lies between 30° and 34° (Fig. 4.5 right panel). This seems like a periodic region but the

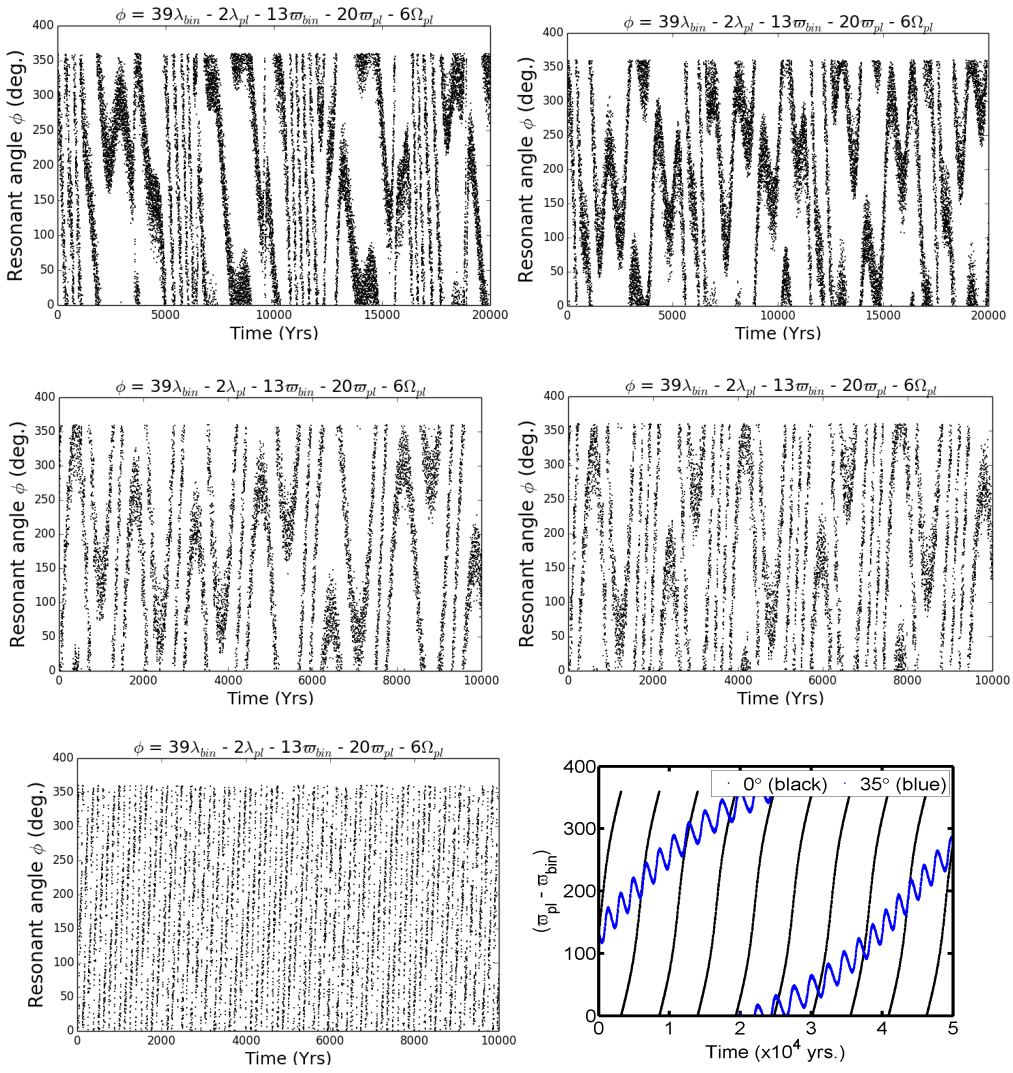

Figure 4.7. The time evolution of resonant angles (Φ) calculated for different i_{pl} values (0°, 10°, 31°, 35°, 50°, 0°,35°) but along the best-fit location of semimajor axis (a_{pl} = 2.6 au). The location for Φ angle test is chosen from MEGNO map (see Fig. 4.5) where measure of MEGNO ($< y >$) is quasi-periodic (e) and chaotic (a, b, c and d). (f) shows the time evolution of the angles ($\varpi_{pl} - \varpi_{bin}$) for i_{pl} values at 0° and 35° (Satyal et al. 2014b).

resonance angle test (Fig. 4.7c) shows that the Φ is found to circulate and librate, which indicates this region as a chaotic zone. The small black and red dots in this region are indicative that many of these initial conditions have not had enough time

to reveal their true nature (quasi-periodic or chaotic). What I called before a quasi-periodic region and expected the circulation of Φ revealed itself as a region of complex dynamics with many overlapping and interacting resonances.

A strip of unstable chaos is observed when the initial i_{pl} ranges between $\sim$(39° - 40°) (Fig. 4.5, right panel) and for any choice of a_{pl}, from 2.3 au to 2.9 au. The instability at this region is also confirmed by the *lifetime* map where the planet is found to collide with its host star. The MEGNO has been successful in determining the chaotic region surrounding this instability point. The minimum critical angle ($i_{pl} \geq 39.2°$) required to initiate the Kozai mechanism lies within this inclination regime. Once the Kozai resonance phenomenon is triggered, it drives the planet into higher inclination orbits (hence higher eccentricity) causing the planet to collide with the primary. However, beyond 40° and less than 55° the planet maintains quasi-periodic orbits even though it is subject to the Kozai resonance. The observed horizontal stripe in the MEGNO map at $i_{pl} \sim 39°$ can be considered as a separatrix line, which separates the phase space from circulation when $i_{pl} < 39.2°$, and libration when $i_{pl} \geq 39.2°$.

The MEGNO maps displayed quasi-periodic orbits along the best-fit a_{pl} value (black line, Fig. 4.5) and for i_{pl} values greater than 40° and until it rises as high as $\sim$55° above the binary plane. Beyond this inclination regime, the maps have displayed the chaotic orbits. The MEGNO shows an overall effectiveness at indicating the MMR locations, and the chaotic and periodic regions of the system's phase space. In addition, the dynamical maximum eccentricity and *lifetime* maps addressed the caveats of chaos seen in the MEGNO maps to discriminate regions that are truly unstable or merely chaotic within the integration period.

The planet's interaction near the 39:2 MMR with the secondary is observed when the mean best-fit value of semimajor axis is 2.6 au. When the planet's location

is moved to 2.58 au and 2.68 au (but within the observational uncertainty limit), the planet is found to exhibit oscillations due to the 20:1 and 19:1 MMRs, respectively.

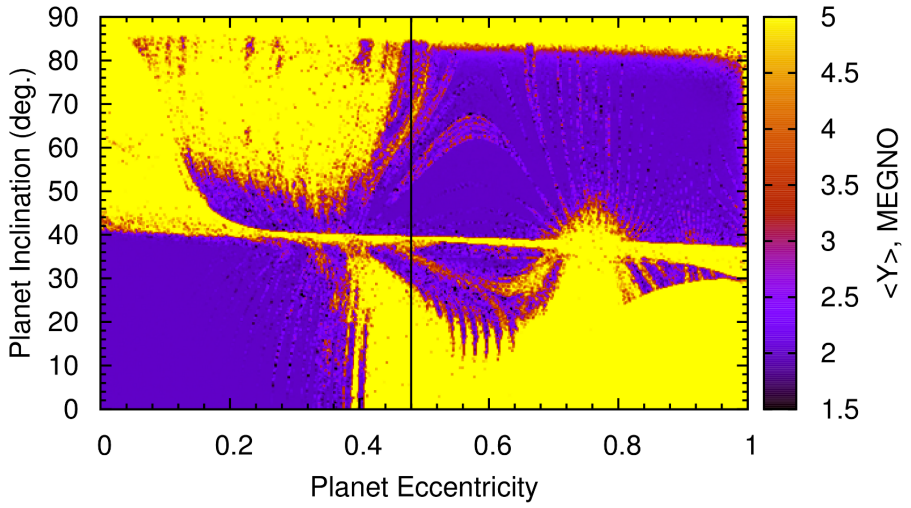

Figure 4.8. MEGNO maps indicating the periodic and chaotic orbits of the giant planet in HD 196885 for inclination varying from 0° to 90°, plotted versus the eccentricity and simulated for 2 $\times 10^5$ years. Vertical line indicates the planet's best-fit location at $e_{pl} = 0.48$ (Satyal et al. 2014b).

The planet's orbital motion is also analysed in the varying i_{pl} and e_{pl} plane (Fig. 4.8) to display possible periodic and chaotic regimes. The vertical line at $e_{pl} = 0.48$ indicates the planet's best-fit location, and, like in the previous case (Fig. 4.5), the planet clearly lies in chaotic zone for $e_{pl} > 0.4$ and $i_{pl} < 30°$. Driven by the Kozai resonance, a similar chaotic stripe appears at $i_{pl} \sim 40°$. Periodic regions continue beyond this angle, however some chaotic islands do appear for i_{pl} greater than 55°.

The discovery of the planet in the HD 196885 system (Chauvin et al. 2011) using the radial velocity (RV) technique only allowed the determination of the planet's minimum mass of $2.98 M_J$. I performed a test to indicate the periodic and/or chaotic regions of the system for variations in the planet's mass (m_{pl}) ranging from $2 M_J$ to

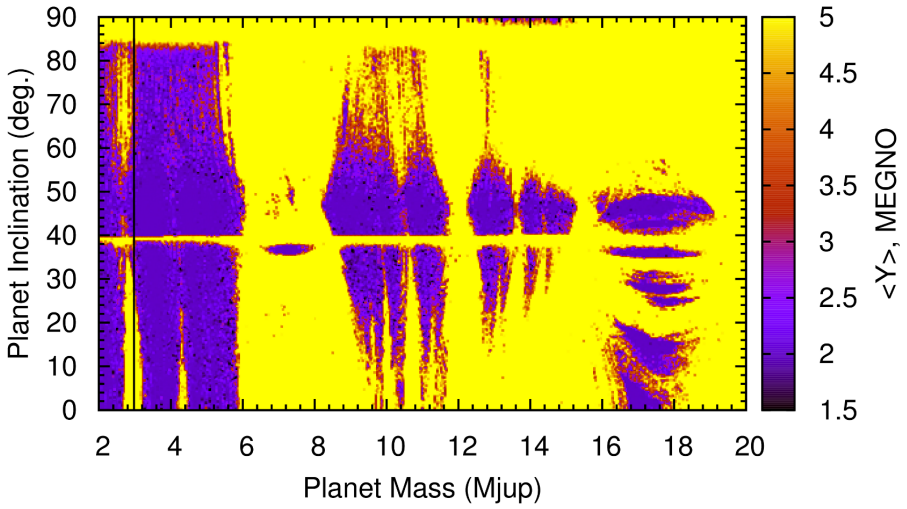

Figure 4.9. MEGNO maps indicating the periodic and chaotic orbits of the giant planet in HD 196885 for inclination varying from 0° to 90°, plotted versus the planet's mass and simulated for 2 $\times 10^5$ years. Vertical line indicates the planet's best-fit location at $m_{pl} = 2.98 M_J$ (Satyal et al. 2014b).

$20 M_J$ and i_{pl} varying from 0° to 90° (Fig. 4.9). The map indicates that quasi-periodic regions exist for various combination of m_{pl} and i_{pl}. The system displays periodic orbits for m_{pl} mostly between $3 M_J$ and $6 M_J$ with a small chaotic region around $4.5 M_J$ plus the exclusion of chaotic region at $\sim 40°$. The chaotic region continues below 30° at the best-fit semimajor axis location of the planet. The map indicates other possible periodic islands for higher mass values of the planet specifically for i_{pl} between (40° - 50°) and m_{pl} between $\sim$ (8.5 - 11.5)M_J, (12.5 - 15)M_J and (16 - 19)M_J.

4.4 Summary

Based on the above analysis, the best configuration for the planet to display quasi-periodic orbits is when the planet's orbital inclination relative to the binary plane lies between 41° and 55°. Chauvin et al. (2011) made a similar suggestion re-

garding the planet's inclination that a high relative inclination favours for the periodic orbits. Also, Giuppone et al. (2012) found that the planet has either coplanar orbits (prograde and retrograde) or highly inclined orbits near the *Lido-Kozai* equilibrium points, i - 90° = ±47°. This range of angles gets smaller when the planet's mass is increased more than the current value of $2.98 M_J$. The planet can have an interaction with the near 39:2 MMR from perturbations of the secondary component of the binary which appears to be responsible for the chaotic region as seen in the MEGNO maps below 39°. The plots of the resonance angle time series for the near 39:2 MMR clearly demonstrate the circulation and libration of Φ based on the choices of initial condition. The planet's orbital configuration below 39° is proven chaotic, and hence lesser possibility for the planet to be in that regime under the current assumptions of planetary formation.

The best-fit value of the planet's eccentricity was set at 0.48. Then the system was evolved for 50Myr and the maximum e_{pl} value was calculated in a_{pl} vs. i_{pl} parameter space. The e_{pl} is found to deviate least from its best-fit value when i_{pl} is at ∼35° and ∼(40°-50°), thus, these regions are expected to demonstrate the most quasi-periodic regimes for the planet. The high amplitude oscillation in e_{pl} below 35° mainly arises due to the planet's secular interactions with the secondary. The perturbation from the secondary may have forced the planetary embryo or protoplanet into precession during its early formation stage, eventually driving the planet into high inclination orbits.

The planets higher mass is possibly constrained between (3 - 6)M_J; however, these choices also depend on the choice of planet's orbital inclination and it is mostly favorable when m_{pl} is less than $6 M_J$ and i_{pl} less than ∼ 55°, with some exceptions of chaotic islands (Fig. 4.9). The planetary mass higher than $9 M_J$ and up to $19 M_J$ is likely when the planet's orbital inclination lies in a smaller regime, somewhere

between 40° and 50°. A possibility of having any other terrestrial planets within the 2.6 au region around the primary is less likely. The circumprimary disc can be strongly hostile to planetesimal accretion in this region (Thebault 2011).

CHAPTER 5

EXOMOON DETECTION

In chapter 1, I briefly discussed some of the methods that are currently used to detect exoplanets, which includes the transit method, radial velocity method, direct imaging and so on. Here I focus on the detection of exoplanets based on their orbital stability and other dynamical properties. Also, I present a possible detection of exomoon through observation of radio emissions based on the paper I co-authored (Noyola et al. 2013).

5.1 Exomoon Detection: A Theoretical Approach

Jupiter has a huge magnetic field lines connecting its polar regions. One of its moon, Io, while orbiting around the planet produces currents along the field lines. These currents then generate and modulate radio emissions along their paths via the electron-cyclotron maser instability. Analyzing and extrapolating these processes, it is suggested that such modulation of planetary radio emissions may reveal the presence of exomoons around the giant planets in exoplanetary systems. As a case study, we calculated a telescope flux sensitivity for possible moons orbiting Gliese 876 b and Epsilon Eridani b.

5.2 Background

More than 1822 have been confirmed as of September 22, 2014[1], yet no exomoons have been found due to the limited observational techniques. Our Solar

[1] `www.exoplanet.eu`

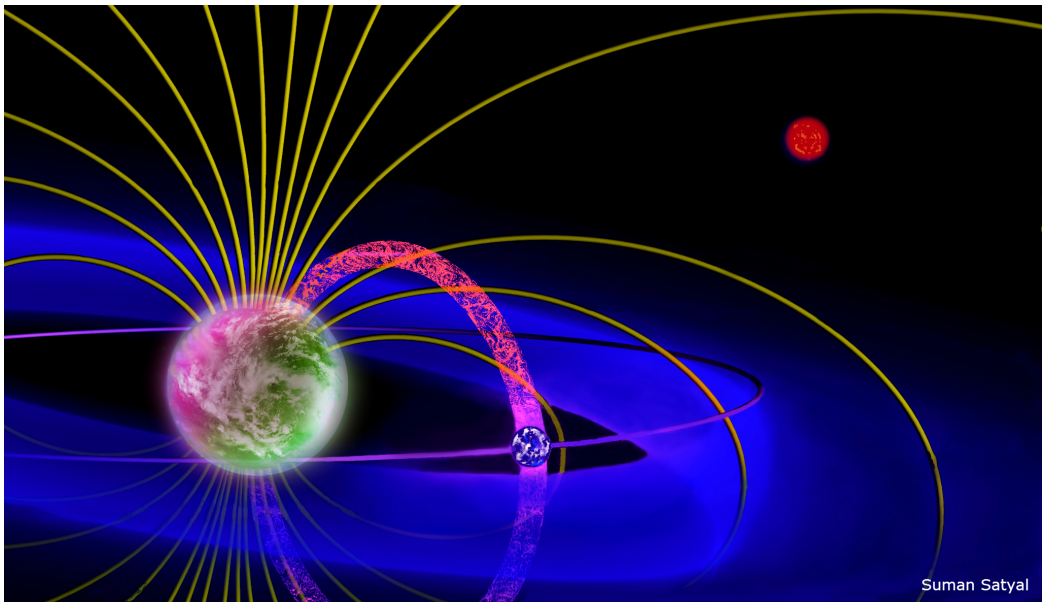

Figure 5.1. Schematic of a plasma torus around an exoplanet, which is created by the ions injected from an exomoon's ionosphere into the planet's magnetosphere. The ionosphere could be created due to the volcanic activity on the exomoon's surface, however, if an exomoon is large enough it can hold its own thick atmosphere, which then will give rise to an ionosphere. Image Credit: Suman Satyal.

System is home to hundreds of moons, which easily leads us to a belief that there must be some similar planetary systems hosting exomoons. There has been a continuous search using various detection techniques and within the data collected from NASA's *Kepler*[2] Space Telescope.

We made a theoretical approach by using Io controlled decametric (Io-DAM) emissions as a basis to demonstrate how the presence of exomoons around the giant exoplanets may be revealed by the same modulation mechanism. The required physical conditions for such interaction are determined and then asses the feasibility of our model by providing a possible exomoon detectability window.

Io is an intensely volcanic moon orbiting inside Jupiter's magnetosphere. The volcanic activity creates a light atmosphere of SO_2 around Io, which ionizes to create

[2]`http://Kepler.nasa.gov/Mission/discoveries/candidates/`

an ionosphere (Lopes & Spencer 2007). This ionosphere then injects ions into Jupiter's magnetosphere to create a plasma torus that orbits Jupiter's magnetic equator at an angle of 9.6° from the rotational equator, and co-rotates with the magnetic field at a speed of 74 kms^{-1} (Su 2009). Io orbits Jupiter at a linear speed of 17 kms^{-1}, so Jupiter's magnetic field passes Io at a speed of 57 kms^{-1}. The speed difference gives rise to a unipolar inductor (Grießmeier et al. 2007) that induces a current across Io's atmosphere of a few million amps. The current then accelerates the electrons that produce the characteristic radio emissions (Crary 1997). It must be noted that while volcanism is essential to the formation of a dense ionosphere around Io, such process might not be required for larger moons, since moons like Titan are already large enough to sustain a thick atmosphere, which in turn can give rise to an ionosphere.

Furthermore, the interaction between Io and the plasma torus gives rise to Alfvén waves (Belcher 1987). The precise mechanism by which Alfvén waves interact with the torus is complex, and several analytical and numerical models have been proposed. In these models, Alfvén waves produce electric fields parallel to Jupiter's magnetic field lines, which then transport and accelerate electrons towards Jupiter's magnetic poles (Su 2009; Crary 1997; Neubauer 1980, and references therein). The electrons traveling through the field lines create a cyclotron maser which then emits radio waves whose existence in the Jupiter-Io system has been observationally verified (Crary 1997; Mauk et al. 2001).

These studies of exoplanet-moon interactions are based on an extrapolation of both Io's plasma environment, and Jupiter's magnetic field to different scenarios that could potentially be encountered in newly discovered planetary systems. For mathematical details on the calculations of the maximum intensity of the radio emissions, the magnetic field and plasma properties, and the dependence of the radio emissions on various parameters, please refer to Noyola et al. (2013).

5.3 Detectability Window

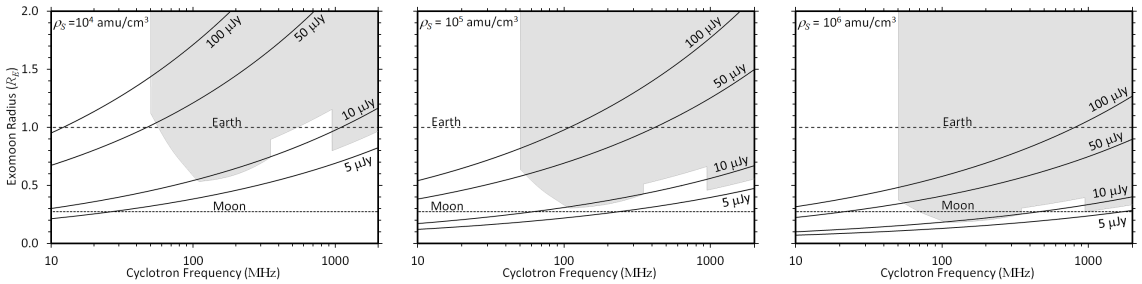

Figure 5.2. Curves of output flux, S, plotted in the $R_S - f_C$ plane for several plasma densities. The radii of detectable exomoons which are 15 light-years away plotted as a function of the host exoplanet's cyclotron frequency for several flux sensitivity values. From left to right, the panels show results for plasma densities of $10^4, 10^5$, and $10^6 amu/cm^3$. The shaded area corresponds to the potential detection capabilities of a fully implemented SKA telescope. 1 Jansky = 10^{-26} Wm^{-2}Hz (Noyola et al. 2013).

The cyclotron frequency is calculated using $f_C = eB_{pole}/(2\pi m_e)$, where e is the electron charge, m_e is the electron mass, and we use the magnetic field strength at the poles of the exoplanet, B_{pole}, because that is where most of the radio emissions occur. At the poles of the planet, the magnetic field is twice as strong as it is at the equator. Hence, the strength of the magnetic field at the poles is expressed as $B_{pole} = 2(r_{Opt}/R_P)^3 B_S$, where R_P is the radius of the exoplanet. Under this assumption, the cyclotron frequency increases as M_P^K, thereby limiting the amount of exoplanets that a telescope could successfully scan for exomoons. Nonetheless, there is still a wide range of frequencies within which an exomoon with radius $\leq 1R_E$ could be detected up to 15 light years away, if the plasma density ρ_S of the system is at least $10^4 amu\ cm^{-3}$, and if the telescope's sensitivity is at least tens of μJy (see Fig. 5.2).

The proposed SKA telescope, if fully implemented, could even detect Mars-size moons ($\sim 0.532R_E$)[3] in this case, if present. The range of detection of SKA is shown as the shaded areas shown in Fig. 5.2. Also, it must be noted that in reality these systems emit over a range of frequencies instead a single one, so the range of detectable systems is effectively larger than shown here. The calculation of the whole frequency band will be treated in future studies. Regarding R_P, a survey of currently known gas giants shows great variability in the value of this parameter. Nonetheless, for large planetary masses $R_P$seems to converge to a value close to Jupiter's radius, R_J. Furthermore, many authors (e.g. Zarka et al. (2001)) assume that $R_P = R_J$ unless the exoplanet's radius is explicitly known. Thus, we also assume $R_P = R_J$ to be the general case.

Applying our results to the exoplanet Epsilon Eridani b (1.55 M_J, 10.5 light years away), we find that a telescope with a flux sensitivity of $S \leq$50 μJy around 49 MHz could detect exomoons with radius between 0.24 R_E for high $\rho_S(\sim 10^6 amu\ cm^{-3})$ and 0.73 R_E for low $\rho_S(\sim 10^4 amu\ cm^{-3})$. For comparison, the Moon is $\sim$0.273 R_E. For another nearby exoplanet, Gliese 876 b (2.28 M_J, 15.29 light years away), a telescope with similar sensitivity around 93 MHz could detect an exomoon with a radius between 0.28 and $0.86R_E$, depending on ρ_S. In both cases, a fairly large minimum radius is required for exomoons to be detectable, unless there is a large amount of plasma present. In fact, to find an exomoon of radius 2500 km (similar to Mercury or Titan) orbiting Epsilon Eridani b, we would need a telescope with a flux sensitivity of 14 μJy if ρ_S is low. Nevertheless, improvements to radio telescope technology, and observational techniques could one day make it possible to reach these sensitivities.

[3]Assuming 2 pol., 1 hr integration, and 16 MHz bandwidth

5.4 Summary

The primary goal of this study was to find a set of conditions that would allow detection of an exomoon through the radio emissions it induces on its host exoplanet, and to assess whether these conditions are attainable by modern radio telescopes.

An exomoon orbiting Epsilon Eridani b, with radius as low as 0.24 R_E, lies in the detectable range of telescopes with sensitivity $S \leq 50$ μJy. However, detection of a Titan or Mercury-sized exomoon under low plasma conditions would require a telescope with flux sensitivity of ~ 14 μJy or better.

The model presented here still requires several refinements, such as including the effects of magnetic exomoons, finding better constraints on T_P and ρ_S, and calculating a complete emission spectrum rather than a single cyclotron frequency. Nonetheless, it is still our hope that the results presented here will give new insight to the observational community, and stimulate searches for the modulation of exo-planetary radio emissions caused by the presence of exomoons.

CHAPTER 6

A THEORETICAL PREDICTION OF NEW EARTH-MASS PLANETS: CASE STUDY OF GJ 832

6.1 Background

The study of orbital dynamics of planetary system in GJ 832 shows potential of hosting multiple planets in close orbits. My emphasis is on the phase space analysis of GJ 832c (inner planet) and the long-term stability of a hypothetical Earth-mass planet(s) injected in between the inner and outer (GJ 832b) planets. The orbital parameters of the inner planet are not well constrained for eccentricity, inclination and ascending node. I aim to minimize the error in the planet's eccentricity and locate its inclination regime. The stability of the system is defined in terms of its *lifetime* during the orbital integration and global parameter maps, displaying the maximum eccentricity (e_{max}) attained in the evolution process, are generated to observe the change in the initial eccentricity. Also, based on the similar methods, stability test is conducted for two Earth-mass test planets in between the two known planets.

Numerical integration comprising of three to five bodies in an elliptical orbits (or circular for special cases) are carried out for a large number of initial conditions (IC) that incorporates the whole phase space of the existing bodies. A global parameter maps (*lifetime* and e_{max}) are then generated to overview the phase space evolution of various orbital elements of inner and middle planets. The long-term evolution of orbital parameters such as a_{pl} and e_{pl} for single IC would allow to explore the amplitude of oscillations, hence predict its future.

The eccentricity of GJ 832c is analyzed in various phase spaces and the relative inclination of the planet is set to a upper limit of 40°. This number seems to be unchanged even when the middle planet was injected into the system. The injected planets also maintained stable orbital configuration for the relative orbital inclination as high as 40°) and a_{pl} ranging from 0.2 to 2.2 AU with an exception of few destabilising resonances between the inner and outer planets. The radial velocity (RV) curves based on the signature from the Keplerian motion and generated for the Earth-mass test planets revealed that the RV signal is much weaker to be measured by currently available instruments.

6.2 Introduction

Recent discoveries of exoplanets have shown that the compact planetary systems seem more common in the Milky way Galaxy. For example, Kepler 186 (Quintana et al. 2014) is a five-planet system with the farthest one (Kepler 186f) located at 0.3926 AU and within the habitable zone of the host star. The nearest one (Kepler 186b) is at 0.0378 AU and orbits the star every 3.88 days. Another such planetary system is Gliese 581 (Mayor et al. 2009), which is known to host three planets along with two that are not yet confirmed. The three known planets (Gliese 581b,c,e) orbit the star within 0.02815 AU. Not only Earth-size planets but also the existence of super-Earths in compact multiple systems are more common (Howard et al. 2012; Batalha et al. 2013).

GJ 832 planetary system is another potentially multi-planet system that is currently known to host two planets within 3.6 AU from the M dwarf star. GJ 832c (inner planet) (Wittenmyer et al. 2014) orbits its star at a distance 0.16 AU away and is potentially a rocky planet with a mass $\geq$5.4 $M_{\oplus}$. This planet resides in the inner boundary of the habitable zone, but its not expected to be habitable mostly due to

its close proximity to the star and possibility of having dense atmosphere. Orbiting the same star, a long-period (∼3657 days) giant planet at 3.53 AU and with a mass of 0.64 M_J, GJ 832b (outer planet) was previously discovered by Bailey et al. (2009). The planet is well outside the habitable zone. Here, our goal is to explore its effect on the orbital stability of the inner planet as well as Earth-mass test planets injected in between the inner and outer planets. Best fit orbital parameters of GJ 832 system is given in Table 6.1 and for the unknown parameters, they are fixed at zero or at certain ranges.

Table 6.1. Best-fit orbital parameters of the GJ 832 system obtained from Wittenmyer et al. (2014). Mass of the star = 0.45 $M_\odot$

Parameters	GJ 832b	GJ 832c
Mass ($M_\oplus$)	216 [188, 245]	5.4 [4.45, 6.35]
Semi-Major Axis (a)	3.56 AU [3.28, 3.84]	0.163 AU [0.157]
Eccentricity (e)	0.08° [0.02, 0.1]	0.18° [0.05, 0.31]
Inclination (i)	(0-90)°	0°
Longitude of the Ascending Node (Ω)	0°	0°
Argument of the Periapsis (ω)	246° [224, 268]	10.0° [323, 57]
Mean Anomaly (μ)	307° [285, 330]	165° [112, 218]

The long term stability and orbital configurations of the inner and test planets with concentration on the evolution of their eccentricity and inclination is studied in various phase spaces. The effect from the injection of test planets in the previously found unstable resonance in the planet's semi-major axis, eccentricity and inclination phase spaces is noted as well. This primarily assisted us in knowing the affects of outer giant planet in the dynamics of inner planets.

GJ 832 is a main sequence dwarf star of a spectral type M1.5V (Jenkins et al. 2006), mass of 0.45 $M_\odot$ (Bonfils et al. 2013), temperature of 3472 K (Casagrande

et al. 2008), and is at a distance of 16.1 light years. The classical habitable zone for this star is calculated using the formulae provided by Kopparapu et al. (2013).

6.3 Numerical Simulations

We considered the motion of the planets of mass, m_{pl} around the central star in elliptic orbits (unless the initial condition (IC) being tested is for the circular case). To calculate the ICs in position and velocity, we used the best-fit orbital elements, semi major axis (a), eccentricity (e), inclination (i), argument of periapsis (ω), ascending node (Ω) and mean anomaly (M), that are obtained from the radial velocity measurements (Wittenmyer et al. 2014). For any unconstrained parameters, the values are taken in a range or considered zero. The initial inclination of the inner planet is taken relative to the orbital plane of star - outer planet system.

Using the orbital integration package MERCURY (Chambers & Migliorini 1997; Chambers 1999), the built-in Hybrid algorithm was used to integrate the orbits of the system in astrocentric coordinates. MERCURY was effective in monitoring the ejection/collision of a planet (either inner or outer) due to close encounter with the star or the gas giant. A time step of $\epsilon = 10^{-3}$ year/step was considered to have high precision. The change in total energy and total angular momentum was calculated at each time step which fell within the range of 10^{-16} to 10^{-13} during the total integration period of 10 Myr. The data sampling (DSP) was done per year for shorter integration periods (up to 10000 kyr) and per five hundred years for longer integration periods. The *lifetime* map and the maximum eccentricity (e_{max}) map are generated for 16,000 initial conditions in a_{pl}, e_{pl} and i_{pl}, and simulated for 10 Myr.

6.4 Results and Discussion

6.4.1 Dynamics of GJ 832c

The orbits of the inner and outer planet integrated with 16,000 ICs provided us with a global dynamical phase space for chosen orbital elements. Each IC is allowed to evolve for 10 Myr and close encounters, ejection or collision are allowed during the integration period. If the integrated orbit survives the total simulation time, then we consider it to be a stable orbit. In the cases when the integrated bodies eject or collide during close encounters, hence resulting in the instability, we note the time of such event and use them to create a global dynamical *lifetime* map.

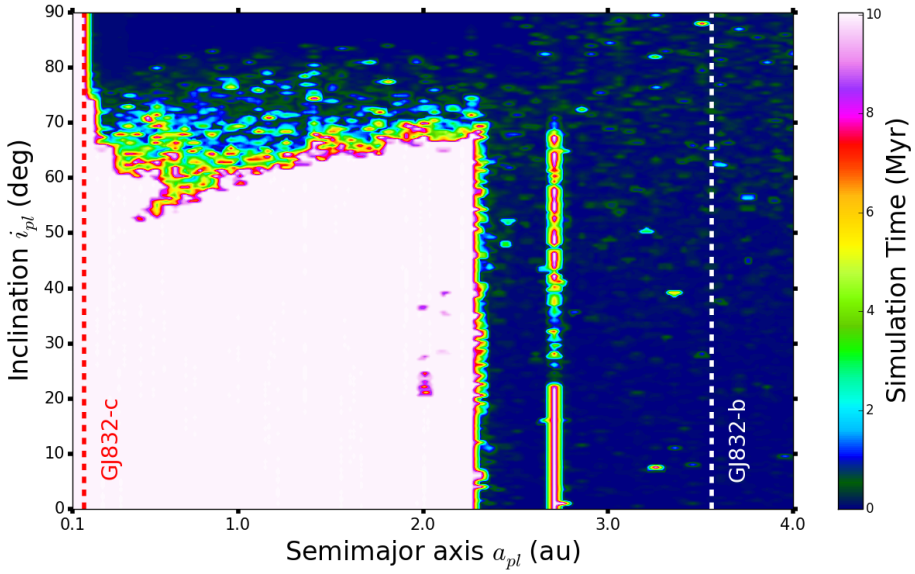

Figure 6.1. A global dynamical *lifetime* map of the planet, GJ 832c, in varying i_{pl} and a_{pl} phase space, simulated for 10 Myr. The colour bar indicates the survival time, where darker colour represents the instability (ejection or collision) and the lightest colour represent the stability (survival) up to the integration period. The vertical dashed lines at 0.16 AU and 3.56 AU represent the best-fit semimajor axis of inner and outer planets. The vertical instability structure at 2.7 AU is due to the 3:2 orbital resonance with the outer planet (Satyal et al. 2014a).

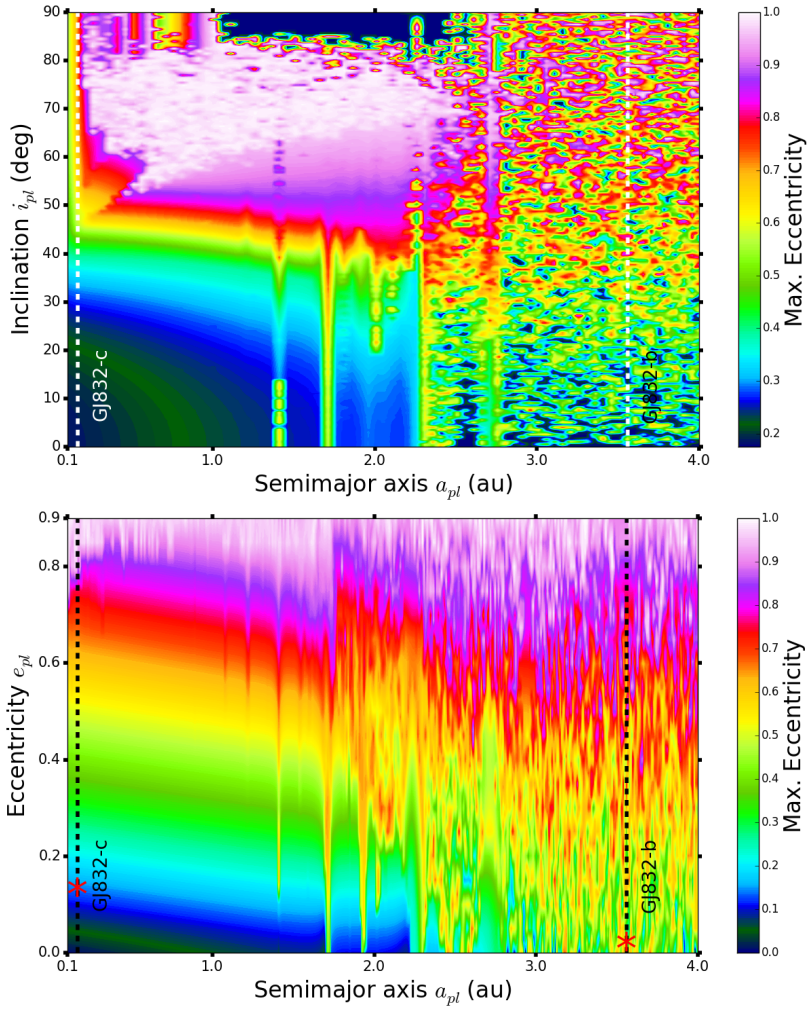

Figure 6.2. (top panel) e_{max} map of the planet, GJ 832c, in i_{pl} and a_{pl} phase space, simulated for 10 Myr. The colour bar indicates the e_{max} reached by the planet during the total simulation time, which also includes the cases when the planet suffers an ejection or collision (especially when e_{pl} reaches a value greater than 0.7). The dark blue-green colour represents the best-fit e_{pl} parameter ($\sim$0.18) and other colours represent the evolution of e_{pl} to the e_{max} value for the respective choices of initial conditions in i_{pl} and a_{pl}. The vertical dashed lines denote the best-fit semimajor axis of the planets. (bottom panel) e_{max} map in e_{pl} - a_{pl} phase space where the red asterisks denote the best-fit eccentricity value of the planets (Satyal et al. 2014a).

To explore the dynamics of the inner planet, its *lifetime* map (Fig. 6.1) is created for multi ICs in i_{pl} and a_{pl} phase space. Each colored pixel represents the evolution of one IC. The light pink color in the map indicates the survival of the

planet for total simulation time, and the other darker color represents instability. The vertical lines, labelled as GJ 832c and GJ 832b, represents the best-fit semimajor axis of the planets. At the best-fit location, GJ 832c displays stability for orbital inclination as high as 75°. Beyond this inclination, the planet is ejected from the system due to the increment in e_{pl} values which results in decreased periastron passage around the star. The vertical structures seen at 2.26 AU and 2.7 AU are the 2:1 and 3:2 resonances due to GJ 832b, respectively.

The e_{max} map (Fig. 6.2, top panel) predicts the long term orbital stability of GJ 832c. Each ICs is integrated for 10 Myr and the evolution of its e_{pl} value is recorded every 500 years. The color bar in the map represents the maximum orbital eccentricity experienced by the planet during the total integration period. The e_{pl} evolution is distinct and in increasing order along the vertical dashed line at 0.16 AU. The blue-green region is where the e_{pl} stays less than 0.4, beyond which the e_{max} is higher than 0.4 and it is expected to increase with longer simulation time. It suggests that the likely i_{pl} value is less than 45°. We note that the maximum i_{pl} value observed in the lifetime map is 75°, however, e_{max} map is more indicative of the orbital evolution. The vertical structures seen at 1.71 AU, 2.26 AU and 2.7 AU are the 3:1, 2:1 and 3:2 resonances due to GJ 832b, respectively. The vertical structure at 1.4 AU could be due to 4:1 resonance with GJ 832b or 2:5 resonance with GJ 832c.

Inner planets orbital evolution in e_{pl} and a_{pl} phase space (Fig. 6.2, bottom panel) also reveals similar resonances with the outer planet. The stability of the planet remains unchanged at the best-fit orbital parameters and e_{pl} deviates least as the planet is moved further out from the star. The upper limit in the uncertainty of the best-fit e_{pl} (0.31) also deviates least during the full integration period. Analysis of dynamics of the planetary orbit of GJ 832b is excluded because there are no known bodies outside its orbit that could constraint its orbital parameters.

6.4.2 Dynamics of hypothetical Earth-mass planets

The known planetary configuration shows a super Earth orbiting at the close proximity of the host star while a gas giant orbits distantly at 3.56 AU. Existence of other Earth-mass planets between these planets is a likely scenario. We injected a fourth body (an Earth-mass test planet) between the two existing planets and studied the orbital dynamics in the similar parameter space as in Figs. 6.1 and **??**. The test planet's *lifetime* map (Fig. 6.3) indicates a wide stability region extending from about 0.2 AU to 2.2 AU. The vertical resonance structures are observed at 1.71 AU, 2.26 AU and 2.7 AU, similar to that seen in Fig. 6.2. As expected, when the planet was set to evolve with an IC close to its companions, the planets collided to each other, hence inducing instability in the system. For high enough i_{pl} values ($\geq 55°$), it was ejected from the system.

In Fig. 6.4, stability of the middle planet is analysed in terms of e_{max} map. The regions where the color map indicates blue-green are expected to remain stable as it shows the least change in the initial eccentricity value. The region of stability is similar to that seen in Fig. 6.3, however, the orbital inclination regime could be safely set at values less than 40°. Beyond 40°, the e_{max} evolved to higher than 0.5 and it is only expected to increase for longer simulation time. The observed resonance at 1.4 AU in Fig. 6.2 disappears with an addition of the middle planet.

Two Earth-mass test planets were injected between the known inner and outer planets at 0.5 AU and 1.0 AU. The i_{pl}, a_{pl} phase-space map for one of the injected planets at 0.5 AU (while other ones were fixed at their respective distances from the star) is shown in Fig. 6.4, bottom panel. The instability islands are observed as expected. The color bar here represents the maximum eccentricity variance of the whole system to incorporate the deviation in eccentricity of each body in the system.

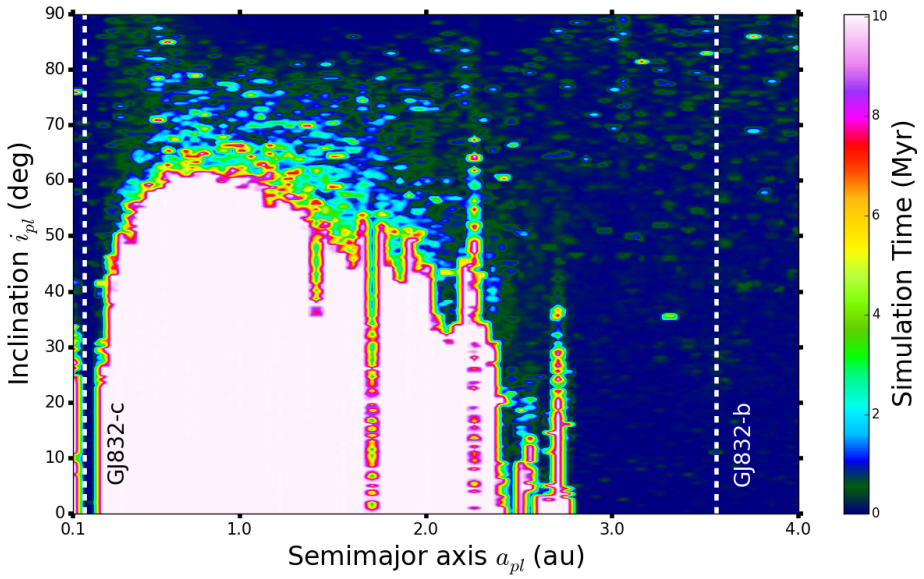

Figure 6.3. A global dynamical *lifetime* map of the middle planet in GJ 832 system, for varying i_{pl} and a_{pl}, simulated for 10 Myr. The colour bar indicates the survival time, where darker colour represents the instability (ejection or collision) and the lightest colour represent the stability (survival) up to the integration period. The vertical dashed lines are the location of the best-fit semimajor axis of the two known planets (Satyal et al. 2014a).

For GJ 832, in order to get the observational verification of these proposed test planets, the direct imaging is particularly a better choice over transit or RV methods because the test planets may be too small to produce RV signatures. We generated a set of synthetic RV curves based on the RV signature of Keplerian motion (Seager 2011) for GJ 832c and an Earth-mass test planet located at 0.5 AU (Fig. 6.5). The maximum RV signal for GJ 832c is ∼2.15m/s, similar to the observational value (Wittenmyer et al. 2014). But the test planet had only 0.19m/s, which is much smaller than the current high accuracy RV precision of about 0.97m/s of the HARPS instruments. This RV signal would increase for bigger planets, but the recent RV observation clearly indicates that GJ 832c is the biggest planet interior to GJ 832b.

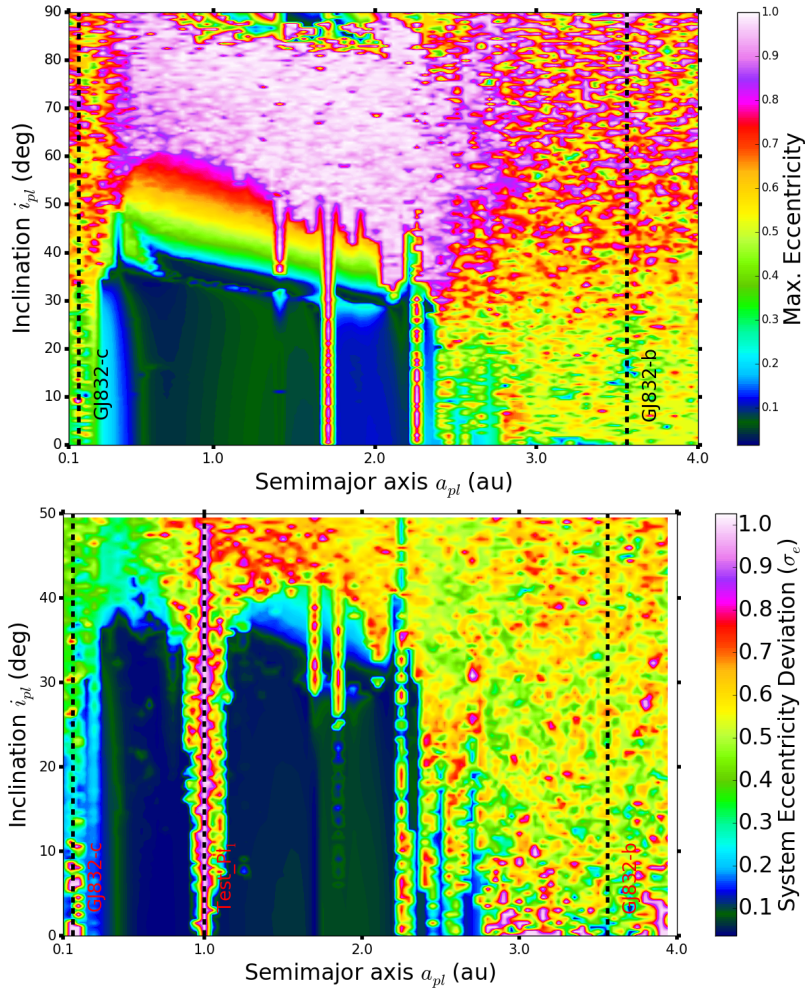

Figure 6.4. Maximum eccentricity (e_{max}) map of the Earth-mass test planet between inner and outer planets, in the i_{pl} and a_{pl} phase space, simulated for 10 Myr (top panel). The colour bar indicates the e_{max} the planet attains during the total simulation time, which also includes the cases when the planet suffers an ejection or collision (especially when e_{pl} reaches a value greater than 0.5). The dark blue-green colour represents the best-fit e_{pl} parameter (0.18) and other light colour represent the e_{max} value the planet attained for the respective choices of initial conditions in i_{pl} and a_{pl}. The vertical dashed line are the best-fit semimajor axis of the known two planets. (bottom panel) e_{max} map for the injected second test planet while the first one is fixed at 1.0 AU and two known planets at their respective positions. The color bar indicates the e_{max} variance of the whole system (Satyal et al. 2014a).

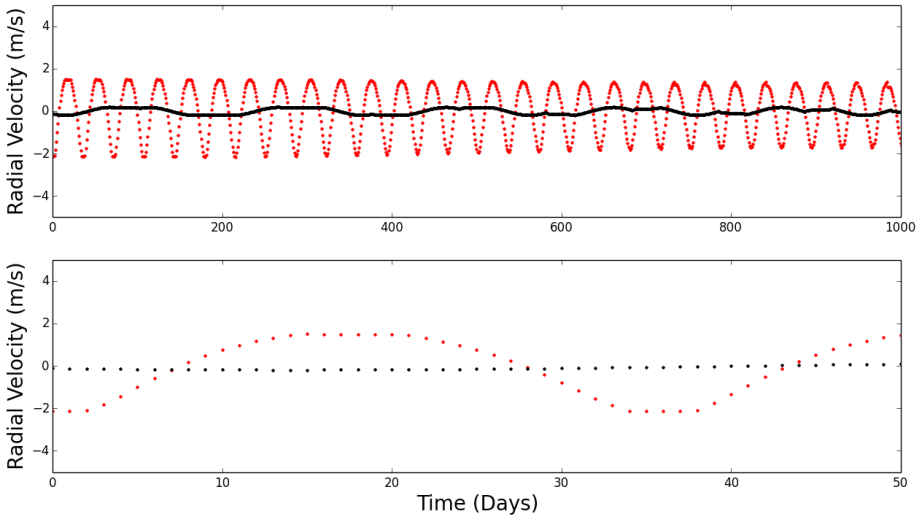

Figure 6.5. Radial velocity signature of Keplerian motion is shown for the inner planet GJ 832c (red) with the maximum amplitude 2.15m/s and for the test planet at 0.5 AU (black) with the maximum amplitude 0.19m/s. Right bottom panel displays the details for the first 50 day-orbit (Satyal et al. 2014a).

6.5 Summary

The *lifetime* maps, e_{max} maps, and the time evolution of the chosen orbital elements for GJ 832c indicates the stable orbital configuration for its best-fit orbital solutions. The maximum eccentricity deviation remained within the best bit uncertainty values. Based on the e_{max} phase space maps for i_{pl}, e_{pl} and a_{pl}, the relative inclination of the planet could be set to $\leq 40°$.

The i_{pl} regime seems to be unchanged even when an Earth-mass test planet was injected into the system. The middle planet also maintained stable orbital configuration for the relative orbital inclination as high as 40° and a_{pl} ranging from 0.2 to 2.2 AU. The planet displayed few de-stabilising resonances between the inner and outer planets, however, did not disrupt the dynamics of the system. Also, it is found that the addition of the second test planet does not change the orbital configuration of the other planets.

Our orbital stability analysis clearly indicates the possible existence of Earth-mass test planets in the system. The calculated RV signal for these planets is too small to detect. The transit method, provided that the planets are along the line-of-sight, and the direct imaging are the only viable options to get the observational verifications.

CHAPTER 7

CONCLUSIONS AND FUTURE WORK

Understanding the motion of stars and planets have been an ongoing process since hundreds of years and theories after theories have been developed to explain and establish *natural laws*, which govern all known matter. With the exploration of new galaxies and hundreds of new planetary systems, new opportunities have surfaced either to test the existing theory or to create a new one. In this dissertation, I produced some scientific work to elaborate the knowledge we have regarding the dynamics and stability of exoplanets through the perspective of orbital resonance and stability.

7.1 Conclusions

To address the issues regarding dynamics of a planet around a star, which is a primary component of a binary system, I used a stability criterion based on the Hill stability (HS) function, which is a major focus of my first project presented in Chapter 3. The stability criteria are for an elliptic orbit, hence it can be applied to more general systems. The HS function, which measures the orbital perturbation of a planet due to the secondary companion, is calculated for the two known binary star systems, γ Cephei and HD 196885 AB, and the obtained results are analyzed and compared with the results obtained from the application of the previously well known chaos indicators such as maximum Lyapunov exponents (MLE) and MEGNO maps.

The analysis from my HS criteria is in agreement with the results obtained from the MLE and the MEGNO maps for periodic and chaotic orbits. The time that the HS criterion took to indicate the chaotic orbits was either equal to that of the MLE or more, depending on the choice of the system. The limitations on the definition of the HS was noted as well. The HS function can only be used for the S-type orbits, thus it may be best suited for studies of hypothetical or observed moons around gas giants as a number of observed planets in the S-type orbits remain modest.

By applying the chaos indicators, it was determined that the planets in γ Cephei and HD 196885 AB can maintain stable orbits for their orbital inclination with the binary plane rising as high as 25°. The planet in γ Cephei/HD 196885 displays stable orbits for e_{bin} as high as 0.6/0.46. Similar studies performed by using the global MEGNO maps of e_{bin} vs. i_{pl} for given orbital parameters agree with the results from the MLE and HS.

The analysis of orbital dynamics in Chapter 3 was limited to planet's orbital inclination less than 25°. Thus in Chapter 4, I explored dynamics of the S-type planetary orbit in HD 196885 AB with an emphasis on higher inclination relative to the binary plane. I used Lidov-Kozai mechanism to explain the observed highly eccentric orbits of the planet in HD 196885 AB and looked into detail of the same mechanism that might be responsible for the planet's possible high inclination. The actual inclination of the planet is unknown, the main purpose of this project was to constrain this parameter to closest value possible. For this, I used the MEGNO maps to demonstrate the existence of regions of periodicity and chaos for varying orbital elements. Also, for similar initial conditions (IC) a dynamical lifetime map and planet's maximum eccentricity maps are produced. To explore the close mean motion resonance (MMR) at the nominal location, the resonant angle is studied for various ICs.

For specific ICs, the planetary orbit can flip to retrograde orbit; however, the planet in HD 196885 AB is not found to flip. The maximum inclination that a planet can rise above the binary plane is found to be $i_{pl} = 82°$, based on the a_{pl} vs. i_{pl} map. The e_{max} map of the planet has further helped to constrain the i_{pl} value to a smaller regime. The planet's maximum eccentricity reaches the extreme values, from 0.7 to ~ 1 for the i_{pl} greater than 55°; nonetheless, the planet survives the total integration time until the i_{pl} is raised to 82°. But, the eccentricity is expected to grow higher for longer simulation time, so the planet may loose its stability for higher i_{pl} values, where the e_{pl} is already found to have reached 0.7 or more. The e_{max} stays relatively low, between 0.48 and 0.68, for the i_{pl} values less than 55°, excluding the case when i_{pl} is $\sim 39°$.

The planet at 2.6 AU is found to have the mean motion resonance (MMR) to be *near* a 39:2 commensurability with the secondary component. When the planet's location is moved to 2.58 AU and 2.68 AU (but within the observational uncertainty limit), the planet is found to exhibit oscillations due to the 20:1 and 19:1 MMRs, respectively. The time evolution of the angles $\varpi_{pl} - \varpi_{bin}$ shows circulation between 0° and 360° when the i_{pl} is set at lower values suggesting the observed chaos is caused by the MMR. Secular resonance at the semi quasi-periodic region ($i_{pl} = 35°$) shows circulation as well, but with a different orientation (Murray & Dermott 1999). Then, the MMR value is used to search for a librating resonant angle (Eq. 4.5), for $k_1 = 39$, $k_2 = -2$, and various other combinations of k_3, k_4, k_5 and k_6 due to the influence of secular components.

The planets higher mass is possibly constrained between (3 - 6)M_J; however, these choices also depend on the choice of planet's orbital inclination and it is mostly favorable when m_{pl} is less than $6M_J$ and i_{pl} less than $\sim 55°$, with some exceptions of chaotic islands (Fig. 4.9). The planetary mass higher than $9M_J$ and up to $19M_J$

is likely when the planet's orbital inclination lies in a smaller regime, somewhere between 40° and 50°.

7.2 Future Work

Through various numerical techniques, I analyzed the orbital stability and dynamics (chaotic and periodic) of planets in single and multi-stellar system. More general studies and formulation of the critical semimajor axis of a planet in binary star system was discussed in chapter 6. A fit formula that will be a function of binary semimajor axis and eccentricity, the stellar mass ratio and planetary eccentricity will be devised with a better precision in future work.

Long term orbital stability is vital for life to develop in a planet residing in the habitable zone (based on the fact that Earth was formed 4.5 billion years ago whilst life started to evolve after a billion year), thus the studies I made and the tools I developed can be (and will be) further extended in the analysis of planets in habitable zones (HZ). The planets search mission, such as *Kepler*, found numerous gas giants within the HZs of the host stars. Since these giant planets are inhospitable for life (based on our current definition of habitability), a terrestrial moon orbiting these planets are very likely to be habitable. Understanding the dynamics of these moons in presence of other nearby planets would be a justifiable goal for my post-doctoral research project.

One of the research projects I discussed in this dissertation includes the detection of exomoon through the modulation of radio emission. This is purely a theoretical calculation of the flux the exoplanet-exomoon must emit so that its signature can be detected here on Earth. The continuation of the project would be to use of one of the suggested radio telescope in order to detect an exomoon in the nearby planetary system. At the time of this dissertation writing, a proposal is being written in col-

laboration with Joaquin Noyola and Zdzislaw Musielak, which will be submitted to the Low Frequency Array (LOFAR) Radio Observatory for the observation time.

Also, I have been externally involved with *Eclipsing Binary Kepler Group* working in the detection and characterization of additional planets in the Kepler 47 circumbinary system. This discovery is expected to appear in the *Science* at the end of 2014.

APPENDIX A

DETERMINATION OF THE ORBITAL ELEMENTS FROM STATE VECTORS

The orbital elements $\{a, e, i, \Omega, \omega, f\}$ can be determined for any system relative to the central body which is the most massive body M_1 in the N body problem. Such elements are found via two different methods such as using Lagrange's Planetary equations of motion or through a transformation of the Cartesian state vectors from conventional integration methods. This appendix will discuss the latter rather than the former as this is the method that was most useful in determining the orbital elements for analysis within this dissertation.

A.1 Assumptions

Several assumptions need to be made to make the appropriate transformations to obtain the orbital elements. The first and foremost assumption is what is necessary to perform the transformation. The position state vector ($\mathbf{R}$), velocity state vector ($\mathbf{V}$), and gravitational parameter (GM_i) are the required known parameters at a given time where M_i is the mass of the central body. In terms of the general restricted three body problem (RTBP) the gravitational parameter is given as $GM\alpha$ where M represents the total mass and alpha is the larger of the two mass ratios (see Chapter **??**). The value for G is chosen to be consistent with the value chosen for performing the simulations. For this dissertation, I have chosen $G = 4\pi$ with units of $M_\odot$, AU, and years. The coordinate system relative to the central body will be described by the Cartesian coordinates $\{x, y, z, \dot{x}, \dot{y}, \dot{z}\}$ as shown by Figure A.1 where the orbital plane, reference plane, and nodal intersection points have also been shown. For the sake of a more general perspective such as in the RTBP, this particular coordinates system could be constructed via translation (ie., $x_i = \xi_i - \xi_1$). Another assumption to be made is that the coordinates have appropriate units before the transformation. This follows from the assumption that the purpose of transforming state vectors to

orbital elements is to verify constants of motion in the 2 body problem or investigate osculating elements for the general N body problem.

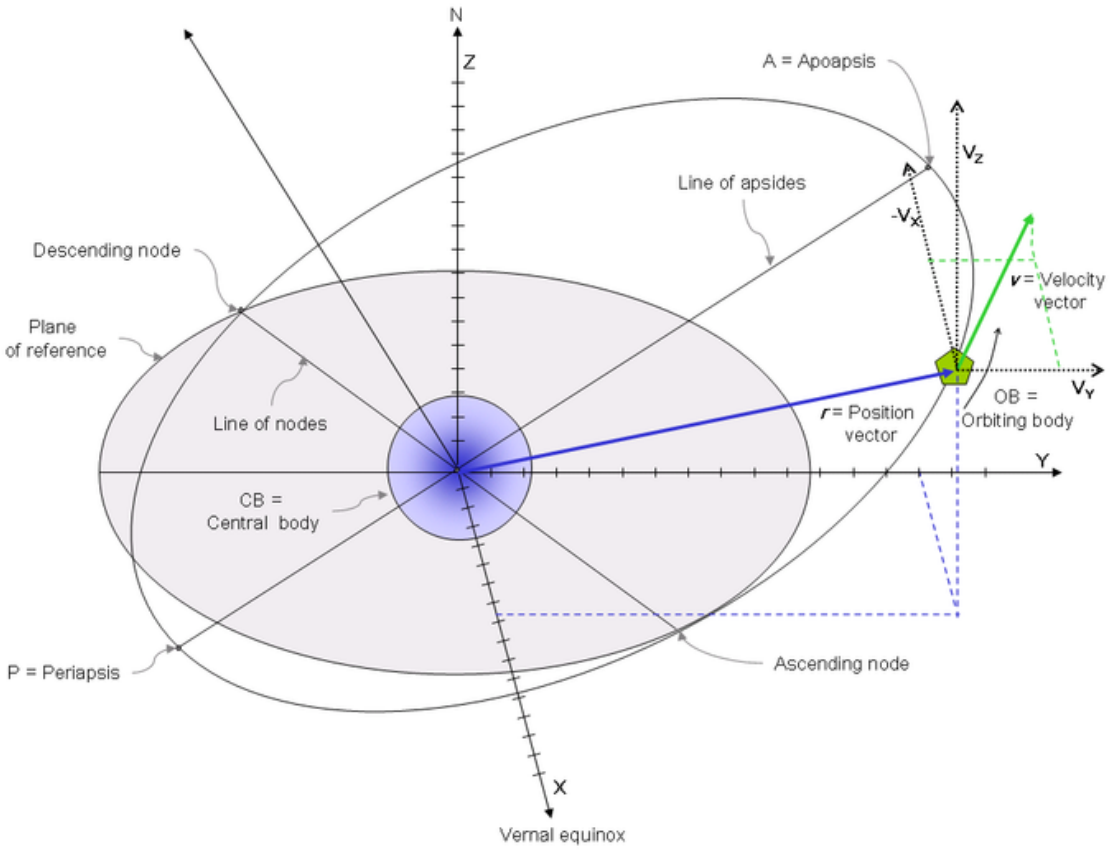

Figure A.1. Illustration of the determination of the orbital state vectors $\mathbf{R}, \mathbf{V}$ relative to a central body. Image Credit: Wikipedia.

The necessary assumptions are:

1. The only parameters to be known *a priori* are the orbital state vectors $(\mathbf{R}, \mathbf{V})$ and the appropriate gravitational parameter GM_i.
2. A coordinate system can be constructed such that the central body exists at the origin (ie., $x_i = \xi_i - \xi_1$).

3. A 2 body problem shall return the constants of motion of the system where a (N > 2) body problem will return the osculating elements.

A.2 Calculation

The orbital state vectors can be used to define a specific angular momentum vector **h** through the use of a cross product to find that $\mathbf{h} = \mathbf{R} \times \mathbf{V}$. Using this newly defined quantity I can determine directly the inclination of the orbit relative to the reference plane as

$$i = \frac{h_z}{|h|}. \tag{A.1}$$

Then a normal vector **n** can be determined through the cross product of the z-axis and the specific angular momentum to produce $\mathbf{n} = \hat{z} \times \mathbf{h}$ and scalar $n = |\mathbf{n}|$. The vector **n** will be utilized to explore all the possible cases to determine the ascending node, Ω. Using the normal vector, the following equations explore each different case as

$$\text{If } \mathbf{n} = \{0, 0, 0\} \qquad \text{then } \Omega = 0, \tag{A.2}$$

$$\text{If } \mathbf{n} > \{0, 0, 0\} \text{ and } n_y > 0 \qquad \text{then } \Omega = \cos^{-1}\left(\frac{n_x}{|n|}\right), \tag{A.3}$$

$$\text{If } \mathbf{n} > \{0, 0, 0\} \text{ and } n_y < 0 \qquad \text{then } \Omega = 2\pi - \cos^{-1}\left(\frac{n_x}{|n|}\right). \tag{A.4}$$

Next the orbital vectors, specific angular momentum, and the gravitational parameter can be used to determine the eccentricity vector whose magnitude produces the orbital element eccentricity. This is done by the using the following equations

$$\mathbf{e} = \frac{\mathbf{V} \times \mathbf{h}}{GM_1} - \frac{\mathbf{R}}{|\mathbf{R}|}, \tag{A.5}$$

$$e = |\mathbf{e}| \,. \tag{A.6}$$

Using the determined values for n and e I can introduce cases to determine the value of the argument of pericenter, ω. The following equations demonstrate the appropriate cases by

$$\text{If } n = 0 \text{ or } e = 0 \qquad \text{then } \omega = 0, \tag{A.7}$$

$$\text{If } n > 0 \text{ and } e_z > 0 \qquad \text{then } \omega = \frac{\mathbf{n} \cdot \mathbf{e}}{|\mathbf{n}| \, |\mathbf{e}|}, \tag{A.8}$$

$$\text{If } n > 0 \text{ and } e_z < 0 \qquad \text{then } \omega = 2\pi - \frac{\mathbf{n} \cdot \mathbf{e}}{|\mathbf{n}| \, |\mathbf{e}|}. \tag{A.9}$$

Using the orbital elements determined thus far the true anomaly f can be determined through different cases. The following equations demonstrate the appropriate cases by

$$\text{If } e = 0 \text{ and } (\mathbf{n} \times \mathbf{R})_z \geq 0 \qquad \text{then } f = \cos^{-1}\left(\frac{\mathbf{n} \cdot \mathbf{R}}{|\mathbf{n}| \, |\mathbf{R}|}\right), \tag{A.10}$$

$$\text{If } e = 0 \text{ and } (\mathbf{n} \times \mathbf{R})_z < 0 \qquad \text{then } f = 2\pi - \cos^{-1}\left(\frac{\mathbf{n} \cdot \mathbf{R}}{|\mathbf{n}| \, |\mathbf{R}|}\right), \tag{A.11}$$

$$\text{If } e > 0 \text{ and } \left(\frac{\mathbf{R} \cdot \mathbf{V}}{|\mathbf{R}|}\right) \geq 0 \qquad \text{then } f = \cos^{-1}\left(\frac{\mathbf{e} \cdot \mathbf{R}}{|\mathbf{e}| \, |\mathbf{R}|}\right), \tag{A.12}$$

$$\text{If } e > 0 \text{ and } \left(\frac{\mathbf{R} \cdot \mathbf{V}}{|\mathbf{R}|}\right) < 0 \qquad \text{then } f = 2\pi - \cos^{-1}\left(\frac{\mathbf{e} \cdot \mathbf{R}}{|\mathbf{e}| \, |\mathbf{R}|}\right). \tag{A.13}$$

Finally the semimajor axis can be determined through the relation

$$a = \frac{h^2}{GM_1(1-e^2)}, \tag{A.14}$$

where a negative value for semimajor axis would indicate that the orbital type is a hyperbola.

APPENDIX B

CALCULATION OF THE LYAPUNOV SPECTRUM

B.1 Circular Restricted Three-Body Problem

In the CRTBP I have used a rotating coordinate system which gives rise to Coriolis and centrifugal forces. The equations of motion of such a system are given by

$$\begin{aligned} \dot{x} &= u & \dot{u} &= 2v + x - \alpha\frac{x-\mu}{r_1^3} - \mu\frac{x+\alpha}{r_2^3}, \\ \dot{y} &= v & \dot{v} &= -2u + y - \alpha\frac{y}{r_1^3} - \mu\frac{y}{r_2^3}, \\ \dot{z} &= w & \dot{w} &= -\alpha\frac{z}{r_1^3} - \mu\frac{z}{r_2^3}, \end{aligned} \tag{B.1}$$

where

$$\begin{aligned} \mu &= \frac{m_2}{m_1+m_2} & r_1^2 &= (x-\mu)^2 + y^2 + z^2, \\ \alpha &= 1-\mu & r_2^2 &= (x+\alpha)^2 + y^2 + z^2. \end{aligned} \tag{B.2}$$

From these equations of motion I can define a set of 6 dimensional tangent vectors $\mathbf{x}_i$ and their derivatives $\dot{\mathbf{x}}_i$ where $i = 1, \ldots, 6$. This set of vectors are given as

$$\begin{aligned} \mathbf{x}_i &= \{x_i, y_i, z_i, u_i, v_i, w_i\}^T, \\ \dot{\mathbf{x}}_i &= \{u_i, v_i, w_i, \dot{u}_i, \dot{v}_i, \dot{w}_i\}^T. \end{aligned} \tag{B.3}$$

Also I can define a Jacobian matrix (see Section 2.9), $\mathbf{J}$, of the following form

$$\mathbf{J} = \begin{pmatrix} 0 & 0 & 0 & 1 & 0 & 0 \\ 0 & 0 & 0 & 0 & 1 & 0 \\ 0 & 0 & 0 & 0 & 0 & 1 \\ \frac{\partial \dot{u}}{\partial x} & \frac{\partial \dot{u}}{\partial y} & \frac{\partial \dot{u}}{\partial z} & 0 & 2 & 0 \\ \frac{\partial \dot{v}}{\partial x} & \frac{\partial \dot{v}}{\partial y} & \frac{\partial \dot{v}}{\partial z} & -2 & 0 & 0 \\ \frac{\partial \dot{w}}{\partial x} & \frac{\partial \dot{w}}{\partial y} & \frac{\partial \dot{w}}{\partial z} & 0 & 0 & 0 \end{pmatrix}. \tag{B.4}$$

B.2 Wolf method

Wolf et al. (1985) has established a method to determine the Lyapunov spectrum and here I will apply this to the CRTBP. The Wolf algorithm consists of three basic steps. The first step is to initialize a state vector of 6 elements with initial conditions. Then, the tangent vectors need to be initialized to some value. It has become convention to have all the tangent vectors to be unit vectors for simplicity. This means that the elements $\{x_1,\ y_2,\ z_3,\ u_4,\ v_5,\ w_6\} = 1$ and all other elements will equal 0.

The next step is to implement a loop in time that will use a standard integrator (Runge-Kutta, Gragg-Burlish-Stoer, etc.) to determine how the vectors (state & tangent) will change within a time step. This will continue for a arbitrary number of steps so that the tangent vectors can orient themselves along the flow. When this has been accomplished, the final step is to perform the Gram-Schmidt Renormalization (GSR) to orthogonalize the tangent space (see below). Thereafter, I can take the logarithm of the length of each tangent vector to obtain the Lyapunov exponents and continue the loop for the next time interval.

B.3 GSR & the Lyapunov Exponents

I use the first tangent vector, $\mathbf{x}_1$, to define a basis vector for the GSR process. The first step is to normalize this vector. I will denote vectors with $'$ to be the new orthonormal set of tangent vectors. The transformation to obtain these vectors is given by the following

$$\begin{aligned}
\mathbf{x}_1^{'} &= \frac{\mathbf{x}_1}{\|\mathbf{x}_1\|}, \\
\mathbf{x}_2^{'} &= \frac{\mathbf{x}_2 - \left\langle \mathbf{x}_2,\, \mathbf{x}_1^{'} \right\rangle \mathbf{x}_1^{'}}{\left\| \mathbf{x}_2 - \left\langle \mathbf{x}_2,\, \mathbf{x}_1^{'} \right\rangle \right\|}, \\
&\vdots \\
\mathbf{x}_6^{'} &= \frac{\mathbf{x}_6 - \left\langle \mathbf{x}_6,\, \mathbf{x}_5^{'} \right\rangle \mathbf{x}_5^{'} - \ldots - \left\langle \mathbf{x}_6,\, \mathbf{x}_1^{'} \right\rangle \mathbf{x}_1^{'}}{\left\| \mathbf{x}_6 - \left\langle \mathbf{x}_6,\, \mathbf{x}_5^{'} \right\rangle \mathbf{x}_5^{'} - \ldots - \left\langle \mathbf{x}_6,\, \mathbf{x}_1^{'} \right\rangle \mathbf{x}_1^{'} \right\|}.
\end{aligned} \tag{B.5}$$

From the new set of tangent vectors, the Lyapunov exponents can be calculated directly by using the lengths of each vector using this expression

$$\lambda_i = \frac{1}{\tau} \left[\lambda_{i-1} + \log \left\| \mathbf{x}_i - \sum_{j=1}^{i} \left\langle \mathbf{x}_i,\, \mathbf{x}_{j-1}^{'} \right\rangle \mathbf{x}_{j-1}^{'} \right\| \right] \tag{B.6}$$

where $\lambda_o = \mathbf{x}_o^{'} = 0$.

BIBLIOGRAPHY

Aarseth, S. J. 2003, Gravitational N-Body Simulations, ed. Aarseth, S. J.

Antonini, F., & Merritt, D. 2013, *ApJL* , 763, L10

Arfken, G. B., & Weber, H. J. 1995, Mathematical methods for physicists

Aughton, P. 2008, The Story of Astronomy (Quercus)

Bailey, J., Butler, R. P., Tinney, C. G., et al. 2009, *ApJ* , 690, 743

Barnes, J., & Hut, P. 1986, *Nature* , 324, 446

Batalha, N. M., Rowe, J. F., Bryson, S. T., et al. 2013, *ApJS* , 204, 24

Belcher, J. W. 1987, Science, 238, 170

Benettin, G., Galgani, L., Giorgilli, A., & Strelcyn, J.-M. 1980, Meccanica, 15, 9

Bonfils, X., Delfosse, X., Udry, S., et al. 2013, *A&A* , 549, A109

Borucki, W., Koch, D., Basri, G., et al. 2008, in IAU Symposium, Vol. 249, IAU Symposium, ed. Y.-S. Sun, S. Ferraz-Mello, & J.-L. Zhou, 17–24

Borucki, W. J., Koch, D., Basri, G., et al. 2010, Science, 327, 977

Borucki, W. J., Koch, D. G., Dunham, E. W., & Jenkins, J. M. 1997, in Astronomical Society of the Pacific Conference Series, Vol. 119, Planets Beyond the Solar System and the Next Generation of Space Missions, ed. D. Soderblom, 153

Campbell, B., Walker, G. A. H., & Yang, S. 1988, ApJ, 331, 902

Casagrande, L., Flynn, C., & Bessell, M. 2008, *MNRAS* , 389, 585

Chambers, J. E. 1999, *MNRAS* , 304, 793

Chambers, J. E., & Migliorini, F. 1997, in Bulletin of the American Astronomical Society, Vol. 29, AAS/Division for Planetary Sciences Meeting Abstracts #29, 1024

Chatterjee, S., Ford, E. B., Matsumura, S., & Rasio, F. A. 2008, *ApJ* , 686, 580

Chauvin, G., Beust, H., Lagrange, A.-M., & Eggenberger, A. 2011, *A&A* , 528, A8

Chauvin, G., Lagrange, A.-M., Udry, S., & Mayor, M. 2007, *A&A* , 475, 723

Cincotta, P., & Simó, C. 1999, Celestial Mechanics and Dynamical Astronomy, 73, 195

Cincotta, P. M., Giordano, C. M., & Simó, C. 2003, Physica D Nonlinear Phenomena, 182, 151

Cincotta, P. M., & Simó, C. 2000, aaps, 147, 205

Compère, A., Lemaître, A., & Delsate, N. 2012, Celestial Mechanics and Dynamical Astronomy, 112, 75

Cooley, J. W., & Tukey, J. W. 1965, Mathematics of Computation, 19, pp. 297

Correia, A. C. M., Laskar, J., Farago, F., & Boué, G. 2011, Celestial Mechanics and Dynamical Astronomy, 111, 105

Crary, F. J. 1997, *JGR* , 102, 37

Cuntz, M., Quarles, B., Eberle, J., & Shukayr, A. 2013, *PASA* , 30, 33

Curiel, S., Cantó, J., Georgiev, L., Chávez, C. E., & Poveda, A. 2011, A&A, 525, A78

Desidera, S., & Barbieri, M. 2007, *A&A* , 462, 345

Diacu, F. 1996, The Mathematical Intelligencer, 18, 66, 10.1007/BF03024313

Doyle, L. R., Carter, J. A., Fabrycky, D. C., et al. 2011, Science, 333, 1602

Duquennoy, A., & Mayor, M. 1991, *A&A* , 248, 485

Dvorak, R., & Karch, M. 1988, Sterne und Weltraum, 27, 350

Eberle, W. J. 2010, PhD thesis, University of Texas at Arlington, Arlington, TX

Eggenberger, A., Udry, S., & Mayor, M. 2004, *A&A* , 417, 353

Fabrycky, D., & Tremaine, S. 2007, *ApJ* , 669, 1298

Ferraz-Mello, S., & Dvorak, R. 1987, *A&A* , 179, 304

Ford, E. B., Kozinsky, B., & Rasio, F. A. 2000, *ApJ* , 535, 385

Fouchard, M., Lega, E., Froeschlé, C., & Froeschlé, C. 2002, Celestial Mechanics and Dynamical Astronomy, 83, 205

Fourier, J. B. J. 1822, Theorie analytique de la chaleur [microform] / par M. Fourier (F. Didot, Paris :), xxii, 639 p., [2] leaves of plates :

Frigo, M., & Johnson, S. G. 1998, in Proc. 1998 IEEE Intl. Conf. Acoustics Speech and Signal Processing, Vol. 3 (IEEE), 1381–1384

Frigo, M., & Johnson, S. G. 2005, Proceedings of the IEEE, 93, 216, special issue on "Program Generation, Optimization, and Platform Adaptation"

Froeschle, C. 1984, Celestial Mechanics, 34, 95

Froeschlé, C., & Lega, E. 2000, Celestial Mechanics and Dynamical Astronomy, 78, 167

Froeschlé, C., Lega, E., & Gonczi, R. 1997, Celestial Mechanics and Dynamical Astronomy, 67, 41

Frouard, J., Vienne, A., & Fouchard, M. 2011, *A&A* , 532, A44

Giuppone, C. A., Morais, M. H. M., Boué, G., & Correia, A. C. M. 2012, *A&A* , 541, A151

Gonczi, R., & Froeschle, C. 1981, Celestial Mechanics, 25, 271

Goździewski, K., Bois, E., Maciejewski, A. J., & Kiseleva-Eggleton, L. 2001, *A&A* , 378, 569

Goździewski, K., Breiter, S., & Borczyk, W. 2008, mnras, 383, 989

Goździewski, K., & Maciejewski, A. J. 2001, *ApJL* , 563, L81

Goździewski, K., & Migaszewski, C. 2009, *MNRAS* , 397, L16

Grazier, K. R., Newman, W. I., Varadi, F., Goldstein, D. J., & Kaula, W. M. 1996, in Bulletin of the American Astronomical Society, Vol. 28, AAS/Division of Dynamical Astronomy Meeting #27, 1181

Grießmeier, J.-M., Zarka, P., & Spreeuw, H. 2007, *A&A* , 475, 359

Hadjidemetriou, J. D. 1993, Celestial Mechanics and Dynamical Astronomy, 56, 201

Haghighipour, N. 2006, *ApJ* , 644, 543

Hairer, E., Norsett, S. P., & Wanner, G. 1993, Solving Ordinary Differential Equations I, nonstiff problems, 2nd Ed., Springer Series in Computational Mathematics (Springer-Verlag)

Heideman, M., Johnson, D., & Burrus, C. 1984, ASSP Magazine, IEEE, 1, 14

Heller, R. 2012, *A&A* , 545, L8

Hilborn, R. C., & Sprott, J. C. 1994, American Journal of Physics, 62, 861

Hill, G. W. 1878a, *MNRAS* , 38, 192

—. 1878b, Astronomische Nachrichten, 91, 251

Hinse, T. C., Christou, A. A., Alvarellos, J. L. A., & Goździewski, K. 2010, *MNRAS* , 404, 837

Hinse, T. C., Michelsen, R., Jørgensen, U. G., Goździewski, K., & Mikkola, S. 2008, *A&A* , 488, 1133

Holman, M., Touma, J., & Tremaine, S. 1997, *Nature* , 386, 254

Howard, A. W., Marcy, G. W., Bryson, S. T., et al. 2012, *ApJS* , 201, 15

Innanen, K. A., Zheng, J. Q., Mikkola, S., & Valtonen, M. J. 1997, *AJ* , 113, 1915

Jacob, W. S. 1855, MNRAS, 15, 228

Jefferys, W. H., & Yi, Z.-H. 1983, Celestial Mechanics, 30, 85

Jenkins, J. S., Jones, H. R. A., Tinney, C. G., et al. 2006, *MNRAS* , 372, 163

Katz, B., Dong, S., & Malhotra, R. 2011, Physical Review Letters, 107, 181101

King, H. C. 1955, The history of the telescope

Kipping, D. M., Bakos, G. Á., Buchhave, L., Nesvorný, D., & Schmitt, A. 2012, *ApJ* , 750, 115

Kipping, D. M., Hartman, J., Buchhave, L. A., et al. 2013, *ApJ* , 770, 101

Kley, W., D'Angelo, G., & Henning, T. 2001, ApJ, 547, 457

Koch, D., Borucki, W., Basri, G., et al. 2006, Proceedings of the International Astronomical Union, 2, 236

Kopparapu, R. K., Ramirez, R., Kasting, J. F., et al. 2013, *ApJ* , 765, 131

Kozai, Y. 1962, *AJ* , 67, 591

Laskar, J., Froeschlé, C., & Celletti, A. 1992, Physica D Nonlinear Phenomena, 56, 253

Lecar, M., Franklin, F., & Murison, M. 1992, *AJ* , 104, 1230

Li, G., Naoz, S., Kocsis, B., & Loeb, A. 2013, ArXiv e-prints

Lidov, M. L. 1962, *Planetary and Space Science* , 9, 719

Lissauer, J. J. 1999, Nature, 398, 659

Lissauer, J. J., Barnes, J. W., & Chambers, J. E. 2011, in American Astronomical Society Meeting Abstracts, Vol. 218, 402.08

Lissauer, J. J., Jontof-Hutter, D., Rowe, J. F., et al. 2013, ArXiv e-prints

Lithwick, Y., & Naoz, S. 2011, *ApJ* , 742, 94

Lohinger, E., & Froeschle, C. 1993, Celestial Mechanics and Dynamical Astronomy, 57, 369

Lohinger, E., Froeschle, C., & Dvorak, R. 1993, Celestial Mechanics and Dynamical Astronomy, 56, 315

Lopes, R. M. C., & Spencer, J. R. 2007, Io After Galileo: A New View of Jupiter's Volcanic Moon (Springer Praxis Books / Geophysical Sciences)

Luzum, B., Capitaine, N., Fienga, A., et al. 2011, Celestial Mechanics and Dynamical Astronomy, 110, 293, 10.1007/s10569-011-9352-4

Lyapunov, A. 1907, Annales de la facultè des sciences de Toulouse, 2:9, 203

Maffione, N. P., Darriba, L. A., Cincotta, P. M., & Giordano, C. M. 2011, Celestial Mechanics and Dynamical Astronomy, 111, 285

Marchal, C., & Bozis, G. 1982, Celestial Mechanics, 26, 311

MATLAB. 2011, version 7.12.0.635 (R2011a) (Natick, Massachusetts: The MathWorks Inc.)

Mauk, B. H., Williams, D. J., & Eviatar, A. 2001, *JGR* , 106, 26195

Mayor, M., & Queloz, D. 1995, *Nature* , 378, 355

Mayor, M., Bonfils, X., Forveille, T., et al. 2009, *A&A* , 507, 487

Mestre, M. F., Cincotta, P. M., & Giordano, C. M. 2011, *MNRAS* , 414, L100

Mikkola, S., & Innanen, K. 1999, Celestial Mechanics and Dynamical Astronomy, 74, 59

Milani, A., & Nobili, A. M. 1992, *Nature* , 357, 569

Morbidelli, A. 2002, Modern celestial mechanics : aspects of solar system dynamics

Morbidelli, A., & Nesvorny, D. 1999, Icarus, 139, 295

Murray, C. D., & Dermott, S. F. 1999, Solar system dynamics

Murray, N., & Holman, M. 2001, nat, 410, 773

Musielak, Z. E., & Musielak, D. E. 2009, International Journal of Bifurcation and Chaos, 19, 2823

Musielak, Z. E., & Quarles, B. 2014, Reports on Progress in Physics, 77, 065901

Nagasawa, M., Ida, S., & Bessho, T. 2008, *ApJ* , 678, 498

Naoz, S., Farr, W. M., Lithwick, Y., Rasio, F. A., & Teyssandier, J. 2011, *Nature* , 473, 187

—. 2013a, *MNRAS* , 431, 2155

Naoz, S., Farr, W. M., & Rasio, F. A. 2012, *ApJL* , 754, L36

Naoz, S., Kocsis, B., Loeb, A., & Yunes, N. 2013b, *ApJ* , 773, 187

Nesvorný, D., Ferraz-Mello, S., Holman, M., & Morbidelli, A. 2002, Asteroids III, 379

Nesvorný, D., & Morbidelli, A. 1998, *AJ* , 116, 3029

Neubauer, F. M. 1980, *JGR* , 85, 1171

Noyola, J. P., Satyal, S., & Musielak, Z. E. 2013, ArXiv e-prints

Orosz, J. A., Welsh, W. F., Carter, J. A., et al. 2012, Science, 337, 1511

Ott, E. 1993, Chaos in dynamical systems

Ozorio de Almeida, A. M. 1990, Hamiltonian Systems

Patience, J., White, R. J., Ghez, A. M., et al. 2002, ApJ, 581, 654

Quarles, B., Eberle, J., Musielak, Z. E., & Cuntz, M. 2011, A&A, 533, A2

Quintana, E. V., Barclay, T., Raymond, S. N., et al. 2014, Science, 344, 277

Quintana, E. V., Lissauer, J. J., Chambers, J. E., & Duncan, M. J. 2002, ApJ, 576, 982

Raghavan, D., Henry, T. J., Mason, B. D., et al. 2006, *ApJ* , 646, 523

Raghavan, D., McAlister, H. A., Henry, T. J., et al. 2010, *ApJS* , 190, 1

Rasio, F. A., & Ford, E. B. 1996, Science, 274, 954

Ricker, G. R., Latham, D. W., Vanderspek, R. K., et al. 2010, in Bulletin of the American Astronomical Society, Vol. 42, American Astronomical Society Meeting Abstracts #215, 450.06

Satyal, S., Griffith, J., Musielak, Z. E., & Quarles, B. 2014a, *ApJ* , in prep.

Satyal, S., Hinse, T. C., Quarles, B., & Noyola, J. P. 2014b, *MNRAS* , 443, 1310

Satyal, S., Quarles, B., & Hinse, T. C. 2013, *MNRAS* , 433, 2215

Seager, S. 2011, Exoplanets

See, T. J. J. 1896, AJ, 16, 17

Sherrill, T. J. 1999, Journal for the History of Astronomy, 30, 25

Słonina, M., Goździewski, K., & Migaszewski, C. 2012, in Proceedings of the workshop "Orbital Couples: Pas de Deux in the Solar System and the Milky Way". Held at the Observatoire de Paris, 10-12 October 2011. Editors: F. Arenou, D. Hestroffer. ISBN 2-910015-64-5, p. 125-129, ed. F. Arenou & D. Hestroffer, 125–129

Smith, R. H., & Szebehely, V. 1993, Celestial Mechanics and Dynamical Astronomy, 56, 409

Su, Y.-J. 2009, in IAU Symposium, Vol. 259, IAU Symposium, ed. K. G. Strassmeier, A. G. Kosovichev, & J. E. Beckman, 271–282

Szebehely, V. 1967, Theory of orbits. The restricted problem of three bodies

—. 1980, Celestial Mechanics, 22, 7

Szebehely, V., & McKenzie, R. 1981, Celestial Mechanics, 23, 3

Szenkovits, F., & Makó, Z. 2008, Celestial Mechanics and Dynamical Astronomy, 101, 273

Teyssandier, J., Naoz, S., Lizarraga, I., & Rasio, F. A. 2013, *ApJ* , 779, 166

Thebault, P. 2011, Celestial Mechanics and Dynamical Astronomy, 111, 29

Tsonis, A. 1992, Chaos: from theory to applications (Plenum Press)

Veras, D., & Ford, E. B. 2010, *ApJ* , 715, 803

Walker, I. W., & Roy, A. E. 1981, Celestial Mechanics, 24, 195

Welsh, W. F., Orosz, J. A., Carter, J. A., et al. 2012, Nature, 481, 475

Winn, J. N., Fabrycky, D., Albrecht, S., & Johnson, J. A. 2010, *ApJL* , 718, L145

Wisdom, J., & Holman, M. 1992, *AJ* , 104, 2022

Wittenmyer, R. A., Tuomi, M., Butler, R. P., et al. 2014, *ApJ* , 791, 114

Wolf, A., Swift, J. B., Swinney, H. L., & Vastano, J. A. 1985, Physica D Nonlinear Phenomena, 16, 285

Wolszczan, A., & Frail, D. A. 1992, *Nature* , 355, 145

Wu, Y., & Murray, N. 2003, *ApJ* , 589, 605

Wu, Y., Murray, N. W., & Ramsahai, J. M. 2007, *ApJ* , 670, 820

Yoshida, H. 1990, Physics Letters A, 150, 262

Zarka, P., Treumann, R. A., Ryabov, B. P., & Ryabov, V. B. 2001, *APSS* , 277, 293

Zhou, L.-Y., Dvorak, R., & Sun, Y.-S. 2009, *MNRAS* , 398, 1217

BIOGRAPHICAL STATEMENT

Suman Satyal started his primary school from Bhaktapur English Secondary School, and got his high school degree from Nobel Academy Higher Secondary School, Nepal in 2001. He started his Undergraduate studies from Truman State University, MO as a computer science student in 2003. He had his associate degree in General Science from Navarro College in 2007 and B.Sc. in Physics from UT Arlington in 2009. He then continued his masters at UTA working for Prof. Dr. Alexander Weiss. He went to work at the Brookhaven National Lab, NY as a part of his Masters thesis and studied the Auger Photo-electron Coincidence Spectroscopy in 2011.

Suman continued his Ph.D. in the area of astronomy and astrophysics with Prof. Dr. Zdzislaw Musielak at UT Arlington and started working on the dynamical analysis of exoplanets in stellar binaries. He later extended his interests into detection of exoplanets and exomoons. He has authored seven scientific papers that have been peer-reviewed and published in top journals such as the *Science, ApJ, A&A, MNRAS and JESRP*. Suman is awarded with R. Jack Marquis Scholarship Award (2009) and Michael B. and Wanda G. Ray Award (2014), Summer Dissertation Fellowship (2014), and I Engage Mentoring Fellowship (2014). As an active member of AAS and APS, he has presented his research in more than 10 national conferences and participated in Sagan Summer Workshop (2012) at Caltech to work on Exoplanet Light Curves, hosted by the NASA Exoplanet Science Institute. He obtained his Ph.D. degree in Astrophysics in the Fall of 2014. He would like to continue his research in exoplanetary science by working as a Post-doctoral fellow.

A billion neutrinos go swimming in heavy water: one gets wet.